ALMA MATER STUDIORUM · UNIVERSITÀ DI BOLOGNA

SCUOLA DI SCIENZE
Corso di Laurea in Astrofisica e Cosmologia

Probing General Relativity: New Measures of Gravitational Redshifts in Galaxy Clusters

Relatore:
Prof. Federico Marulli

Candidato:
Damiano Rosselli

Correlatore:
Chiar.mo Prof. Andrea Cimatti

Sessione IV
Anno Accademico 2020-2021

Abstract

Clusters of galaxies provide a natural cosmic laboratory to attempt direct measurements of gravitational redshifts trough the peculiar velocity distribution of cluster member galaxies, thus allowing us to test the Einstein theory of General Relativity (GR) and to investigate the gravitational potential inside them. However, after the pioneering work of Wojtak et al. [2011], only a few results have been obtained, despite the existence of robust theoretical foundations [Cappi, 1995, Kim and Croft, 2004, Croft, 2013]. In this Thesis work we make new measurements of the gravitational redshift effect in galaxy clusters and we provide new constraints on the theory of gravity on the megaparsec scales. To do this, we construct two new catalogs of cluster member galaxies, which have never been exploited in the past literature, by using public available data of cluster and galaxy spectroscopic surveys. In particular, we exploit galaxy coordinates and spectroscopic redshifts derived from the sixteenth data release (DR16) of the Sloan Digital Sky Survey (SDSS; Ahumada et al. [2020]), and two cluster catalogs, namely the *Wen-Han-Liu* cluster catalog (WHL15; Wen et al. [2015]) and the cluster catalog derived from the latest data release of the Dark Energy Survey Instrument (DESI; Zou et al. [2021]). To perform the measurements of the gravitational redshift, we accurately estimate the cluster centers computing as the average of angular positions and redshifts of the closest galaxies to the Brightest Cluster Galaxy (BCG). This choice has never been adopted previously for these measurements. We demonstrate that it provides a better approximation of the center of the cluster gravitational potential well relative to just assuming the BCG as the center, as done in the past literature works [Wojtak et al., 2011, Jimeno et al., 2014, Sadeh et al., 2015]. We consider for the analyses the clusters with high masses, low redshifts, and high numbers of associated member galaxies. These selections, that will be described in details in Sec.5.3, are applied to mitigate the impurities, such as cluster false identifications. We stack all the selected member galaxy data into a single phase-space diagram, which we correct for the foreground and background galaxy contaminations by following the method described in Jimeno et al. [2014]. We split the phase-space diagram into four equal bins of transverse distances, and we model the galaxy velocity distribution, Δ_{mean}, within each bin, to recover the shift of the mean of these distributions, $\hat{\Delta}_{mean}$, as a function of the cluster radius. The latter quantity is proportional to the gravitational redshift effect. Moreover, we compare our measurements with the theoretical predictions of three different gravity theories: GR, $f(R)$ [Sotiriou and Faraoni, 2010], and the Dvali–Gabadadze–Porrati models (DGP; Dvali et al.

[2000]). We implement a new statistical procedure in order to fit the measured gravitational redshift signal and consequently discriminate among the gravity theories. We parameterize the different predictions of the gravitational redshift in the three gravity theories by multiplying the predicted gravitational acceleration experienced by the photons inside the cluster by a constant α, which is the free parameter of the new statistical analysis. By construction α is equal to one in GR theory. We clearly detect the gravitational redshift effect in both the exploited cluster member catalogs. We recover an integrated gravitational redshift signal $\hat{\Delta}_{mean,int} = -11.4 \pm 3.3$ km s^{-1} for the WHL15 clusters, and $\hat{\Delta}_{mean,int} = -14.1 \pm 3.6$ km s^{-1} for the DESI cluster catalog. These results are in agreement, within the errors, with the previous works of Jimeno et al. [2014] and Sadeh et al. [2015], and with the theoretical predictions of Cappi [1995] and Kim and Croft [2004]. We get $\alpha = 0.86 \pm 0.25$ from the WHL15 catalog, and $\alpha = 1.04 \pm 0.28$ from the DESI catalog. Thus, the gravitational redshift measurements are in agreement with the GR predictions considering both the cluster member catalogs. Finally, we investigate the uncertainties possibly affecting our analysis. Firstly, we investigate the effects on the final measurements of the selections we made on the cluster member galaxies for both the cluster catalogs exploited. Then, we investigate the impact of different assumptions in estimating the cluster centers.

The whole statistical analysis of this Thesis work has been performed using the CosmoBolognaLib (CBL; Marulli et al. [2016]), a large set of *free software* C++/Python libraries, that provide an efficient numerical environment for statistical investigations of the large-scale structure of the Universe. The new likelihood functions for fitting the velocity distributions and computing the GR, $f(r)$ and DGP models predictions, will be released in the forthcoming public version of the CBL.

Sommario

Gli ammassi di galassie rappresentano un laboratorio ideale per effettuare misure dirette del redshift gravitazionale tramite la distribuzione delle velocità peculiari delle galassie membro, tramite cui testare la teoria della Relatività Generale di Einstein e studiare il potenziale gravitazionale al loro interno. Nonostante l'esistenza di solide basi teoriche su questo fenomeno [Cappi, 1995, Kim and Croft, 2004, Croft, 2013], dopo il lavoro pionieristico di Wojtak et al. [2011] sono stati ottenuti soltanto pochi risultati in questo ambito. In questa Tesi abbiamo misurato l'effetto del redshift gravitazionale all'interno degli ammassi di galassie e abbiamo fornito nuovi vincoli sulla teoria della gravità a scale del megaparsec. Per fare questo, usando i più recenti dati disponibili di survey spettroscopiche di galassie e ammassi di galassie, abbiamo costruito due nuovi cataloghi di galassie membro di ammassi. In particolare, abbiamo sfruttato le coordinate celesti e i redshifts spettroscopici delle galassie all'interno della sedicesima data release (DR16) della Sloan Digital Sky Survey (SDSS; Ahumada et al. [2020]), il catalogo di ammassi di *Wen-Han-Liu* (WHL15; Wen et al. [2015]) e il catalogo di ammassi creato utilizzando le misure della più recente data release del Dark Energy Survey Instrument (DESI; Zou et al. [2021]). Partendo da questi cataloghi pubblici abbiamo costruito un catalogo di galassie membro per ogni campione di ammassi a nostra disposizione. Per effettuare la misura del redshift gravitazionale, abbiamo stimato i centri degli ammassi calcolando la media delle posizioni angolari e dei redshift delle galassie più vicine alla Brightest Cluster Galaxy (BCG). Questo metodo non è mai stato utilizzato prima in letteratura per effettuare misure di redshift gravitazionale. In questo lavoro di Tesi abbiamo dimostrato che questo metodo fornisce una migliore approssimazione del centro della buca di potenziale degli ammassi rispetto alla BCG, che è stata sempre assunta come centro nei precedenti lavori di Wojtak et al. [2011], Jimeno et al. [2014] e Sadeh et al. [2015]. Per l'analisi abbiamo considerato soltanto gli ammassi di alta massa, che si trovano a redshifts bassi, e che hanno un alto numero di galassie membro. Abbiamo applicato queste selezioni al finire di mitigare l'effetto causato dall'includere ammassi non reali nel catalogo. I dati dei membri dei cluster selezionati sono stati mediati all'interno di un singolo diagramma dello spazio delle fasi. Abbiamo corretto i diagrammi dello spazio delle fasi dalla contaminazione delle galassie di foreground e background utilizzando il procedimento descritto da Jimeno et al. [2014]. In seguito abbiamo suddiviso lo spazio delle fasi in quattro intervalli di distanza trasversa e abbiamo modellato la distribuzione di velocità delle galassie, Δ_{mean}, all'interno di ciascuno di essi al fine di misurare lo spostamento della media di queste

distribuzioni, $\hat{\Delta}_{mean}$, in funzione del raggio dell'ammasso, che è proporzionale al segnale del redshift gravitazionale. Inoltre abbiamo costruito un nuovo modello per la calcolare la predizione teorica dell'effetto del redshift gravitazionale, al fine di comparare le nostre misure con le predizioni teoriche di tre diverse teorie della gravità: Relatività Generale, $f(R)$ [Sotiriou and Faraoni, 2010], e i modelli di Dvali–Gabadadze–Porrati (DGP; Dvali et al. [2000]). Abbiamo anche implementato una nuova procedura di analisi statistica al fine di discriminare tra le diverse teorie della gravità utilizzando le misure del redshift gravitazionale. Abbiamo parametrizzato le diverse predizioni teoriche andando a moltiplicare la forza gravitazionale che agisce sui fotoni all'interno dell'ammasso per un parametro, α, che risulta uguale a uno in la Relatività Generale. Abbiamo potuto misurare accuratamente il segnale del redshift gravitazionale in entrambi i cataloghi analizzati. Il risultato ottenuto dalla misura segnale integrato del redshift gravitazionale è pari a $\hat{\Delta}_{mean,int} = -11.4 \pm 3.3$ km s^{-1} per il catalogo di ammassi WHL15, e $\hat{\Delta}_{mean,int} = -14.1 \pm 3.6$ km s^{-1} per il catalogo DESI. Considerando le incertezze di misura, questi risultati sono in accordo con i precedenti lavori di Jimeno et al. [2014] e Sadeh et al. [2015], e con le predizioni teoriche di Cappi [1995] e Kim and Croft [2004]. Il parametro α misurato risulta pari a 0.86 ± 0.25 per il catalogo WHL15 e pari a 1.04 ± 0.28 per il catalogo di membri DESI. Le nostre misure in entrambi i cataloghi sono quindi in accordo con la teoria della Relatività Generale. Inoltre abbiamo studiato le possibili fonti di errori sistematici nella nostra analisi. Per prima cosa abbiamo studiato l'effetto delle nostre selezioni sulla misura di α in entrambi i cataloghi. Infine abbiamo studiato l'impatto delle diverse assunzioni per la stima dei centri degli ammassi

Tutta l'analisi statistica di questo lavoro di Tesi è stata svolta utilizzando le CosmoBolognaLib (CBL; Marulli et al. [2016]), un grande insieme di librerie *free software* in C++/Python, che forniscono un efficiente ambiente numerico per le investigazioni statistiche della struttura su larga scala dell'Universo. Il nuovo modello di likelihood per il fit delle distribuzioni di velocità e il modello per calcolare le predizioni teoriche in Relatività Generale, $f(R)$ e modelli DGP, saranno rilasciati nella prossima versione pubblica delle CBL

Contents

Chapter 1

Intoduction

The Λ-cold dark matter (ΛCDM) cosmological model provides a satisfactory description of the Universe. This model is currently considered the standard cosmological framework. Various assumptions were made to construct the model: the validity of the Cosmological Principle and Einstein's General Relativity, the existence of cold dark matter, the presence of a Cosmological Constant Λ in Einstein's equation and, finally, the existence of an accelerated evolutionary period, called Inflationary Era, in the early phase of the Universe's evolution. The Cosmological Principle states that the Universe is homogeneous and isotropous on the large scale. In other words, if we observe the Universe in any direction its general properties are the same. The dark matter is described as a matter component which only has gravitational interactions with itself and the ordinary matter (Baryons). Dark matter (DM) is considered cold because we think that it is composed of no-relativistic particles. The Cosmological Constant was introduced to explain the late-time accelerated expansion of the Universe and it is associated with the presence of a dark energy component into the Einstein field equations. The physical origin and behaviour of dark matter and dark energy are far to be understood. These two components are required to describe the formation and evolution of cosmic structures and the expansion of the Universe. Furthermore, dark matter and dark energy represent, respectively, the $\sim 27\%$ and the $\sim 68\%$ of the total mass-energy in the Universe, so that only the $\sim 5\%$ of the Universe is composed of ordinary matter and radiation. These percentages highlight the importance to study and understand these two fundamental components. Einstein's theory of General Relativity is the foundation of all the equations that describe how the Universe evolves and the formation of the cosmic structures we can observe today. During the past years, General Relativity was tested only on very small scales, so we do not really know if Einstein's Theory works on the largest scales of the Universe. For this reason, many alternative theories of gravity were proposed to explain the accelerated expansion of the Universe and the growth of cosmic structures, for example the $f(R)$ gravity theories [see De Felice and Tsujikawa, 2010].

Clusters of galaxies are the most massive virialized structures in the Universe. Their predominant component is dark matter, hence they play a crucial role into the presented framework. From the main statistics of galaxy clusters,e.g. number counts and clustering, we

can infer fundamental cosmological information and we can constrain some of the parameters that describe the ΛCDM model, such as the mass density parameter Ω_M and the normalization of the power spectrum σ_8. Furthermore, thanks to the high masses and very deep gravitational potentials of clusters of galaxies, it is possible to test the General Relativity Theory on the scale of these large structures by measuring the gravitational redshift. For the first time, thanks to the data available today, we can directly study the gravity inside these cosmic structures and we can impose constraints on the validity of General Relativity and possibly discriminate among alternative gravitational theories on the scale of million of parsecs.

The aim of this Thesis work is to measure the gravitational redshift inside clusters of galaxies. Exploiting the new available survey data of galaxies (see Ahumada et al. [2020]) and clusters (see Wen et al. [2015] and Zou et al. [2021]), we want to improve the measurements done by Wojtak et al. [2011], Jimeno et al. [2014] and Mpetha et al. [2021]. Thanks to these new data we are able to reduce significantly the errors with respect to literature works. Moreover, we refine the theoretical model to improve the accuracy of the analysis. The huge number of measured redshifts inside our catalog allows us to perform a new Bayesian fit, with the aim of imposing new constraints on the Einstein General Relativity.

This Thesis is organized as follows:

- Chapter 2: we introduce the modern cosmological scenario, describing the main properties of the Universe and the observable parameters through which it is possible to verify the current cosmological model.
- Chapter 3: we present an overview on the general properties of clusters of galaxies and we illustrate the methods used for their detection and to measure their masses.
- Chapter 4: we describe the gravitational redshift in a theoretical context and we briefly underline the differences among the various gravitational theories. Moreover, we present how to compute the model predicted by a certain gravity theory and we briefly illustrate the results in past literature.
- Chapter 5: we introduce and analyze the data set of galaxies and clusters this Thesis work is based on. We describe the method we use to construct the new exploited cluster member catalogs.
- Chapter 6: we describe the method we use to measure the gravitational redshift and we present the final results we obtained.
- Chapter 7: we summarise the main results of this Thesis work and discuss future perspectives.
- Appendix A: we describe the several tests we conduct to investigate the uncertainties possibly affecting our analysis.

Chapter 2

Cosmological Framework

In this Chapter we describe the main theoretical and observational achievements of modern cosmology. In the first part we will provide an overview of the mathematical formalism in cosmology, based on the General Relativity and the Friedmann equations. Then we present the main features of the standard cosmological model, called ΛCDM, that is the cosmological framework on which this Thesis work is based on. Finally, we discuss the theory of evolution of the density and gravitational perturbations in the Universe.

2.1 Cosmological Principles

The standard cosmological model depends on two strong assumptions. The first one is that we can describe the Universe using the Einstein theory of General Relativity (GR, see Einstein [1915]), which describes the gravitational interaction, that becomes predominant on sufficiently large scales. The second assumption is the so-called *Cosmological Principle* (CP). This conjecture states that on the largest scale the Universe is homogeneous and isotropic. The isotropy is the property to look the same in every direction, while the homogeneity is the property of being identical everywhere. Nowadays, we can verify that the Universe follows the CP on scale greater than about $260h^{-1}$ Mpc, using multi-fractal analysis of the large scale matter distribution [Yadav et al., 2010]. The cosmos is an unique and non reproducible object, so a statistical approach would be impossible. To deal with this issue the so-called *Fair Sample Principle* is also assumed. It states that considering distinct volumes of the Universe, sufficiently large to be statistically independent, is equivalent to consider many realizations of the Universe[1].

[1]The volume size we have to consider to satisfy this principle depends on the cosmological time

2.2 Friedmann-Lemaître-Roberston-Walker Metric

Given the first assumption described in the Sec.2.1, we will use GR in order to describe the cosmos. The fundamental idea of this theory is that the content of energy and matter changes the space-time geometry, and the gravitational force is the results of this geometric distortion. In GR the geometrical proprieties of the space-time are described by the *metric tensor*, $g_{\mu\nu}$, and the interval between two events is expressed as:

$$ds^2 = g_{\mu\nu} dx^\mu dx^\nu, \tag{2.1}$$

where both μ and ν run from 0 to 3; the time coordinate is $x_0 = ct$ (c is the speed of light), while x_1, x_2, x_3 are the space coordinates. We can re-write this equation in its explicit form as:

$$ds^2 = g_{00} dt^2 + 2 g_{0i} dx^i dt + g_{ij} dx^i dx^j, \tag{2.2}$$

where $g_{00} dt^2$ is the time component, $2 g_{0i} dx^i dt$ is the mixed component and $g_{ij} dx^i dx^j$ is the spatial one ($i, j = 1, 2, 3$).

Assuming the CP, the mixed components g_{0i} of Eq.(2.2) have to be null. So, the general form for the metric in this case is:

$$ds^2 = c^2 dt^2 - g_{ij} dx^i dx^j = c^2 dt^2 - dl^2. \tag{2.3}$$

In fact, whitin the CP assumption, it is possible to demonstrate that the metric can be expressed as follows:

$$ds^2 = c^2 dt^2 - a(t) \left[\frac{dr^2}{1 - kr^2} + r^2 (d\theta^2 + \sin^2 \theta d\phi^2) \right], \tag{2.4}$$

which is called the Friedmann-Lemaître-Robertson-Walker (FLRW) metric.

In Eq.(2.4) we have used spherical polar coordinates where r, θ and ϕ are called comoving coordinates, while t is the cosmic time. The $a(t)$ factor is the so-called *cosmic scale factor*, which describes how the distances grow or decrease with cosmic time; this parameter is usually normalised so that $a(t_0) = 1$ at the present time. Finally, k is the curvature parameter, that can take only three values: $k = 0$ for flat space (Euclidean space), $k = 1$ for spherical space and $k = -1$ for hyperbolic space. The curvature parameter defines the sign of the *Gaussian Curvature* (C_G):

$$C_G = \frac{k}{a^2}. \tag{2.5}$$

Using the FLRW metric we can derive two important quantities: the *proper distance* (d_p) and the *comoving distance* (d_c). The proper distance is defined as the separation between two points ($P - P'$) measured at the same cosmic time, so we impose that $dt = 0$. For the sake of simplicity, we can set the origin of the reference frame on the point P, so the point P' has coordinates (r, θ, ϕ). Additionally, we can assume that we measure the distance along a radial

geodetic where θ, ϕ are constant, consequently $d\theta = d\phi = 0$. Imposing these conditions in Eq.(2.4) we obtain the proper distance:

$$d_p = \int_0^r \frac{a(t)dr'}{(1-kr'^2)^{\frac{1}{2}}} = a(t)f(r). \tag{2.6}$$

$f(r)$ is a function that depends on the value of the curvature parameter:

- $f(r) = \sin^{-1} r \leftrightarrow k = 1$
- $f(r) = r \leftrightarrow k = 0$
- $f(r) = \sinh^{-1} r \leftrightarrow k = -1$

The proper distance depends on the scale factor $a(t)$, so in an expanding Universe the distance between two points increases with time.

We can define the comoving distance d_c as the proper distance at the present time t_0, then:

$$d_c = d_p(t_0) = a(t_0)f(r) = \frac{a_0}{a}d_p(t). \tag{2.7}$$

2.2.1 Hubble-Lemaître Law

The proper distance changes with time due to expansion of the Universe. Then, by using Eq.(2.6), we can obtain the radial velocity of a source at a point P with respect to the origin of the reference frame:

$$v_r = \dot{d_p} = \dot{a}f(r) = \frac{\dot{a}}{a}d_p. \tag{2.8}$$

This equation is called the *Hubble-Lemaître Law*. The quantity:

$$H(t) = \frac{\dot{a}}{a}, \tag{2.9}$$

is the so-called *Hubble parameter*, which is constant in space at any cosmic time. The Hubble parameter at the present time, $H(t_0) := H_0$, is called the *Hubble constant*. It is conventional to define a dimensionless parameter h, so that $H_0 = h100$ kms s^{-1} Mpc^{-1}. This convention arised from the fact that originally the value of H_0 was not known with great accuracy.
Currently, there is still a possible tension between the value of H_0 measured from the Cosmic Microwave Background (CMB) spectrum and from the distances of Cepheids in nearby galaxies. In particular, ESA Planck Mission measured $H_0 = 67.4 \pm 0.5$ km s^{-1} Mpc^{-1} (see Aghanim et al. [2020],Planck Collaboration 2018, paper VI), while Riess et al. [2019] measured $H_0 = 74.03 \pm 1.42$ kms s^{-1} Mpc^{-1}, which shows a 4.4σ tension. This difference is very debated, possibly indicating systematic uncertainties not accurately modelled, or clues that the ΛCDM requires corrections (see Di Valentino et al. [2021] for a detailed review). The knowledge of

the Hubble constant is fundamental within the standard cosmological model because its value set the Universal distance scale. Moreover, assuming that the Universe expands at constant velocity, we can use H_0 as a proxy of the Universe's age, t_0. The estimated age of the cosmos is 13.800 ± 0.024 Gyr, as described in Aghanim et al. [2020].

2.2.2 Cosmological Redshift

In this Thesis work we exploit the redshifts of millions of galaxies. The measured galaxy redshifts include a contribution from the background expansion and other various contributions that will be described in Chapter 4.

Let us consider a galaxy, with comoving coordinate r, emitting a photon at the time t_e with wavelength λ_e in the source rest frame. An observer, placed in the origin of the coordinate system, receives the signal at the time t_0 and measures a wavelength $\lambda_0 > \lambda_e$. The wavelength shift is called *redshift* and it is defined as:

$$z = \frac{\lambda_0 - \lambda_e}{\lambda_e}. \tag{2.10}$$

This change in the wavelength is primarily caused by the Universe expansion. Specifically, the redshift component due to Universe expansion is called the *cosmological redshift*, and does not depend on the galaxy proper motion (in fact, it is different from the Doppler effect).

Light travels along null geodetics, that is $ds^2 = 0$. Choosing the rest frame where $d\theta = d\phi = 0$, Eq.(2.4) becomes:

$$\int_{t_e}^{t_0} \frac{cdt}{a(t)} = \int_0^r \frac{dr}{\sqrt{1-kr^2}} = f(r). \tag{2.11}$$

Let us assume that both r and $f(r)$ do not change with time, as both the source and the observer are assumed to move with the expanding Universe. Thus, we can consider the light emitted from the source at time $t_0' = t_0 + \delta t_0$ and received by the observer at the time $t_e' = t_e + \delta t_e$, so we can write:

$$\int_{t_e'}^{t_0'} \frac{cdt}{a(t)} = f(r). \tag{2.12}$$

By assuming that δt_0 and δt_e are sufficiently small, from Eq.(2.11) and Eq.(2.12) we can derive that:

$$\frac{\delta t_0}{a_0} = \frac{\delta t_e}{a}, \tag{2.13}$$

where $a = a(t_e)$. We can express the frequencies of emitted and received light as: $\nu_e = 1/\delta t_e$ and $\nu_0 = 1/\delta t_0$, then using the relation between frequency and wavelength we obtain:

$$1 + z = \frac{a_0}{a}. \tag{2.14}$$

This equation relates an observable quantity, the redshift, to the expansion of the Universe, predicting that z increases going back in time. Moreover, it is possible to link the cosmological redshift to the distance and to the cosmic time of the observed object.

2.2.3 Cosmological Distances

To measure the gravitational redshifts in galaxy clusters which is the goal of this Thesis work, it is required to select the cluster member galaxies which lie inside the cluster gravitational potential wells. These galaxies are selected by measuring their distances from the cluster centers. Thus, in the following Section, we describe how distances are measured given a cosmological model.

The proper distance, d_p, is defined as the distance between two objects measured at the same cosmic time, see Eq.(2.6). However, we cannot directly measure this quantity for distant cosmic objects. In order to overcome this problem, two different distance definitions have been introduced: the *luminosity distance*, d_L, and the *angular diameter distance*, d_A.

The former is defined as:

$$d_L = \left(\frac{L}{4\pi l}\right)^{\frac{1}{2}}, \tag{2.15}$$

where L is the luminosity of a source at comoving coordinate r, that emits radiation at the time t. The flux measured by the observer, l, at the time t_0 is expressed as:

$$l = \frac{L}{4\pi a_0^2 r^2}\left(\frac{a}{a_0}\right)^2, \tag{2.16}$$

where $4\pi a_0^2 r^2$ is the surface of a sphere centered at the source position and passing through the observer position. The factor $(a/a_0)^2$ takes in account for the cosmological redshift (Eq.(2.14)) and the time dilatation effect (Eq.(2.13)). Then, it is possible to define d_L as:

$$d_L = a_0^2 \frac{r}{a} = a_0 r(1+z), \tag{2.17}$$

thus, if we know the proper luminosity of a source, we can measure its distance.

The latter, the angular diameter distance d_A, is defined as:

$$d_A = \frac{D_P}{\Delta\theta}, \tag{2.18}$$

where D_P is the proper diameter of a source with comoving coordinate r, and $\Delta\theta$ is the angle subtended by that source. Because of $D_P = ar\Delta\theta$, we can define d_A as:

$$d_A = ar = \frac{a_0 r}{1+z}, \tag{2.19}$$

so it is possible to measure the cosmological distance of a cosmic object, if we know its proper diameter.

Moreover, from Eq.(2.17) and Eq.(2.19) we can define a relation that links d_L and d_A, called the *duality relation*:

$$d_A = \frac{d_L}{(1+z)^2}. \tag{2.20}$$

Thus, if we know the proper diameter and the proper luminosity of a distant source, we can measure d_A and d_L, and we can verify the assumptions of homogeneity and isotropy because the factor $(1+z)^2$ derives directly from the FLRW metric.

Cosmological Horizon

The cosmological horizon, R_H, is the radius defining the spherical region of the Universe in causal connection; it is the space travelled by a free photon from the Big Bang, which is given by:

$$R_H = a(t)c \int_0^t \frac{dt'}{a(t')}. \tag{2.21}$$

The horizon is finite, due to the finite speed of light, and naturally grows in time. The causally connected region grows faster than the speed of light due to the Universe expansion.

2.3 Friedmann Models

The Friedmann models are fundamental in the description of the Universe as a whole. They are based on the FLRW metric, that can be derived from the assumptions of CP and GR. Furthermore, these models describe the Universe content of matter and energy under the assumption that we can consider the Universe as a perfect fluid with pressure p and density ρ.

2.3.1 Friedmann Equations

In Einstein's Theory the metric tensor $g_{\mu\nu}$ is related to the content of energy and matter, defined by the energy-momentum tensor $T_{\mu\nu}$, through the fundamental Einstein's field equation:

$$R_{\mu\nu} - \frac{1}{2} g_{\mu\nu} R = \frac{8\pi G}{c^4} T_{\mu\nu}, \tag{2.22}$$

where $R_{\mu\nu}$ and R are, respectively, the Ricci tensor and the Ricci scalar, G is the Newton's gravitational constant and c the speed of light. Let us describe the Universe as a perfect fluid

with pressure p and energy density ρc^2. Under this assumption, the energy-momentum tensor has the form:

$$T_{\mu\nu} = (p + \rho c^2)u_\mu u_\nu - p g_{\mu\nu}, \tag{2.23}$$

where u_μ is the four-vector that describes the velocity of the fluid.

Using the definition of the energy-momentum tensor for perfect fluids (Eq.(2.23)) and the metric tensor computed from the FLRW metric (Eq.(2.4)) it is possible to demonstrate that the solutions of Eq(2.22) can be written as follows :

$$\ddot{a} = -\frac{4\pi}{3} G \left(\rho + \frac{3p}{c^2} \right) a, \tag{2.24}$$

$$\dot{a}^2 + kc^2 = \frac{8\pi G}{3} \rho a^2, \tag{2.25}$$

these equations, which are dynamical, are known as *Friedmann equations* [Friedmann, 1922]. In order to describe a static Universe, where the large-scale properties do not vary with time, we would have to impose that $\ddot{a} = \dot{a} = 0$. These conditions imply that:

$$\rho = -\frac{3p}{c}. \tag{2.26}$$

In order to have a consistent relation, the pressure or the density has to be a negative quantity, however that is a *non-physical* solution. So, under the assumptions used to derive the Friedmann equations, the Universe cannot be static. This description only works for a Universe composed of ordinary matter, dark matter and radiation, the case of a Universe with a cosmological constant will be examined later.

Moreover, the Friedmann equations are not independent and are linked through the *adiabaticity relation*:

$$d(\rho c^2 a^3) = -p da^3. \tag{2.27}$$

Naturally, the Universe is a closed system, so we can assume that its expansion is an adiabatic process.

2.3.2 General Friedmann Model

The Friedmann equations (Eq.(2.24) and Eq.(2.25)), along with the adiabaticity relation (Eq.(2.27)), allow us to model the time evolution of $a(t)$, $\rho(t)$ and $p(t)$. In order to close the system of equations we need a relation which links density with pressure, the so-called *equation of state*. Because we assume the CP and we describe the Universe as a perfect fluid, the pressure can only be isotropic, then the general equation of state is expressed as:

$$p = w\rho c^2, \tag{2.28}$$

where w is a constant parameter which value, for ordinary matter, can only be inside the interval $0 \leq w < 1$, called the *Zel'dovich interval*. In particular we can assume $w = 0$ for pressureless matter (dust), which is a good approximation for fluids made of no-relativistic gas. On the other hand, $w = 1/3$ for fluids made of photons or ultra-relativistic particles in thermal equilibrium. The case $w = -1$, which is associated to the cosmological constant, will be examined later. Therefore, combining Eq.(2.27) and Eq.(2.28), we retrieve the laws that describe the evolution of the density:

$$\rho_w = \rho_{0,w} \left(\frac{a}{a_0} \right)^{-3(1+w)} = \rho_{0,w}(1+z)^{3(1+w)}. \tag{2.29}$$

Thus, the evolution for the dust, given $w = 0$, results:

$$\rho_m = \rho_{0,m} \left(\frac{a}{a_0} \right)^{-3} = \rho_{0,m}(1+z)^3. \tag{2.30}$$

On the other hand, the evolution for relativistic particles and photons, given $w = 1/3$, is:

$$\rho_r = \rho_{0,r} \left(\frac{a}{a_0} \right)^{-4} = \rho_{0,r}(1+z)^4. \tag{2.31}$$

So, the density of dust and photons decreases with time, as the Universe expands. The dust density decreases as the cube of the scale factor because the number of particles is constant, then the density drops due to the Universe's volume growth. We are describing the energy density of the universal fluid, then for relativistic particles and photons we have to take into account the effect of cosmological redshift that changes wavelength by a factor equal to a. This explains the exponent 4 in Eq.(2.31).

Now we focus on the evolution of the scale factor $a(t)$. We calculate the Eq.(2.25) at the present time t_0 and we divide the result by a factor a_0^2, so we obtain:

$$H_0(1 - \Omega_{0,w}) = -\frac{kc^2}{a_0^2}, \tag{2.32}$$

where $\Omega_{0,w}$ is the *density parameter* for a generic component of the cosmic fluid, that is defined as:

$$\Omega_{0,w} = \frac{\rho_{0,w}}{\rho_{0,c}}, \tag{2.33}$$

where $\rho_{0,c}$ is the *critical density* of the Universe at the present time. Generally, it is possible to define $\rho_c(t)$, the critical density at any cosmic time as:

$$\rho_c(t) = \frac{3H^2(t)}{8\pi G}. \tag{2.34}$$

Thus, combing Eq.(2.32) and Eq.(2.25) considered at generic time t, we obtain the relation that describe the evolution of $H^2(t)$:

$$H^2(t) = H_0^2 \left(\frac{a_0}{a}\right)^2 \left[1 - \Omega_{0,w} + \Omega_{0,w} \left(\frac{a_0}{a}\right)^{1+3w}\right]. \tag{2.35}$$

This is the equation for a singular fluid component, while for a Universe composed of multiple components it is possible to express the above relation as follows:

$$H^2(t) = H_0^2 \left(\frac{a_0}{a}\right)^2 \left[1 - \sum_i \Omega_{0,w_i} + \sum_i \Omega_{0,w_i} \left(\frac{a_0}{a}\right)^{1+3w_i}\right]. \tag{2.36}$$

The total density parameter is defined as the sum over all the components, that is $\sum_i \Omega_{w_i} = \Omega_{TOT}$. It is possible to demonstrate that this parameter determines the geometry of the Universe:

- $\Omega_{TOT} = 1 \rightarrow \rho = \rho_c \rightarrow k = 0$: flat Universe.
- $\Omega_{TOT} < 1 \rightarrow \rho < \rho_c \rightarrow k = -1$: open Universe.
- $\Omega_{TOT} > 1 \rightarrow \rho > \rho_c \rightarrow k = +1$: flat Universe.

Given the definition of the density parameter (Eq.(2.33)) and combining that with Eq.(2.25), we retrieve the law which describes the evolution of Ω_w with redshift:

$$\Omega_w^{-1}(z) - 1 = \frac{\Omega_{0,w}^{-1}(z) - 1}{(1+z)^{1+3w}}. \tag{2.37}$$

This relation demonstrates that the time evolution cannot change the Universe geometry. So, the decrease of ρ_w with the Universe expansion does not change the sign of the curvature parameter k.

The Big Bang

Assuming the Friedmann equations, in particular Eq.(2.25), and combining that with the equation of state (Eq.(2.28)), we obtain:

$$\ddot{a} = -\frac{4\pi G}{3}(1+3w)\rho a. \tag{2.38}$$

Considering the above equation, it is clear that $\ddot{a} < 0$ for $w > -1/3$ (always true for ordinary matter which is inside the Zel'dovich interval). Thus, the Universe has a decelerated expansion. Going back through cosmic time there would be a moment when $a(t) = 0$, the so-called *Big Bang* (BB). Looking at Eq.(2.29), if $a = 0$, then $\rho \rightarrow \infty$. The BB is a singularity where the known physics does not work and it is not avoidable in a model of Universe based on Friedmann Equations with w inside the Zel'dovich interval.

Cosmological Constant

As said previously, it is straightforward to see, by looking at the Eq.(2.24), that the expansion of the Universe can only be decelerated for Universe with only ordinary matter and radiation. However, observations demonstrate that Universe is currently undergoing an accelerated expansion [see Riess et al., 1998]. The simplest possible way to explain this evidence is to change Eq.(2.22) by adding a constant component, Λ, in the GR field equation. Physically, this is equal to consider a new and unknown energy component in the Universe, the so-called *dark energy*. Then, the energy-momentum tensor can be modified as:

$$\tilde{T}_{\mu\nu} = T_{\mu\nu} + \frac{\Lambda c^4}{8\pi G} g_{\mu\nu} = -\tilde{p} g_{\mu\nu} + (\tilde{p} + \tilde{\rho} c^2) u_\mu u_\nu, \tag{2.39}$$

where

$$\tilde{p} = p - \frac{\Lambda c^4}{8\pi G}, \quad \tilde{\rho} = \rho + \frac{\Lambda c^2}{8\pi G}, \tag{2.40}$$

$\tilde{p}$ and $\tilde{\rho}$ are the effective pressure and density. We associated the pressure and density of the dark energy with:

$$p_\Lambda = -\frac{\Lambda c^4}{8\pi G}, \quad \rho_\Lambda = \frac{\Lambda c^2}{8\pi G}. \tag{2.41}$$

Thus, the dark energy can be described as a fluid with $w = -1$. This value is outside the Zel'dovich interval, so dark energy is not ordinary matter. Moreover, given Eq.(2.29), we obtain that:

$$\rho_\Lambda = \rho_{0,\Lambda}. \tag{2.42}$$

Then, the dark energy density does not vary with the Universe expansion. In order to explain the accelerated expansion we need to add this new component into the Friedmann equations described above. We underline that it is possible to achieve the same result by changing the left side of the Einstein field equation, adding $\frac{\Lambda c^4}{8\pi G} g_{\mu\nu}$. Mathematically, a change in the left or the right side of Eq.(2.22) is the same and we obtain identical results for the Universe evolution, but physically it is not. Changing the energy-momentum tensor it is equal to add a new component into Universe fluid. On the other hand, changing the left side of the equation means transforming the gravity theory. To explain the Universe accelerated expansion without the dark energy component, many alternative gravity theories have been developed over the years, such as the $f(R)$ theory (see Sotiriou and Faraoni [2010]) and the Dvali–Gabadadze–Porrati (DGP) models [Dvali et al., 2000].

Density and Scale Factor Evolution in Friedmann Models

The Eq.(2.29) describes the time evolution of the density for a singular fluid component. The equation depends on the parameter w in the equation of state (Eq.(2.28)). Thus, as shown in Eq.(2.30), Eq.(2.31) and Eq.(2.42), different components have different evolutions. Due to this fact, we expect that in different Universe epochs there are distinct dominant components.

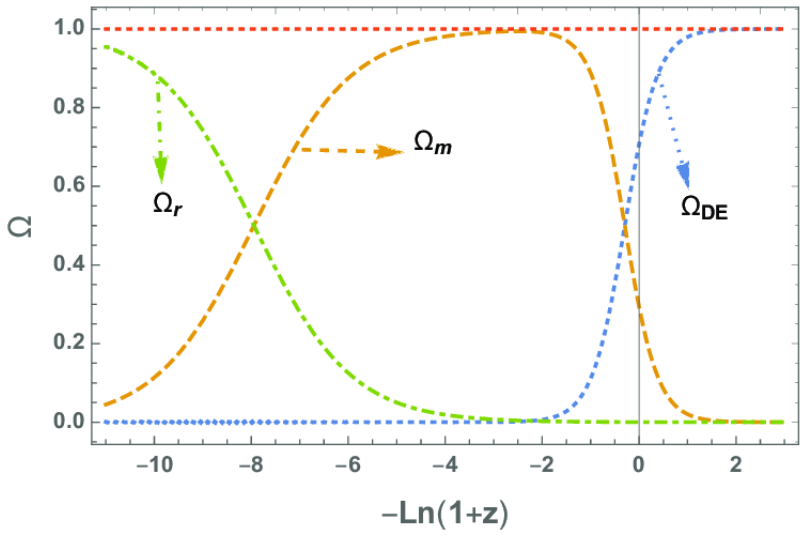

Figure 2.1: Evolution of density parameters in function of the redshift. Radiation parameter (green dash-dotted line), matter parameter (orange dashed line) and dark energy parameter (blue dotted line). The red dotted line represents Ω_{TOT}, which has value equal to one for every redshift, due to Universe flatness. Credtis to: Granda [2020].

Figure 2.1 shows the evolution of the density parameters, accordingly to Eq.(2.37). It is clear that in early-time radiation was dominant, then matter became the dominant component, while, nowadays, dark energy and matter have almost the same density. In particular the values of density parameter at present time are: $\Omega_{0,m} \sim 0.3$, $\Omega_{0,\Lambda} \sim 0.7$ and $\Omega_{0,r} \sim 10^{-4}$. We highlight that $\Omega_{TOT} = \sum \Omega_{w,i}$ describes the Universe geometry and here it is set equal to one (flat Universe), due to CMB measurements [see Aghanim et al., 2020]. The time when the density parameter of different components have the same value is called the *equivalence time* (t_{eq}). During the Universe history there were two different equivalence times:

1. radiation-matter equivalence $\rightarrow \Omega_r = \Omega_m$ at $z_{eq,rm} \sim 10^4$.
2. matter-Λ equivalence $\rightarrow \Omega_m = \Omega_\Lambda$ at $z_{eq,m\Lambda} \sim 0.7$.

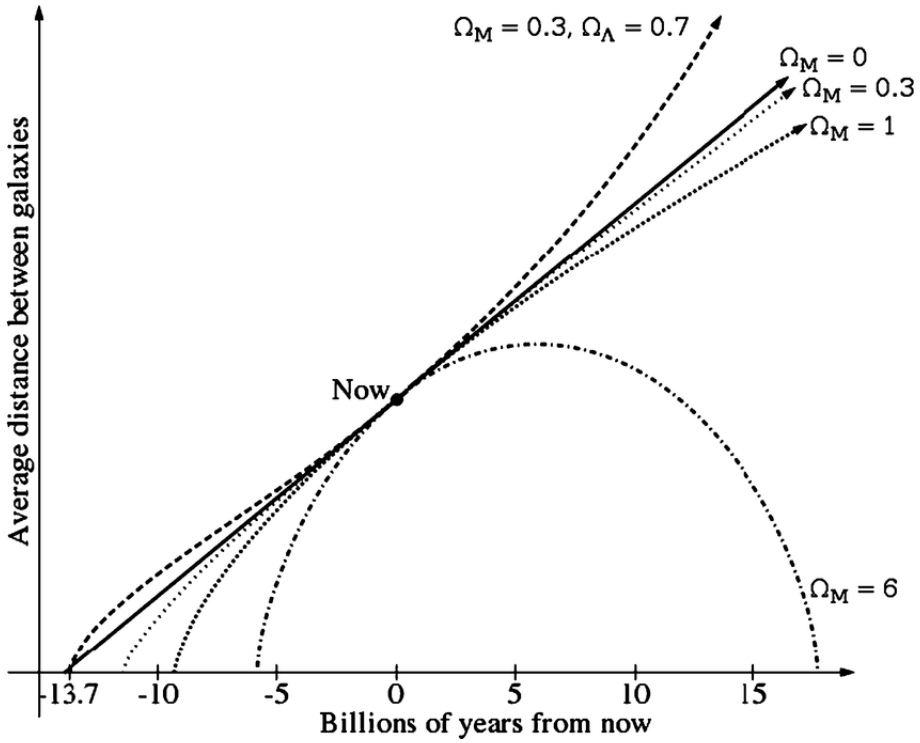

Figure 2.2: Time evolution of the scale factor in arbitrary units for different cosmological models as a function of the matter density parameter Ω_m and the dark energy density parameter Ω_Λ. Closed Universe with $\rho > \rho_c$ (dot-dashed line) ending up collapsing in a second singularity (Big Crunch); flat Universe with $\rho = \rho_c$ (pointed line); open Universe (solid line) with $\rho < \rho_c$ ending up in a Big Freeze (heat death); Universe with dark energy (dotted line), as assumed in ΛCDM model. Credits to: Casado [2013].

Figure 2.2 shows the time evolution of the scale factor $a(t)$. We highlight that Eq.(2.36), which describes how the Universe expands, depends on the Universe geometry and the components of the cosmic fluid. Thus, for different geometries we retrieve different universal histories. Figure 2.2 shows that a closed Universe ($\Omega_{TOT} > 1$) has an initial expansion phase, then reaches the maximum scale factor, a_{max}, finally enters in a contraction phase which ends up in a singularity, called *Big Crunch*. Flat and open Universes expand forever, in particular an open Universe grows faster than a flat Universe. The ΛCDM Universe has the fastest expansions and, unlike the other scenarios, has a late time accelerated growth. Figure 2.2 shows also that the age of the Universe is different in the various cases. In particular the ΛCDM Universe is the oldest, while closed Universes are the youngest.

2.4 Standard Cosmological Model

In this Section we describe the standard cosmological framework which is also assumed in this Thesis.

By solving the Friedmann equations we can obtain the so-called *Hot Big Bang Model* (BB). This model is currently largely accepted because its predictions can be extensively verified through several independent observations. The BB model explains various phenomena such as: the Hubble flow, the abundance of light elements and the presence of the CMB. The latter is the black-body radiation which permeates the Universe. It is the black-body radiation which started to freely propagate when the first recombination of the free electrons occurred. Moreover, CMB is one of the strongest evidences of the Big Bang. This model is called *Hot* because, going back to the time close to singularity, the Universe became hotter and hotter and reached a temperature of almost 10^{40} K at the so-called *Planck time*. We describe the Universe evolution as a thermal history because, from the Big Bang moment, the temperature drops and reach the present day temperature $T_0 = 2.73K$ (the CMB temperature). The ΛCDM model, the present day standard cosmological model, is based on the hot BB model. In order to explain the Universe flatness (observed through CMB) and the whole uniformity of CMB, it seems convenient to assume the existence of the *inflation* in Universe's early epoch. The inflation is a period of exponential accelerated expansion of the Universe. Moreover, the inflationary era gives rise to the density perturbations which originate the cosmic structures observed today. One of the fundamental aspects of the standard model is the presence of the dark energy component Λ. As said previously, it is necessary to add this component to explain the accelerated expansion of the present day Universe. Furthermore, from CMB measurements we have $\Omega_{TOT} \simeq 1$, while primarily from dynamical studies of galaxies and galaxy clusters we retrieve the value of the matter density parameter Ω_m. Then, the presence of the dark energy is necessary to explain also the Universe flatness. The other fundamental aspect of the ΛCDM model is the existence of the *cold dark matter* (CDM). The dark matter represents the majority of the matter in the Universe, everything else is baryonic matter. Standard dark matter is assumed to interact only through gravitational force. Its existence could be verified by only indirect observations, in particularly gravitational lensing (e.g. Li et al. [2016]), studies of rotation curves of late-type galaxies (e.g. Fuchs [2001]) or dynamical studies of galaxy clusters (e.g. Zwicky [1933]). We refer to dark matter as cold because, in order to explain the cosmic structures formation and growth (see Sec.2.6), DM has to be composed of massive particles, which must be non-relativistic at the decoupling time. Indeed, one of the main problem of ΛCDM model is the understanding of what DM is composed of. It is necessary to highlight that it is possible to avoid the problem of DM by modifying the Einstein theory of General Relativity, by explaining this mass excess with gravitation itself (see Joyce et al. [2016] for a review on modified gravity models).

During this Thesis work all the cosmological calculations are performed assuming a flat ΛCDM cosmology, with $\Omega_m = 0.3153$ and the Hubble constant $H_0 = 67.36\,\mathrm{km\,s^{-1}\,Mpc^{-1}}$, see Aghanim et al. [2020] (Planck collaboration 2018, Paper VI:Table 2, TT,TE,EE+lowE+lensing).

Moreover, the whole cosmological analysis of this Thesis work has been performed with the CosmoBolognaLib (CBL; Marulli et al. [2016]), a large set of *free software* C++/Python libraries, that provide an efficient numerical environment for statistical investigations of the large-scale structure of the Universe. The new likelihood functions for fitting the velocity distributions and computing GR and the alternative gravity theories predictions, will be released in the forthcoming public version of the CBL.

2.5 Theory of Linear Perturbations

In this Thesis work we will exploit a large sample of clusters of galaxies. Thus, in order to present a general overview of these cosmic structures during the following Sections, we briefly describe here the cosmological theory of formation and evolution of these objects.

The gravitational bound structures in the Universe descend from the growth of small density perturbations. Such perturbations were originated in the early epoch of the Universe, after the inflationary era. We can observe that through the temperature fluctuations in CMB. Thus, from the study of the *growth factor*, the growth rate of these perturbations, it is possible to infer fundamental parameters of the ΛCDM model, such as $H(z)$ and Ω_m. In the CMB we observe the perturbations at $z \sim 1100$ with a very small *density contrast* δ:

$$\delta = \frac{\rho - \bar{\rho}}{\bar{\rho}} = \frac{\delta\rho}{\bar{\rho}} \sim 10^{-5}, \tag{2.43}$$

where $\bar{\rho}$ is the mean density of the Universe. Because of the small perturbations at very high redshift, we can model the growth factor $\delta(t)$ by using the linear approximation of fluid dynamic equations. However, in the present Universe we observe structures with density contrast of $\sim 100 - 100$, then, in order to describe that, it is necessary to use non linear theories or N-body simulations.

2.5.1 Jeans Theory

The linear model of structure formation is based on the so-called Jeans gravitational instability theory, [Jeans, 1902]. This theory describes how small density perturbations evolve over time into a static, homogeneous and isotropic background fluid. The general idea, indeed, is that density perturbations that exceed a critical scale in this fluid can trigger a gravitational collapse, which would result in a growth of these perturbations. the gravitational collapse of dark and baryonic matter is not that trivial and involves several hydrodynamical and dynamical effects, such as gas heating and the increase of the angular momentum due to the baryonic matter interactions. These effects can not be described in a linear regime. On the largest scales the dominant matter contribution is given by dark matter, which is weakly interactive, therefore does not undergo the physical processes of the gas.

Let us consider a spherical inhomogeneity of radius R, into a background fluid of mean density $\bar{\rho}$, with mass M and a positive density fluctuation $\delta\rho$:

$$\delta\rho = \rho - \bar{\rho} > 0. \tag{2.44}$$

The absolute value of the gravitational potential energy E_p must exceed the internal kinetic energy E_k to have the collapse of this perturbation. Then, by using the condition $E_p > E_k$, it is possible to retrieve the collapse condition:

$$R > R_J = \frac{v}{\sqrt{2G\rho}}, \tag{2.45}$$

where R_J is the so-called *Jeans Radius*. A perturbation which grows over the scale defined by the Jeans radius, starts to collapse as the gravitational force becomes dominant.

Having introduced the principles of the gravitational collapse, we can now proceed with a more detailed discussion of the perturbations' evolution. Moreover, we have to deal with the fact that the Universe expands and this expansions is in contrast with gravitational force that causes the perturbations' growth.

2.5.2 Jeans Theory in Expanding Universe

Assuming the Universe as a perfect fluid, we can characterised it by its density ρ, pressure p, velocity $\vec{v}$, gravitational potential ϕ and entropy S, through the following hydrodynamic equations:

$$\begin{cases} \frac{\partial\rho}{\partial t} + \nabla\cdot\rho\vec{v} = 0 & \text{continuity equation} \\ \frac{\partial\vec{v}}{\partial t} + (\vec{v}\cdot\nabla)\vec{v} = -\frac{1}{\rho}\nabla p - \nabla\phi & \text{Euler equation} \\ \nabla^2\phi = 4\pi G\rho & \text{Poisson equation} \\ p = p(S,\rho) & \text{equation of state} \\ \frac{dS}{dt} = 0 & \text{entropy conservation} \end{cases} \tag{2.46}$$

It is possible to describe the primordial fluctuations as adiabatic perturbations, therefore $S = const$ and $p = p(\rho)$ (from CMB observations, see Aghanim et al. [2020], Planck Collaboration, paper VI). We consider the following background solutions:

$$\begin{cases} \rho_B = \rho_B(t) \\ \phi_B = const \\ \vec{v}_B = H(t)\vec{x} \\ p_B = p_B(\rho_B) \end{cases} \tag{2.47}$$

We perturb the hydrodynamic equations (Eq.(2.46)) by adding a small perturbation $\delta x \ll 1$ and we consider only the linear terms. Finally, we look for solutions to the perturbed system

as *plane waves*:

$$f(\vec{r},t) = f_k \exp\left(i\vec{k}\cdot\vec{r} + i\omega t\right), \tag{2.48}$$

where $\vec{r}$ is the spatial vector, f_k is the wave amplitude, k is the wave number, $\vec{k} = 2\pi\hat{k}/\lambda$ is the wave vector, $\hat{k}$ is the wave versor and ω is the angular frequency. Thus, we search solutions in the Fourier space, by calculating the so-called *dispersion relation* ($\omega(\vec{k})$). In order to find the evolution of the so-called *density contrast*, defined as:

$$\delta(\vec{x},t) = \frac{\rho(\vec{x},t)}{\rho_B}, \tag{2.49}$$

we need to consider the scale and the cosmic time. In fact, we will have different solutions for perturbations inside or outside the cosmological horizon.

2.5.3 Outside Cosmological Horizon

For scales larger than the cosmological horizon (R_H, Eq.(2.21)) the gravity is the only important interaction. Thus, we can neglect the micro-physics, we do not use the hydrodynamics equations, and we describe the problem through the GR. In this scenario, we can consider the perturbations like a closed Universe ($\Omega_{TOT} > 1$) described by Friedmann equations. We assume these perturbations are immersed in a flat Universe with a singular dominant component (the so-called *Einstein-de Sitter Universe*). Considering these assumptions during the different Universe periods, in which we can consider only the dominant component coupled with the other through gravitation for $R > R_H$, we have:

- For $t < t_{eq,rm}$ the Universe is dominated by radiation, so $w = 1/3 \rightarrow \delta_r \propto \delta_m \propto a^2$.
- For $t_{eq,m\Lambda} > t > t_{eq,rm}$ the Universe is dominated by matter, so $w = 0 \rightarrow \delta_m \propto \delta_r \propto a$.

2.5.4 Inside Cosmological Horizon

For $R < R_H$ we have to consider the gas physics, thus we have to consider the hydrodynamics equations in an expanding Universe.

Radiation Era

The Universe at $t < t_{eq,rm}$ is dominated by radiation and relativistic particles. Solving the dispersion's equation to study the the temporal evolution of the density perturbations leads to:

$$\delta_+(\vec{x},t) \propto a, \tag{2.50}$$

for $R_H > R > R_J$ (δ_+ is called the *growing solution*). This solution is relevant, because it can lead to gravitational instability.

However, during the Radiation Era the Universe was completely dominated by a fluid of photons and relativistic particles. Therefore, because the baryonic matter was coupled to the radiative fluid via frequent scattering, the huge radiation pressure prevents the perturbations from collapsing. On the other hand, dark matter consists of colliosionless particles, thus it has a different evolution relative to baryons. It is possible to demonstrate that a dark matter perturbation, for $R_H > R > R_J$, grows at most by a factor of $5/2$, instead of growing proportionally to $a(t)$. This phenomenon is called *stagnation effect* or *Meszaros effect* [see Meszaros, 1974].

Matter Era

The Universe at $t > t_{eq,rm}$ is dominated by the matter, so the radiation pressure is negligible. We consider a mono-component and flat Universe ($\Omega_{TOT} = 1$, $\omega = 0$). Thus, by solving the dispersion's equation and by searching for solutions with a power law form, we obtain:

$$\delta_+(\vec{x}, t) \propto a, \tag{2.51}$$

for $R_H > R > R_J$. We highlight that this solution is valid for every type of matter. However, dark and baryonic matter interact through gravity but dark matter decouples from the radiation much before baryons. Therefore, dark matter, from the decoupling moment, grows proportional to the expansion factor $a(t)$. On the other hand, when baryons also decoupled from the radiation (at $t = t_{dec}$), the dark matter perturbations have already grown. For that reason, the baryonic matter immediately falls into the gravitational potential wells of the dark matter haloes. Hence, the baryonic perturbations grows following the relation:

$$\delta_b \propto \delta_{DM} \left(1 - \frac{a_{dec}}{a}\right). \tag{2.52}$$

This phenomenon is called *baryon catch-up* (see Fig.2.3). This phenomenon is necessary in order to explain the values of δ_b we observe today ($\delta_b \sim 10^3$ inside galaxy clusters). Indeed, without the baryon catch-up we expect $\delta_b \sim 10^{-2}$.

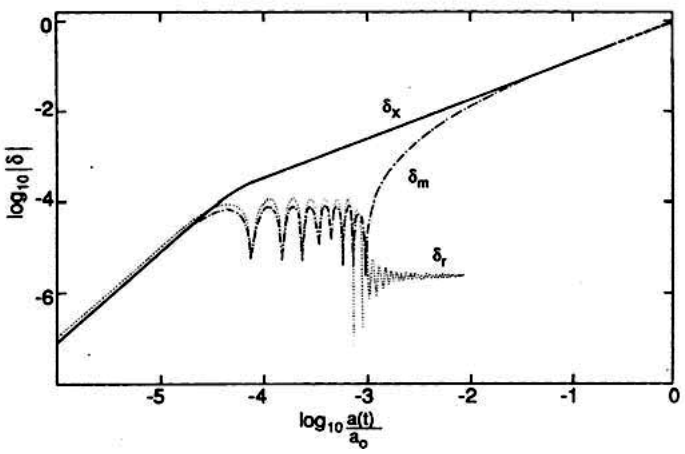

Figure 2.3: Evolution of density perturbations for cold dark matter δ_x, baryonic matter δ_m and radiation δ_r components; at mass scale $M \sim 10^{15}$ $M_\odot$ in a Universe with $\Omega_{TOT} = 1$. Credits to: Coles and Lucchin [2008].

In the general case an analytical expression for $\delta_+(t)$ does not exist, for a Universe with multiple components and whatever geometry, but the approximate formula of the so-called *growing factor* (f) is used:

$$f \equiv \frac{d\ln(\delta_+)}{d\ln(a)} \simeq \Omega_m^\gamma + \frac{\Omega_\Lambda}{70}\left(1 + \frac{\Omega_m}{2}\right). \tag{2.53}$$

This expression is extremely important because the γ-term depends on the gravity theory ($\gamma \simeq 0.55$ for GR). Therefore the measure of f allow us to discriminate among different gravity theories.

2.6 Non Linear Theory

In Sec.2.5 we have described the evolution of primordial perturbations, which is based on the assumption of linearity $\delta(\vec{x}, t) < 1$. However, nowadays we observe structures, like galaxy clusters, characterised by a density contrast of about 10^3. Thus, in order to understand the formation of cosmic structures, it is necessary to elaborate a non linear theory.

An analytic approach to the collapse of cosmic structures is the spherical collapse model, which leads to the Press & Schechter formalism of the mass function. However, in general it is necessary to use numerical methods in order to accurately describe the structures in the Universe. In fact, the exploitation of N-body simulations is mandatory in several cases.

2.6.1 Spherical Collapse

In the non linear regime, it is possible to obtain an analytical solution only for an isolated and spherical perturbation, initially at rest. The perturbation can detach from the background density field and possibly collapses in a finite timescale. Assuming a generic background Universe where the perturbation is immersed, we obtain the following relations:

$$\begin{cases} \delta(t) = \frac{3}{5}\delta_+(t_i)\left(\frac{t}{t_i}\right)^{\frac{2}{3}} \\ \delta_+ > \frac{3}{5}\frac{1-\Omega_{bkg}(t_i)}{\Omega(t_i)(1+z_i)} \end{cases} \tag{2.54}$$

where t_i is the initial time, Ω_{bkg} is the density parameter of the background and Ω is the density parameter of the perturbation.

Initially, the overdensity follows the background dynamics, but it has a deceleration caused by gravitational interactions. Thus, the overdensity stops at the so-called *turn-around epoch* and starts to evolve independently from the background. The collapse of the perturbation starts at the so-called *turn-around time* (t^*), when the perturbation is already nonlinear. Indeed, by assuming a flat and matter dominated background Universe, we obtain $\delta_+(t^*) \simeq 180$. Then, the collapsed structure may reach the virialisation at $t_{vir} \simeq 3t^*$, obtaining a bound object which is usually called *halo*. Using an extrapolation of the linear growth theory, for which $\delta_+ \propto a(t)$, we obtain $\delta_+(t^*) \simeq 1.68$.

Mass Function

In order to test the ΛCDM cosmological model, it is necessary to link it to observables. One of the most exploited observable is the *mass function*, which describes the number of objects with a mass between M and $M + dM$, at a given time, per unit of comoving volume. The mass function is linked to the halo formation and evolution and particularly, the mass function of cosmic structure is defined as:

$$\frac{dn(M,z)}{dM} = f(\sigma(M,z))\frac{\bar{\rho}}{M}\frac{d\ln\sigma(M,z)^{-1}}{dM}, \tag{2.55}$$

where $f(\sigma(M,z))\bar{\rho}$ defines the amount of mass contained in fluctuations with mass M at redshift z, and $\sigma(M)$ represents the mass variance. The most common form of the mass function is the so-called *Press-Schechter mass function* (see Press and Schechter [1974]), which is modeled using the linear theory of perturbations and is defined as:

$$n(M,z)dM = \sqrt{\frac{2}{\pi}}\frac{\delta_c\bar{\rho_M}(z)}{\sigma_M(z)M^2}\left|\frac{d\ln\sigma(M)}{d\ln M}\right|\exp\left(-\frac{\delta_c}{2\sigma_M^2(z)}\right), \tag{2.56}$$

where $\delta_c \simeq 1.68$, which is the threshold value for having a collapse in the linear theory. The form of this mass function is that of a power-law, with an exponential cut from a certain value of the mass, called the *characteristic mass* M_* (see Fig.2.4). The value of M_* increases in

time, at the present days $M_* \simeq 10^{15}\,\mathrm{M}_\odot/h$, which is the typical mass of galaxy clusters. Thus, counting the number of clusters in the local Universe is equivalent to counting how much mass is contained in the exponential tail of the mass function.

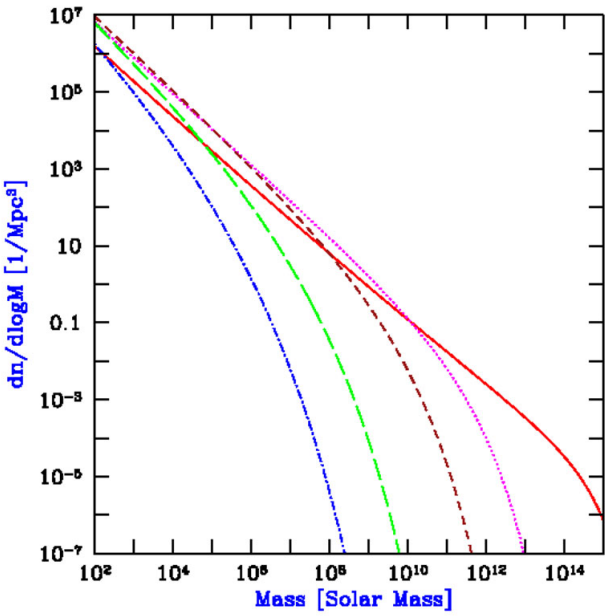

Figure 2.4: Halo mass function at several redshift: $z = 0$ (solid curve), $z = 5$ (dotted curve), $z = 10$ (short-dashed curve), $z = 20$ (long-dashed curve), and $z = 30$ (dot-dashed curve). Credits to: Loeb [2006].

2.6.2 N-Body Simulations

As we mentioned, we can exploit numerical simulations to study the non linear evolution of matter density perturbations. The fundamental advantage of the N-body simulations is that the growth in non linear regime can be investigated without the necessary assumptions adopted in analytical models. In the large-scale structure of the Universe, the evolution is dominated by the gravitation so, at the first order, it is sufficient to study the behaviour of the dark matter component. However, in order to obtain a more realistic description of the formation and evolution of cosmic structures also the baryonic component must be considered. This implies that we need to take into account also the hydrodynamic interactions, in particular: the gas cooling process, the star formation, the supernova and AGN feedback and the chemical enrichment. An overview over the N-body simulations in cosmology is presented in Moscardini and Dolag [2011].

Chapter 3

Clusters of Galaxies

Galaxy clusters are the biggest virialized structures present in the Universe. They lie on the highest peaks of the dark matter density field. Their masses can reach $\sim 10^{15}$ $M_{\odot}$, while their radii $2-3$ Mpc. These cosmic structures are critically important in cosmology because we can link their observed properties to the physical quantities of their host halos of dark matter, that we can model as a function of ΛCDM parameters. In this Chapter we will describe the main peculiarities of galaxy clusters and how we can infer their properties. Also, we will illustrate how we detect these objects, and their relevance in cosmological studies.

3.1 Galaxy Clusters Overall Properties

Galaxy clusters can be detected and observed using a multi-wavelength approach. Deep studies of these objects have been performed in X-ray, optical, Near Infrared (NIR), radio, and also using the technique of the gravitational lensing. With their large mass, these cosmic structures generate a very deep potential well where member galaxies reside. Typically, clusters contain about $500-1000$ member galaxies, that can reach velocity dispersions of thousands kilometer per seconds due to the cluster gravitational potential. The main components of these objects are: galaxies ($2\%-5\%$), Intra-Cluster Medium (ICM, $11\%-15\%$) and dark matter ($80\%-88\%$) (for more details see Kravtsov et al. [2012]). These percentages refer to the mass fraction of the singular component, so clusters are dark matter dominated structures.

The typical galaxy cluster population is composed of early-type galaxies (ETGs), elliptical and lenticular galaxies, that had ended up their star formation phase at $z \sim 2$. This type of galaxies are passive and lie in the cluster central region. These member galaxies, in a color-magnitude diagram (e.g. a (B-R)-R diagram), usually shape a particular sequence, called *red sequence*. This sequence is a narrow linear relation between magnitude and color which shows that redder galaxies are brighter. In the cluster outskirt we can also find star forming galaxies (SFGs), usually in clusters that undergo a recent wet merger. The so called Central Dominant Galaxy (CD galaxy), that can reach a mass of $\sim 10^{12}$ $M_{\odot}$, is situated in the very center of a

cluster. This galaxy is usually the Brightest Cluster Galaxy (BCG) and hosts an Active Galaxy Nuclei (AGN), which is a Super Massive Black Hole (SMBH) that radiates a great amount of energy in all the wavelengths, due to the infall of the gas that surrounds it.

The dark matter halo, where the baryonic matter resides, represents the dominant matter component. Because dark matter mass is $1-2$ orders of magnitude higher than the mass of all baryons, we assume that ICM and galaxies are in equilibrium inside the same potential well generated by the DM halo. The density profile of the halo at any mass and redshift is generally modelled by the Navarro-Frank-White (NFW) radial profile [Navarro et al., 1995], which was obtained from N-body simulations. Obviously it is a mean profile, real clusters have different merger histories and may not be completely relaxed.

The ICM accounts for most of the baryonic matter contained in a cluster and it is responsible for the cluster's diffuse X-ray emission. The ICM is a diffuse plasma that is not associated with singular galaxies and it has an average free electron density of $n_e \sim 10^{-3}$ cm^{-3} and a typical temperature of $\sim 10^7 - 10^8$ K. This plasma, due to the high temperature and low density, emits by thermal bremsstrahlung, with a characteristic luminosity in the X-ray of $L_X \sim 10^{43} - 10^{45}$ erg/s. The classical way to describe the ICM density radial profile is the β-model [Cavaliere and Fusco-Fermiano, 1976]. The basic idea of this model is that the ICM and galaxies are nearly in equilibrium within the gravitational potential well generated by the dark matter halo. The β-model is a flat profile near the centre and decreases towards the outskirt. It is described by the following equation:

$$\rho_{gas} = \frac{\rho_0}{[1 + (\frac{r}{r_c})^2]^{\frac{3}{2}\beta}}, \tag{3.1}$$

where r_c is the core radius and ρ_0 is the central density. The parameter β is the ratio between the kinetic energy of galaxies, defined by their one-dimensional velocity dispersion σ^2, and the gas thermal energy:

$$\beta = \frac{\mu m_p \sigma^2}{k_B T}, \tag{3.2}$$

where μ is the mean molecular weight, m_p is the proton mass and k_B is the Boltzmann constant.

The equilibrium assumption is valid only for relaxed clusters, usually called *cool-core clusters*. The assumption is not valid for clusters that present a central peak in the density profile, called *non-cool-core clusters*. These objects experienced a recent major merger and therefore the gas did not have time to return to equilibrium.

The central regions in relaxed clusters are denser than the outskirt. For this reason, gas cooling due to energy loss by radiation is more efficient there and the temperature is lower [Fabian, 1994]. However, spectroscopic observations with Chandra and XMM-Newton satellites have shown that the fraction of ICM gas cooling down to low temperatures is smaller than expected [Peterson et al., 2001]. This conundrum is called the Cooling Problem and can be solved by invoking various mechanisms, such as the AGN feedback from the central CD galaxy [see Vernaleo and Reynolds, 2006] or the heating produced by the gas turbulence [see Zhuravleva et al., 2014].

3.2 Clusters Detection and Mass Estimation

Several methods are used to detect clusters of galaxies and estimate their masses. When studying galaxy clusters, one of the main issues is to estimate their mass. Since it cannot be directly observed, we have to deduct the mass using observable properties, called *mass proxies*. So far, different proxies in various wavelengths have been used in numerous scaling relations, which are based on the assumption of fundamental physical processes or have been empirically calibrated on observations (see Godini et al. [2013] for a detailed overview).

3.2.1 X-Ray

The ICM is mostly composed of hydrogen which is ionized due to the plasma's high temperature. This element emits radiation in the X-ray band through free-free interactions, so it is possible to identify clusters by searching for diffuse X-ray emission in the sky. Furthermore, we can retrieve the cluster mass using X-ray data and the hydrostatic equilibrium assumption.

The condition of hydrostatic equilibrium, that is the balance between the gas pressure force and the gravitational one, can be expressed as:

$$\frac{dP_{gas}}{dr} = -\rho_{gas}\frac{GM(<r)}{r^2}, \tag{3.3}$$

where P_{gas} and ρ_{gas} are the gas pressure and density respectively, G is the Newtonian gravitational constant, while r is the distance from the cluster center and $M(<r)$ is the total mass contained within r. Because of the ICM high temperature and low density, we can assume that the plasma follows the equation of state for ideal gases. So, we can link P_{gas} with the temperature and density of the medium and retrieve the total cluster mass within a radius r:

$$M(<r) = -\frac{r}{G}\frac{k_B T_{gas}}{\mu m_p}\left(\frac{d\ln\rho_{gas}}{d\ln r} + \frac{d\ln T_{gas}}{d\ln r}\right). \tag{3.4}$$

Usually, the mean molecular weight of primordial composition $\mu \sim 0.59$ is assumed. In order to derive the temperature profile $T_{gas}(r)$, X-ray observations at different distances from the centre of the cluster are performed: the exponential cut-off of the bremsstrahlung spectrum provides the temperature value, assuming the density profile follows the β-model (Eq.(3.1)). However, this method poses an issue: the estimated mass is usually lower than the mass retrieved with other proxies. The reason is that in Eq.(3.4) the contributions to the pressure from turbulence, magnetic fields and interactions with cosmic rays are not included.

3.2.2 Sunyaev Zel'dovich Effect

The CMB photons passing through the ICM experience a shift in frequency due to the Inverse Compton (IC) interaction with hot free electrons inside the plasma. Specifically, the CMB low-frequency photons (radio band) gain energy from the electrons. The net result of this

interaction is the distortion of the CMB black-body spectrum. This modification consists of a lower number of photons with $\nu < \nu_0$ and, accordingly, a higher number of photons with $\nu > \nu_0$ ($\nu_0 \sim 217$ GHz is the characteristic frequency where the spectrum is not distorted). This effect is called *Thermal Sunyaev Zel'dovich Effect* (tSZ; see Sunyaev and Zel'dovich [1972]).

The tSZ effect is merely a spectrum distortion and does not depend on the cluster's redshift. In the low frequency approximation, it is possible to link the tSZ effect to a change in the signal intensity I equal to:

$$\frac{dI}{I} = \frac{dT}{T} = -2\frac{\sigma_T}{m_e c^2}\int P_e dl, \tag{3.5}$$

where σ_T is the Thompson scattering cross-section, c is the speed of light, while m_e and P_e are, respectively, the mass and pressure of the ICM free electrons. The typical variation in signal intensity is $dI/I \sim 10^{-4}$, and it is not negligible compared to the CMB anisotropies, that are an order of magnitude smaller. As said, the tSZ effect does not depend on the cluster's redshift and does not undergo surface brightness dimming. So tSZ observations are well-suited to search for massive clusters at high redshifts. This type of measurements are currently performed by the Planck satellite [see Erler et al., 2018].

Furthermore, the tSZ effect provides a reliable estimate of the electron thermal pressure. Hence by combining these radio measurements with X-ray observations, from which we retrieve the temperature, it is possible to evaluate the cluster mass.

3.2.3 Optical

Galaxy clusters are identified in the Optical band by searching for overdensities of galaxies in a small sky region. The main problems of this approach are to discriminate real clusters from random objects aligning along the line-of-sight and to distinguish the galaxy members of a cluster from field objects. Despite these disadvantages, the Optical band identification is the most used because with this method it is possible to construct large samples of clusters useful for cosmological investigations. Various methods have been implemented to find clusters and their members in the photometric data provided by the optical surveys. The most used is the *friend-of-friend algorithm*, which, assuming the cosmological parameters, searches for overdensities of galaxies with defined linking length and photometric redshift range. The linking length is the transverse distance: the separation between two objects on the sky plane. Another famous employed method is the *redMaPPer* cluster finding algorithm, which is a cluster finder specifically designed to make optimal use of ongoing and near-future large photometric surveys [see Rykoff et al., 2014]. The *redMaPPer* algorithm makes use of all the bands utilized in the survey (typically Optical and Near Infrared bands) to self-calibrate a model for the *red sequence* galaxies. The obtained model is then used to detect clusters as red galaxy overdensities, while simultaneously estimating the probability that each red galaxy is a cluster member. Lastly, we cite the detection algorithm called AMICO, *Adaptive Matched Identifier of Clustered Objects*,

described in Bellagamba et al. [2017]. This algorithm is aimed at identifying galaxy clusters given a photometric dataset of galaxies. In particular, it assumes a model for the density and luminosity profiles of galaxy clusters, and identify them by finding galaxy overdensities and matching them with the defined model. Moreover, in this case each galaxy has an assigned probability to be a member of a cluster or to be part of the field.

Finally, once clusters are identified, it is possible to estimate their masses using different approaches: applying the *Virial Theorem* or using scaling relations between cluster richness and mass.

The former method works under the assumptions that the cluster is in dynamical equilibrium. Moreover, spectroscopic observations are needed to retrieve the galaxy velocity dispersions along the line-of-sight. Indeed, it is possible to demonstrate (see Binney et al. [1987] for details) that the virial mass of the cluster is given by the relation:

$$M_V = \frac{\pi}{2}\frac{3\sigma_v^2 R_v}{G}, \tag{3.6}$$

where $\pi/2$ accounts for the system's geometry, R_V is the virialization radius projected along the line-of-sight and σ_v^2 is the projected velocity dispersion, while the factor 3 comes from the assumption of spherical symmetry. This method is rarely used in large surveys because of the long observational time needed to obtain galaxy spectra.

On the other hand, scaling relations are more utilized in large surveys. These relations are based on global optical properties of clusters such as their total luminosity or the number of member galaxies (*richness*). The relation between these observables and the cluster mass is calibrated using the proxies described above, such as the X-ray. The problem with this approach is that the calibration depends on the cluster finding algorithm, so it has to be repeated for every different cluster catalog. The cluster masses of the catalogs exploited in this Thesis work, which are described in Sec.5.1, have been retrieved using a specifically calibrated *richness-mass* relation.

3.2.4 Gravitational Lensing

Previously, we describe detection methods which suit only for specific bands: optical, radio and X-ray, while the following one can be applied on observations done in any wavelength. According to Einstein's General Relativity, the high mass of a galaxy cluster causes a distortion of the space-time geometry in the structure's surroundings. Light rays passing near the cluster follow a distorted path, instead of a linear path, because they track the geodetic lines given by the warped space-time geometry. Therefore, photons bend around the cluster in a phenomenon known as *Gravitational Lensing*. This event can both magnify and distort the images and create various copies of cluster background sources. The characteristics of gravitational lensing depend only on the lens mass distributions and the total mass of the system, while they do not rely on the cluster physical state. Thus, it is possible to find clusters by searching for galaxy overdensities around distorted or multiple galaxy images. Additionally, we can infer

the cluster's mass by assuming a model for the surface density distribution and then fitting the lensing observables. These observables are either the number of multiple images of a background source or the shear, which is the direction where the background galaxies are distorted. The gravitational lensing mass estimation provides the total mass of the cluster (i.e. the mass of the dark matter component); this estimation is better than the ones described previously because it does not rely on any assumption on ICM physics or cluster dynamical state.

3.3 Clusters as Cosmological Probes

Galaxy clusters are the largest and most massive gravitational bound structures in the Universe, so that the highest density peaks in the large-scale structures of the Universe are traced by them. Indeed, clusters of galaxies have been used in cosmological studies since Zwicky's discovery of DM inside the Coma cluster [see Zwicky, 1933]. By applying the virial theorem, he found that the virial cluster mass exceeds the total mass of all member galaxies by a factor of about 400. Thus, it was necessary to postulate the existence of an invisible matter component, the dark matter, or to modify the gravity theory.

According to the classical model of cosmic structures formation, the so-called *hierarchical model*, the largest objects in the Universe have been built through a sequence of mergers and accretion phenomena. The description of the formation of these objects is quite simple compared to that of the galaxies, because we can neglect the gas dynamical effects. Therefore, galaxy clusters mark the transition between the linear regime and the non linear one. In addition, the dark matter component dominates the gravitational field, so the cluster formation and evolution can be determined simply by assuming the initial conditions of the dark matter perturbations in the primordial Universe. Then, the possibility of modelling the statistical properties of clusters of galaxies as a function of cosmological parameters, combined with the capability of measuring their basic properties, such as the mass, as discussed previously, makes them optimal tracers of the large-scale structure of the Universe and powerful cosmological probes to infer the cosmological model parameters.

Notably, the galaxy cluster mass function strongly depends on cosmological parameters, particularly the matter density parameter (Ω_M) as a result of the linear growth rate of perturbations. This allows the assessment of the evolutionary models of the Universe by studying the number and mass distributions of clusters of galaxies at different redshifts [see Lesci et al., 2020]. Another strategy to extract cosmological information is to make use of the two-point and three-point correlation functions, which describe how clusters are clustered inside the large cosmic structure (see Marulli et al. [2018] and Marulli et al. [2021]). These studies are even more efficient if combined with other observables such as the anisotropies in CMB radiation [see Salvati et al., 2018]. Finally, galaxy clusters are good tracers of redshift space distortions (see Marulli et al. [2012], Marulli et al [2017] and Veropalumbo et al. [2014, 2016]).

Chapter 4

Gravitational Redshift in Galaxy Clusters

All gravity theories predict that photon frequencies are redshifted due to a gravitational field. When a photon with wavelength λ is emitted inside a gravitational potential ϕ, it loses energy when it climbs up in the gravitational potential well, and is consequently redshifted. The gravitational redshift, z_g, observed at infinity in the weak field limit, can be expressed as follows:

$$z_g := \frac{\Delta\lambda}{\lambda} \simeq \frac{\Delta\phi}{c^2}, \tag{4.1}$$

where $\Delta\lambda$ and $\Delta\phi$ are the difference in wavelength and the difference in potential, respectively, between where the photon is emitted and where it is observed.

Let us consider a galaxy, which resides inside a cluster, as a source of photons. The measurement of the total observed galaxy redshift, z_{obs}, is the sum of three components: the cosmological redshift, z_{cosm}, the Doppler redshift from the line-of-sight peculiar velocity, z_{pec}, and the gravitational redshift:

$$\ln(1 + z_{obs}) = \ln(1 + z_{cosm}) + \ln(1 + z_{pec}) + \ln(1 + z_g). \tag{4.2}$$

The cosmological redshift, $z_{cosm} \simeq \frac{H(z)r}{c}$, due to the expansion of the Universe, is the same for both the galaxy and the host galaxy cluster. The peculiar redshift, a Doppler redshift, is caused by the random motions of the galaxy within the cluster. The galaxy is in motion around the minimum of the cluster potential well, its dynamical centre. The gravitational redshift depends on the cluster gravitational potential and, as a consequence, it depends on the mass distribution around the galaxy. Thus, for a typical cluster mass of $10^{14}\ M_\odot$, the gravitational redshift is estimated to be $cz_g \simeq 10$ km s^{-1} (see Cappi [1995]), which is around two orders of magnitudes smaller than the peculiar redshift. The small effect of the gravitational redshift becomes detectable when the number of analyzed galaxies is large, $N_{gal} \gtrsim 10^4$ [see Zhao, 2013]. Because of this, stacked data of a large sample of clusters and galaxies are necessary to measure the gravitational redshift effect in galaxy clusters. The method of disentangling the gravitational redshift from the other components relies on measuring the distribution of

line-of-sight velocity offsets derived from observed redshifts. The line-of-sight velocity offset is defined as follows:

$$\Delta := c[\ln(1 + z_{obs}) - \ln(1 + z_{cen})], \tag{4.3}$$

where z_{cen} is the redshift of the cluster centre. Generally the BCG is taken as the cluster centre, because BCG belongs to the so-called *cold population* of the cluster, and thus his peculiar velocity is relatively small compared to the other galaxies within the cluster. Moreover, Cui et al. [2015] have found that the BCG correlates well with the minimum of the gravitational potential. We note that Δ does not depend on the cosmological redshift component, which is the same in the two terms, and thus cancels. In this Thesis work, differences in the logarithm of the redshifts have been used instead of simply assuming $z = v/c$, because the natural logarithm provides a better approximation of the line-of-sight velocity [see Baldry, 2018]. The distribution of Δ over all galaxy cluster members is a quasi-Gaussian distribution with nonzero mean velocity. The shift of the centre of this distribution is due to the gravitational redshift caused by the spatial variation of the gravitational potential:

$$\Delta = \frac{\phi(0) - \phi(r)}{c}, \tag{4.4}$$

where r is the distance from the cluster centre. This effect is present in any reliable theory of gravity. Thus, the shift of the average is the quantity of interest in this study; the size of the shift and its evolution with distance from the cluster centre are both informative on the theory of gravity governing the observed redshifts of these galaxies.

In the following Sections we describe how it is possible to model the gravitational redshift effect for a sample of clusters with different masses. We present this model in three different gravity theories: the General Relativity, the $f(R)$ theory and the Dvali-Gabadadze-Porrati (DGP) models. Finally, in the last Section of this chapter we show the results of the past literature works.

4.1 General Relativity

The distribution of line-of-sight velocity offsets between galaxies and their host cluster's centre, Δ, defined in Eq.(4.3), is expected to have an average value that is blueshifted (see Cappi [1995] and Kim and Croft [2004]). In fact, photons experience the largest gravitational redshifting at the minimum of the cluster potential wells and the gravitational redshift effect decreases moving towards the cluster outskirt, as the potential well decreases too. Therefore, comparing the redshift of the centre with redshifts of galaxies gives the net results of a blueshift. For a single galaxy, the gravitational redshift, expressed as a velocity offset, is given by Eq.(4.4), where the gravitational potential can be retrieved by assuming the cluster matter density distribution. Generally we can only measure the line-of-sight information with sufficient accuracy, therefore only the projected distance from the centre of the cluster, R, is known. Thus, to compute

the gravitational redshift effect, the density along the line-of-sight to that distance has to be integrated along with the potential difference.

During this Thesis work we assume that the cluster density profile follows the NFW radial profile [Navarro et al., 1995]. Moreover, we use the projected distance from the centre of the cluster in units of r_{500}, because scaling the separation between galaxies and the associated cluster centre takes advantage of the self-similarity of clusters. Moreover, stacking data by simply using distances in Megaparsecs is not ideal, as clusters can have a large range of sizes, and therefore different masses and densities at the same distance from the centre. In this Thesis, r_{500} is the radius where the cluster density is 500 times the critical density of the Universe, ρ_{cr}. Therefore, it is possible to define the cluster mass M_{500}, at radius r_{500}, as follows:

$$M_{500} = \frac{4}{3}\pi r_{500}^3 500 \rho_{cr}. \tag{4.5}$$

Hence, the NFW density profile of a cluster, in units of its radius r_{500}, can be expressed as follows (see Łokas and Mamon [2001]):

$$\rho(\tilde{r}) = \frac{M_{500} c_{500}^2 g(c_{500})}{4\pi r_{500}^3 \tilde{r}(1 + c_{500}\tilde{r})^2}, \tag{4.6}$$

where $\tilde{r} = r/r_{500}$ and c_{500} is the cluster concentration parameter defined as $c_{500} = r_{500}/r_s$, r_s is the so-called *scale radius* of the cluster. Moreover, the function $g(c_{500})$ can be expressed as follows:

$$g(c_{500}) = \left(\ln(1 + c_{500}) - \frac{c_{500}}{1 + c_{500}}\right)^{-1}. \tag{4.7}$$

The gravitational potential, associated with the density distribution given by Eq.(4.6), results:

$$\phi(\tilde{r}) = -g(c_{500}) \frac{G M_{500}}{r_{500}} \frac{\ln(1 + c_{500}\tilde{r})}{\tilde{r}} \tag{4.8}$$

Hence, under these assumptions, the gravitational redshift for a single cluster can be written as follows (see Łokas and Mamon [2001]):

$$\Delta_{c,gz}(\tilde{R}) = \frac{2 r_{500}}{c \Sigma(\tilde{R})} \int_{\tilde{R}}^{\infty} (\phi(0) - \phi(\tilde{r})) \frac{\rho(\tilde{r}) \tilde{r} \mathrm{d}\tilde{r}}{\sqrt{\tilde{r}^2 - \tilde{R}^2}}, \tag{4.9}$$

where $\tilde{R}$ is the projected distance from the centre of the cluster in units of r_{500}. $\Sigma(\tilde{R})$ is the surface mass density profile found from the integration of the NFW density profile along the line-of-sight:

$$\Sigma(\tilde{R}) = 2 r_{500} \int_{\tilde{R}}^{\infty} \frac{\rho(\tilde{r}) \tilde{r}}{\sqrt{\tilde{r}^2 - \tilde{R}^2}} \mathrm{d}\tilde{r}. \tag{4.10}$$

Here we assume that the clusters have spherical symmetry because a stacked sample of many clusters is expected to exhibit spherical symmetry, even though often it is not the case for a single cluster [Kim and Croft, 2004]. Following Wojtak et al. [2011] the gravitational redshift signal for a stacked cluster sample can be calculated by convolving the gravitational redshift profile for a single cluster with the cluster mass distribution, this operation can be expressed as follows:

$$\Delta_{gz}(\tilde{R}) = \frac{\int_{M_{min}}^{M_{max}} \Delta_{c,gz}(\tilde{R})\Sigma(\tilde{R})(\mathrm{d}N/\mathrm{d}M_{500})\mathrm{d}M_{500}}{\int_{M_{min}}^{M_{max}} \Sigma(\tilde{R})(\mathrm{d}N/\mathrm{d}M_{500})\mathrm{d}M_{500}}. \tag{4.11}$$

By calculating the integral in Eq.(4.11) it is possible to compute the gravitational redshift effect for a stacked cluster sample as a function of the projected radius. However, Zhao [2013] and Kaiser [2013] demonstrated that the shift of the mean in the Δ distribution is affected by various corrections, which are of the same order of the gravitational redshift, these corrections will be described in Sec.4.4.

The Eq.(4.11) is valid in any theory of gravity, but different gravity theories predict a different gravitational acceleration experienced by photons within the cluster. Thus, in the following Sections we describe the gravitational acceleration as a function of the cluster radius, $g(r)$, predicted by two different gravity theories: the $f(R)$ gravity (see Sotiriou and Faraoni [2010] for a complete review) and the Dvali–Gabadadze–Porrati (DGP) models [Dvali et al., 2000]. These two theories are consistent models which appreciably modify gravity on the largest scales, to reproduce the Universe accelerated expansion, but restore General Relativity locally. Moreover, both theories can be adjusted to satisfy all current constraints on gravity.

4.2 $f(R)$ Gravity

In the ΛCDM model, the Einstein-Hilbert action, S, integrated over all coordinates of spacetime, describes the interaction between matter and gravity and can be expressed as follows:

$$S = \int d^4x\sqrt{-g}\left[\frac{M_{pl}^2}{2}(R - 2\Lambda) + L_m\right], \tag{4.12}$$

where $M_{pl} = \sqrt{1/8\pi G}$ is the reduced Planck mass; R is the Ricci scalar, which gives information on the curvature of the space-time; L_m is the matter Lagrangian and g is the FLRW metric determinant. Starobinsky [1980] demonstrates that it is possible to modify Eq.(4.12) to represent a modified gravity theory as follows:

$$S = \int d^4x\sqrt{-g}\left[\frac{M_{pl}^2}{2}(R - f(R)) + L_m\right], \tag{4.13}$$

where the cosmological constant is replaced with a function of the Ricci scalar, $f(R)$, which is an unknown function. $f(R)$ models are scalar-tensor theories, where the scalar degree of

freedom is given by $f_R \equiv df/dR$ which mediates the relation between density and space-time curvature. The theory is stable under perturbations if $f_R < 0$. This theory is created to reproduce the proprieties of the ΛCDM model on the linear scales. Thus, following Schmidt [2010], in the quasi-static regime, the f_R field and the modified dynamical potential, Ψ, are determined from the density field by the following equations:

$$\nabla^2 \delta f_R = \frac{1}{3}\left[\delta R(f_R) - 8\pi G \delta\rho\right], \tag{4.14}$$

$$\nabla^2 \Psi = \frac{16\pi G}{3}\delta\rho - \frac{1}{6}\delta R(f_R), \tag{4.15}$$

where $\delta f_R \equiv f_R - \bar{f_R}$, $\delta R \equiv R - \bar{R}$ and $\delta\rho \equiv R\rho - \bar{\rho}$ are perturbations from the background value. R and δR are non linear functions of the field f_R. The following calculations are made considering $z = 0$, this assumption does not affect the results of this work, because the final analyzed samples have a medium redshfit of about 0.2, as described in Sec.5.3.

Let us consider the case where f_R is much larger than typical potential wells in the universe, then it is possible to linearize the δR term. The result is:

$$\Psi = \frac{4}{3}\Psi_N, \tag{4.16}$$

where Ψ_N is the Newtonian potential. Hence, the gravitational force is increased by $4/3$ within the range of the f_R field given by the Compton wavelength, λ_c, which is expressed as follows:

$$\lambda_c^2 = 3\frac{d^2 f}{dR^2}. \tag{4.17}$$

In the opposite limit, we retrieve that:

$$\delta R(f_R) \simeq 8\pi G \delta\rho, \tag{4.18}$$

therefore $\Psi = \Psi_N$, and the General Relativity is restored. This is the so-called *chameleon regime* [Khoury and Weltman, 2004].

Let us consider the solution for a spherically symmetric mass, to determine the transition between the two regimes described previously. In this case, it is possible to express the solution for δf_R as follows:

$$\delta f_R(r) = \frac{2G\delta M_{eff}(<r)}{3r}, \tag{4.19}$$

$$\delta M_{eff}(<r) = 4\pi \int_0^r \mathrm{d}r' r'^2 \delta\rho_{eff}(r'), \tag{4.20}$$

$$\delta\rho_{eff}(r) = \delta\rho(r) - \frac{\delta R(r)}{8\pi G}. \tag{4.21}$$

Considering these equations, the result is that the dynamical potential satisfies:

$$\nabla^2\Psi = 4\pi G\left(\delta\rho + \frac{1}{3}\delta\rho_{eff}\right). \tag{4.22}$$

Thus, if the perturbation δf_R is small for all r (in general this is true far away from the body), we can neglect the δR term in Eq.(4.21), then $\delta M = \delta M_{eff}$. Hence, from Eq.(4.19) we obtain:

$$|f_{R0}| \leq \frac{2}{3}\Psi_N, \tag{4.23}$$

where $f_{R0} = f(\bar{R}_0)$ and $\bar{R}_0$ is the present-day background curvature. To retrieve this condition we have considered that δf_R can achieve the maximum value of $|\bar{f}_R|$, in which case the f_R field becomes equal to zero. Eq.(4.23) states that if the value of Ψ_N for the body is larger than this, the field must enter the chameleon regime. Thus, ρ_{eff} is nonzero only outside of the radius where Eq.(4.23) is valid, then δM_{eff} is the mass outside of this radius. The cosmological potentials range from 10^{-6} to 10^{-5} (see Nadathur et al. [2017]), therefore the chameleon mechanism is expected to operate for background field values lower than 10^{-5}. These arguments are valid for any form of the function $f(R)$. Hence, to evaluate the effects on the dynamics within galaxy clusters, Schmidt [2010] chooses the following functional form:

$$f(R) = -2\Lambda - f_{R0}\frac{\bar{R}_0{}^2}{R}. \tag{4.24}$$

The first term supplies an effective cosmological constant, yielding accelerated expansion of the background. The second term determines the departures from GR and yields corrections to the background expansion with order of magnitude f_{R0}. The analyzed models have $|f_{R0}| \leq 10^{-4}$, hence the background expansion is indistinguishable from the one predicted by the ΛCDM model. To make a comparison between GR and various alternative gravity models, the parameter g is defined as follows:

$$g(r) := \frac{d\Psi/dr}{d\Psi_N/dr}. \tag{4.25}$$

This parameter quantifies the strength of the gravitational force in modified gravity relative to that which would be measured in GR, given the same density field ($g = 1$ corresponds to unmodified forces). Assuming spherical symmetry and the NFW density profile, it is possible to calculate $g_{f(R)}(r)$, which quantifies the differences between GR and $f(R)$ theory within a galaxy cluster. Hence, combining Eqs.(4.19-4.22,4.24), we obtain:

$$g_{f(R)}(r) = 1 + \frac{1}{3}\frac{M_{eff}(<r)}{M(<r)}. \tag{4.26}$$

Schmidt [2010] performed simulations to compute $g_{f(R)}(r)$ for a range of background field values: $|f_{R0}| = 10^{-6}, 10^{-5}, 10^{-4}$. Figure 4.1 shows the simulation results and the theoretical

predictions for the parameter $g_{f(R)}(r)$ as a function of the halo mass. The models, with $|f_{R0}| = 10^{-6}, 10^{-5}$ show a dependence of the parameter $g_{f(R)}(r)$ from the halo mass, while the model with $|f_{R0}| = 10^{-4}$ is almost constant.

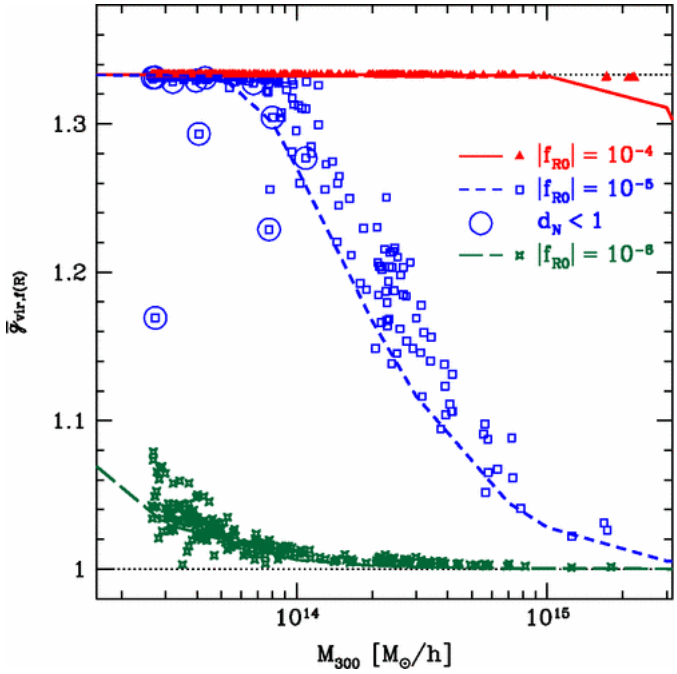

Figure 4.1: Simulation results and theoretical predictions for the parameter $g_{f(R)}(r)$ as a function of the halo mass for three values of $|f_{R0}|$ (circled points are halos that have a more massive halo in their immediate vicinity). Credits to: Schmidt [2010].

In this Thesis work we consider the strong field model with $|f_{R0}| = 10^{-4}$, where the chameleon mechanism is essentially absent. In fact, this model predicts a $4/3$ enhancement of the gravitational force for all halo masses ($G_{f(R)} = 4/3G$). Thus, this is the condition we assume in this study, for a simple comparison between the prediction of $\hat{\Delta}$ in General Relativity and in $f(R)$ gravity. We emphasise that this simple model is useful to provide some insight into the sensitivity of $\hat{\Delta}$ to variations of the theory of gravity.

4.3 Dvali–Gabadadze–Porrati Model

In the DGP braneworld scenario [Dvali et al., 2000], matter and radiation live on a four-dimensional brane embedded in a five-dimensional Minkowski space. The action is constructed so that on scales larger than the so-called *crossover scale*, r_c, the gravity is five-dimensional, while it becomes four-dimensional on scales smaller than r_c. Thus, the gravitational potential goes as $1/r$ at short distances for the sources localized on a brane. As a result, an observer on

a brane will see correct Newtonian gravity despite of the fact that gravity propagates in extra space, which is flat and has an infinite size. This model admits a homogeneous cosmological solution on the brane, which obeys to a modified Friedmann equation (see Deffayet [2001]):

$$H^2 \pm \frac{H}{r_c} = 8\pi G[\bar{\rho} + \rho_{DE}], \tag{4.27}$$

where ρ_{DE} is the density associated with the cosmological constant. The sign on the left side of Eq.(4.27) is determined by the choice of the embedding of the brane. The negative sign is the so-called *self-accelerating* branch, which allows for accelerated Universe expansion even in the absence of a cosmological constant. The positive sign is the so-called *normal* branch, which does not exhibit self-acceleration.

On scales smaller than the r_c, the DGP models can be described as a scalar-tensor theory where the brane-bending mode φ mediates an additional attractive (normal branch) or repulsive (self-accelerating branch) force [Nicolis and Rattazzi, 2004]. In DGP models the gravitational forces are governed by the equation:

$$\nabla\Psi = \nabla\Psi_N + \frac{1}{2}\nabla\varphi, \tag{4.28}$$

where the φ field is created by matter overdensities. However, the φ field has quadratic self-interactions that suppress its effect once the density contrasts become nonlinear. The equation which describes the φ field is:

$$\nabla^2\varphi + \frac{r_c^2}{3\beta}[(\nabla^2\varphi)^2 - (\nabla_i\nabla_j\varphi)(\nabla^i\nabla^j\varphi)] = \frac{8\pi G}{3\beta}\delta\rho, \tag{4.29}$$

where β is a function of the expansion rate $H(a)$. It is possible to find an analytical solution for Eq.(4.29) in the case of spherically symmetric mass. In particular, we obtain an equation for the φ gradient:

$$\frac{d\varphi}{dr} = \frac{G\delta M(<r)}{r^2}\frac{4}{3\beta}g\left(\frac{r}{r_*(r)}\right), \tag{4.30}$$

where the function $g\left(\frac{r}{r_*(r)}\right)$ can be expressed as follows:

$$g\left(\frac{r}{r_*(r)}\right) = \left(\frac{r}{r_*(r)}\right)^3\left[\sqrt{1+\left(\frac{r}{r_*(r)}\right)^{-3}} - 1\right], \tag{4.31}$$

$r_*(r)$ is the so-called *r-dependent Vainshtein radius*. The function r/r_* depends on the average overdensity $\delta\rho(<r)$, within r. It is possible to re-scale this function to a halo with mass M_Δ and radius R_Δ, determined by a fixed overdensity Δ. Thus, we obtain:

$$\frac{r}{r_*(r)} = (\varepsilon\Delta)^{-1/3}x\left(\frac{M(<x)}{M_\Delta}\right)^{-1/3}, \tag{4.32}$$

where $x = r/R_\Delta$ and the quantity ε is determined by the background cosmology. Hence, by using Eq.(4.28,4.30), it is possible to calculate the parameter $g_{DGP}(r)$, which quantifies the differences between GR and DGP models, therefore the result is:

$$g_{DGP}(r) = 1 + \frac{2}{3\beta} g\left(\frac{r}{r_*(r)}\right). \tag{4.33}$$

On the largest scales, $\delta\rho(< r) \ll \bar{\rho}$ and $r_* \ll r$, then $g\left(\frac{r}{r_*(r)}\right) \to 1/2$ and $d\varphi/dr$ becomes proportional to $d\Psi_N/dr$. In this case, we obtain that $g_{DGP} = g_{DGP,lin} = 1 + 1/(3\beta)$. On the other hand, on the smallest scales where $r \ll r_*$, the modified forces are suppressed.

Schmidt [2010] performed simulations for spherical clusters with a NFW profile, using three different DGP models: two normal branch models (nDGP-1, nDGP-2) and one self-accelerating branch model (sDGP). Figure 4.2 shows the results of these simulations for the parameter g_{DGP} as a function of the halo mass (left panel) and the halo radius (right panel). The left panel shows that g_{DGP} is almost constant with the halo mass for the three models. However, the two normal branch models have an enhancement of the gravitational force, while the self-accelerating branch model presents a reduction of the force, for all the masses. The right panel shows that the variation of the gravitational force, with respect to the General Relativity prediction, changes with the cluster radius for all the analyzed models.

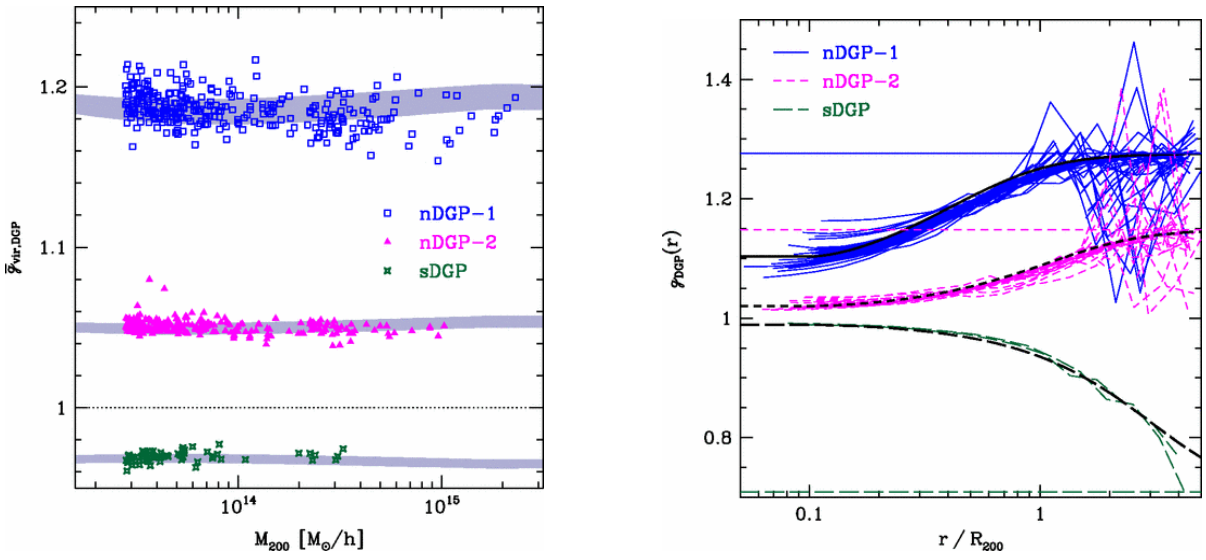

Figure 4.2: The left panel shows the simulations results for the parameter g_{DGP} as a function of the halo mass (colored points); the grey lines are the theoretical predictions. The right panel shows the results for the same parameter as a function of the halo radius (colored thin lines); the thick black lines are the theoretical predictions, while the horizontal lines show $g_{DGP,lin}$. Credits to: Schmidt [2010].

In this Thesis work, we consider a self-accelerating model, the sDPG model, where $\rho_{DE} = 0$. In this model the value of $r_c \simeq 6000$ Mpc is adjusted to best match the constrains derived from CMB observations and Universe expansion history [Fang et al., 2008]. Schmidt [2010] showed that for the sDGP model $\beta = -1.15$ and $\varepsilon = 0.32$ at $z = 0$.

4.4 Other Effects

In this Section we describe the other effects which affect the distribution of the velocity offsets. The following description is valid in any reliable theory of gravity.

4.4.1 Transverse Doppler Effect

The peculiar redshift of a galaxy can be decomposed as follows:

$$1 + z_{pec} \simeq 1 + \frac{v_{los}}{c} + \frac{1}{2}\frac{v^2}{c^2} + ..., \tag{4.34}$$

where v_{los} gives the velocity component along the line-of-sight. The second-order term, due to the transverse motion of the galaxy, gives rise to the transverse Doppler (TD) effect. The TD contributes with a small positive shift of the mean in the velocity distribution; this is typically a few km s^{-1}, and is relatively constant with distance from the cluster centre. The additional effect on the radial velocity shift of the mean can be expressed as follows:

$$\Delta_{TD} = \frac{\langle v_{gal}^2 - v_0^2 \rangle}{2c}, \tag{4.35}$$

where v_{gal} and v_0 are the peculiar velocities of the galaxy and the cluster centre, respectively. Calculating this effect involves an integral over the line-of-sight density profile and a convolution with the mass distribution [Zhao, 2013]. Therefore, the TD effect for a single cluster results:

$$\Delta_{c,TD}(\tilde{R}) = \frac{2Qr_{500}}{c\Sigma(\tilde{R})} \int_{\tilde{R}}^{\infty} (\tilde{r}^2 - \tilde{R}^2) \frac{\mathrm{d}\phi(\tilde{r})}{\mathrm{d}\tilde{r}} \frac{\rho(\tilde{r})\mathrm{d}\tilde{r}}{\sqrt{\tilde{r}^2 - \tilde{R}^2}}, \tag{4.36}$$

where $Q = 3/2$ for isotropic orbits. This equation must be convolved with the mass distribution to retrieve the effect for the stacked cluster sample, so we obtain:

$$\Delta_{TD}(\tilde{R}) = \frac{\int_{M_{min}}^{M_{max}} \Delta_{c,TD}(\tilde{R})\Sigma(\tilde{R})(\mathrm{d}N/\mathrm{d}M_{500})\mathrm{d}M_{500}}{\int_{M_{min}}^{M_{max}} \Sigma(\tilde{R})(\mathrm{d}N/\mathrm{d}M_{500})\mathrm{d}M_{500}}. \tag{4.37}$$

4.4.2 Light-cone Effect

When we observe galaxies we are observing objects which lie in our past light cone (LC). This causes a bias such that we see more galaxies moving away from us than moving towards us,

due to the time it takes light to travel trough the cluster. Hence, this effect causes an asymmetry in the Δ distribution, which results in a positive shift of the mean. The shift given by the LC effect results:

$$\Delta_{LC} = \frac{\langle v^2_{los,gal} - v^2_{los,0} \rangle}{c}, \tag{4.38}$$

where $v_{los,gal}$ and $v_{los,0}$ are the line-of-sight velocities of the galaxy and the cluster centre, respectively. The LC effect is of the same order of the TD effect and is opposite in sign to the effect of gravitational redshift. To compute the LC effect on a stacked sample of clusters it is necessary to repeat the operations already done for the TD effect. Hence, by assuming isotropic orbits of the galaxies, we obtain:

$$\Delta_{LC} = \frac{2}{3}\Delta_{TD}. \tag{4.39}$$

4.4.3 Surface Brightness Modulation Effect

Galaxies in spectroscopic or photometric samples are generally selected according to their apparent luminosity, l. The apparent luminosity of a galaxy depends on its peculiar motion through the special relativistic beaming effect, which changes the galaxy surface brightness and thus its luminosity. In particular, this effect enhances the luminosity of galaxies which are in motion towards the observer, while it decreases the luminosity of those moving away. Thus, the beaming effect could shift the galaxies moving towards the observer into the luminosity cut, while it could shift the galaxies moving away outside the luminosity cut. Generally, this creates a preferential bias in the selection of galaxies, promoting galaxies which are moving towards the observer, with the overall effect of a blueshift on the centre of the distribution of velocity offsets. Let us consider the effect on the BCGs. For these galaxies, the flux limit is irrelevant, due to their high intrinsic luminosity, but there is a bias because peculiar velocities can change the ranking of the two brightest galaxies. This can lead to a wrong selection of the BCG.

The size of the surface brightness modulation (SB) effect depends strongly on the galaxy survey. The size of the relativistic beaming effect can be calculated considering the fractional change in the apparent galaxy luminosity as a function of the spectral index, α, at the cosmological redshift of the source, as well as considering the peculiar velocity of the galaxy [Kaiser, 2013]. The fractional change can be expressed as follows:

$$\frac{\Delta l}{l} = (3 + \alpha(z))\frac{v_x}{c}. \tag{4.40}$$

Furthermore, the modulation of the number density of detectable objects at a given redshift

is given by:

$$\frac{\Delta l}{l}\delta(z) = -(3+\alpha(z))\frac{v_x}{c}\frac{\mathrm{d}\ln n(>l_{lim}(z))}{\mathrm{d}\ln l}, \tag{4.41}$$

where $\delta(z)$ is the redshift dependent logarithmic derivative of the number distribution of galaxies and l_{lim} is the apparent luminosity limit of the survey. The redshift dependence comes from translating the apparent luminosity limit to an absolute luminosity limit that varies with redshift. Following Kaiser [2013], it is possible to assume $\alpha(z) \simeq 2$ for the whole redshift range. Hence, assuming isotropy, we can obtain the predicted shift of the mean due to the SB effect:

$$\Delta_{SB} = -5\langle\delta(z)\rangle\frac{\langle v^2_{x,gal} - v^2_{x,0}\rangle}{c}, \tag{4.42}$$

where $\langle\delta(z)\rangle$ is the average value of δ over the redshift range of the cluster sample. Just as it was done for the LC effect, we can rewrite the SB effect as a function of the TD effect. The result can be expressed as follows:

$$\Delta_{SB} = -\frac{10}{3}\langle\delta(z)\rangle\Delta_{TD}. \tag{4.43}$$

Thus, we notice that the SB effect is of the same order of the TD and LC effects, but is opposite in sign. The SB effect leads to a blueshift of the centre of the distribution of velocity offsets, as mentioned previously.

4.4.4 The Combined Effect

The effects described in the previous Sections are not the only ones present, thought they are the dominant ones. Cai et al. [2017] provided a comprehensive summary of the different contributions to the mean of the velocity offset distribution, $\hat{\Delta}$, including the cross-terms. It is demonstrated that these cross-terms change the $\hat{\Delta}$ signal by a factor less than 1 km s^{-1}, so they will not be considered any further in this work. Hence, the combination of the effects considered in this analysis results:

$$\hat{\Delta} = \Delta_{gz} + \Delta_{TD} + \Delta_{LC} + \Delta_{SB}, \tag{4.44}$$

$$\hat{\Delta} = \Delta_{gz} + (2 - 5\langle\delta(z)\rangle)\frac{2}{3}\Delta_{TD}. \tag{4.45}$$

The factor $2/3$ in Eq.(4.45) arises from the fact that in this Thesis work we consider logarithmic differences in redshifts; this alters the size of the TD effect [Mpetha et al., 2021]. Hence, we need to calculate only the gravitational and the TD effects, as well as $\delta(z)$, to account for the four largest contributions in $\hat{\Delta}$. In Chapter 6 we will show how we compute these effects for the cluster catalogs exploited in this Thesis.

The TD, LC and SB effects are small compared to the gravitational one. Thus, from now on, we refer to the combined effect as the gravitational redshift effect.

4.5 Previous Results

In this Section we present past literature on the measure of the gravitational redshift in clusters of galaxies.

Wojtak et al. [2011] made the first attempt to detect the gravitational redshift effect in galaxy clusters, using spectroscopic data from the Sloan Digital Sky Survey Data Release 7 (see Abazajian et al. [2009]) and the associated Gaussian Mixture Brightest Cluster Galaxy (GMBCG) catalog [Hao et al., 2010]. This cluster sample is richness-limited with a threshold corresponding to a cluster mass of 10^{14} $M_{\odot}$. In this analysis, the galaxy redshifts were selected using a cut of 6 Mpc in transverse distance from the cluster BCG and a cut of ± 4000 km s^{-1} around the cluster centre. Figure 4.3 shows the evaluated $\hat{\Delta}$ in four bins of projected distance from the cluster centre. The data are compared with the predictions of General Relativity, $f(R)$ theory and TeVeS, a relativistic generalization of the Modified Newtonian Dynamics theory [Bekenstein, 2004] (the effects which affect $\hat{\Delta}$ described in Sec.4.4 were not taken into account). Wojtak et al. [2011] found that the integrated signal of the gravitational redshift within 6 Mpc results $\hat{\Delta} = -7.7 \pm 3$ km s^{-1}. The author claimed that his measurements are in agreement with General Relativity and the $f(R)$ theory, while the data seems to marginally discard TeVes theory.

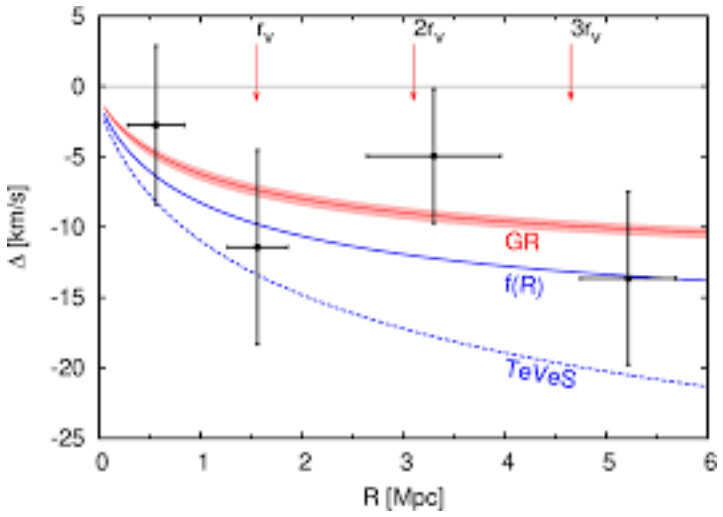

Figure 4.3: The black points are the evaluated $\hat{\Delta}$ from data, the error bars represent the range of $\hat{\Delta}$ containing 68% of the marginal probability and the dispersion of the projected radii in a given bin. The red line is the General relativity prediction, the blue line is the prediction of the $f(R)$ theory and the blue dotted line is the TeVeS prediction. Credits to: Wojtak et al. [2011].

Jimeno et al. [2014] made an attempt to detect the gravitational redshift effect in galaxy clusters using spectroscopic data from the Sloan Digital Sky Survey (SDSS) Data Release 12 (see Dawson et al. [2012]) and three different cluster catalogs: WHL12 described in Wen et al. [2012], the GMBCG [Hao et al., 2010] and the RedMaPPer cluster catalog [Rykoff et al., 2014]. In this analysis, the galaxy redshifts were selected using a cut of 7 Mpc in transverse distance from the cluster BCG and a cut of ± 6000 km s^{-1} around the cluster centre. For the three cluster catalogs, $\hat{\Delta}$ was evaluated from data in bins of mass and radius. The General Relativity predictions were computed as a function of cluster mass and radius, following the prescriptions given by Kaiser [2013]. Figure 4.4 shows the results of the analysis as a function of the cluster radius (left panel) and the cluster mass (right panel). The data from the GMBCG and RedMaPPer catalogs show an accordance with the model, while WHL12 data show a positive value of $\hat{\Delta}$. The authors claimed that WHL12 data are dominated by the less massive and reliable clusters.

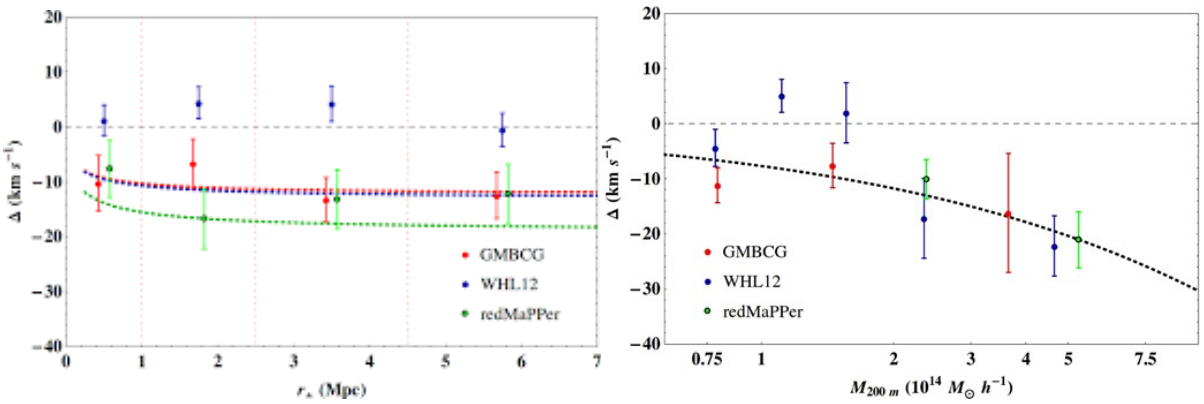

(a) (b)

Figure 4.4: Evaluated $\hat{\Delta}$ from data (colored points) and General relativity predictions (dotted lines) for the three cluster catalogs. The left panel shows the measurement as function of the cluster radius, while the right panel shows the results as a function of the cluster mass. Credits to: Jimeno et al. [2014].

The last attempt to measure the gravitational redshift in galaxy clusters was carried out by Mpetha et al. [2021]. The authors analyzed data from the SPectroscopic IDentification of ERosita Sources (SPIDERS, see Clerc et al. [2020]). The authors study the gravitational redshift effect in about 2500 clusters using three different definitions of the cluster centre: the BCG, the redMaPPer identified Central Galaxy (CG) and the peak of X-ray emission. The effect has been studied up to a distance of $1.2\ R_{200}$ from the cluster centre, Fig.4.5 shows the results of this analysis. The authors calculated the General Relativity and $f(R)$ predictions as a function of cluster radius. The results show that there is no significant preference of one gravity theory over another, but the authors claimed that in all the cases there is a clear detection of the

gravitational redshift. Mpetha et al. [2021] deemed that the BCG centroid is the most robust method in their analysis, due to the well defined central redshift.

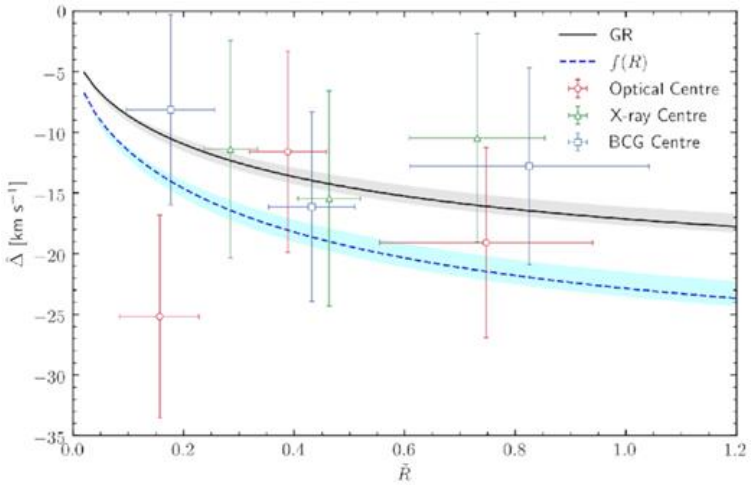

Figure 4.5: Evaluated $\hat{\Delta}$ from data (colored points) for the three considered cluster centres. General relativity (black line) and $f(R)$ (blue dotted line) predictions as a function of cluster radius. Credits to: Mpetha et al. [2021].

Chapter 5

New Catalogs of Cluster Member Galaxies

The goal of this Thesis work is to measure the gravitational redshift inside clusters of galaxies and to impose new and robust constraints on the theory of gravity. To do this, we need to cross-match a cluster sample with a large spectroscopic catalog of galaxies, in order to find the cluster member galaxies and to calculate the distribution of the galaxy line-of-sight velocity offsets described in Chapter 4. Thus, starting from public data of clusters and galaxies, we create new catalogs of cluster member galaxies, that were never exploited in past literature. In this Chapter we describe the main features of the public data and the new catalogs exploited in this Thesis.

5.1 Cluster Catalogs

5.1.1 The Wen-Han-Liu Catalog

In this Thesis work we exploit the *Wen-Han-Liu* catalog described in Wen et al. [2015] (WHL15), which is an updated version of the catalog described in Wen et al. [2012] (WHL12). The WHL12 sample was built using the SDSS-III photometric data. The method used to identify the clusters is based on a *friend-of-friend algorithm*. In practice, a cluster is identified if more than eight member galaxies, with an *r-band* absolute magnitude, M_r, smaller than -21, are found within a radius of 0.5 Mpc and within a photometric redshift range of $0.04(1+z)$. To calculate the comoving distances the authors assumed the ΛCDM cosmological model with $H_0 = 72$ km s^{-1}, $\Omega_m = 0.3$ and $\Omega_\Lambda = 0.7$. After that, the BCG is recognized among the cluster members and it is taken as the cluster center. The authors calculated the total luminosity within a radius of 1 Mpc, $L_{\rm 1Mpc}$, then by using a scaling relation between $L_{\rm 1Mpc}$ and the cluster virial radius r_{200}, they computed r_{200}. The scaling relation is expressed as follows:

$$\log(r_{200}) = (-0.57 \pm 0.09) + (0.44 \pm 0.05)\log(L_{\rm 1Mpc}). \tag{5.1}$$

Then, the authors computed the total luminosity within the r_{200} radius, and the cluster

richness. The optical richness, R_{L200}, was used as a proxy for the cluster mass, M_{200}, within r_{200}. The final catalog includes the data of BCG angular positions and redshifts of $132,684$ clusters within the redshift range $0.05 \leq z \leq 0.8$, almost $38,000$ of which have a spectroscopic redshift. The identified clusters have masses above 10^{13} $M_{\odot}$. The authors claim that this catalog is almost complete in the redshift range $0.05 \leq z < 0.42$ and for masses above 10^{14} $M_{\odot}$, while the catalog is less complete and have a biased smaller richness at $z > 0.42$.

In the WHL15 catalog the authors re-calibrated the cluster masses. Specifically, they collected the masses of 1191 WHL12 clusters estimated by X-ray or SZ effect, which lie within the redshift range $0.05 < z < 0.75$, and calculated the optical richness, R_{L500}, within the cluster radius r_{500} for these clusters. Then, by using the new mass measurements, they re-calibrated the richness-mass relation for every cluster in the catalog. The calibrated relation used to estimate the mass M_{500} can be expressed as follows:

$$\log(M_{500}) = 14 + (1.08 \pm 0.02)\log(R_{L500}) - (1.37 \pm 0.02). \tag{5.2}$$

By using the spectroscopic data of the SDSS twelfth data release (DR12), the authors also extended the number of clusters with spectroscopic redshift.

5.1.2 The DESI Cluster Catalog

We also exploit the catalog described in Zou et al. [2021]. This cluster sample has been obtained by applying a new fast clustering algorithm, the so-called *Clustering by Fast Search and Find of Density Peaks* (CFSFDP; Gao et al. [2020]), on the galaxy catalog described in Zou et al. [2019]. The CFSFDP identifies the clusters as the regions that have a higher galaxy density than the field. The galaxy catalog contains the photometric data from the latest data release of the Dark Energy Survey Instrument (DESI). This catalog has data of almost 0.3 billion galaxies with apparent r-band magnitude less than 23, and it covers a sky area of about 2×10^4 deg^2. From this catalog of galaxies the authors selected only those which have an absolute magnitude in r-band less than 20.5 and a photometric redshift error less than 0.1; then, they applied the CFSFDP. The galaxies in the photometric catalog were divided in small equal-area sky pixels through the Hierarchical Equal Area and isoLatitude Pixelisation (HEALPix). Each pixel has an area of about 0.89 deg^2. For each galaxy at a given redshift in a specified HEALPix pixel, the local density, Φ, and the background density, Φ_{bkg}, were calculated. To compute these quantities, the selected pixel and the surrounding eight pixels were considered, so the sky area is almost 8 deg^2. The local density Φ was computed as the number of galaxies with a distance, R, less then 0.5 Mpc within a redshift slice of $z \pm 0.04(1+z)$. To compute the comoving distances the authors assumed the ΛCDM cosmological model with $H_0 = 70\,\mathrm{km\,s^{-1}}$, $\Omega_m = 0.3$ and $\Omega_\Lambda = 0.7$. On the other hand, Φ_{bkg} was computed as the number of galaxies with $R > 1$ Mpc in the same redshift slice. Thus, the cluster centers were identified as the positions of the galaxies with $\Phi > 4\Phi_{bkg}$ and $D > 1$ Mpc, where D is defined as the shortest distance of the specified galaxy to other galaxies with higher Φ. In case there are multiple galaxies with the

same Φ, the authors considered the brightest galaxy in r-band as the center. This cluster center is not always the cluster BCG, which was recognized as the brightest galaxy in r-band within 0.5 Mpc around the density peak. After that, the authors calculated the number of galaxies within 1 Mpc around the cluster center, N_{1Mpc}, which was corrected for the background. An identified cluster was required to have N_{1Mpc} greater than 10. Then, they computed the total r-band luminosity within 1 Mpc, L_{1Mpc}, which was corrected for the background luminosity and it was considered as the proxy of the cluster mass. The $L_{1Mpc} - M_{500}$ relation was calibrated by using mass estimates from X-ray and SZ surveys; this relation can be expressed as follows:

$$\log(M_{500}) = (0.81 \pm 0.02)\log(L_{1Mpc}) + (0.50 \pm 0.14)\log(1+z) + (12.61 \pm 0.04). \quad (5.3)$$

The final catalog contains $540,932$ clusters at $z \leq 1$, almost $122,000$ of which having a spectroscopic identification of the BCG. The cluster sample has a mean redshift of about 0.53 and a median mass of 1.2×10^{14} $M_{\odot}$.

5.2 The Spectroscopic Galaxy Catalog

In this section we describe the galaxy public data that we cross-correlate with the cluster catalogs, in order to find the cluster member galaxies.

We exploit the galaxy coordinates and spectroscopic redshifts derived from the sixteenth data release (DR16) of the Sloan Digital Sky Survey (SDSS; Ahumada et al. [2020]). Specifically, we analyze the data collected by the Baryon Oscillation Spectroscopic Survey (BOSS; Dawson et al. [2012]), the Extended Baryon Oscillation Spectroscopic Survey (eBOSS; Dawson et al. [2016]) and the Legacy Survey obtained as part of the SDSS-I and SDSS-II programs, [York et al., 2000]. Although the spectroscopic data and the sky coverage of the galaxy samples have remained unchanged during the past years, the imaging and the spectroscopic pipelines have been improved in subsequent SDSS data releases. Therefore, in this work we use the data of the latest release.

The Legacy Survey was originally designed to investigate the large-scale structure of the universe. This survey covers a total sky area of 8032 deg^2 and it is composed of two galaxy samples:

- The *Main sample*: a magnitude limited sample of galaxies with a mean redshift of $z \simeq 0.1$, [Strauss et al., 2002]
- The *Luminous Red Galaxies sample* (LRGs), [Eisenstein, 2001].

Within the Legacy Survey, we select the galaxies with the most reliable spectra and the lowest redshift errors. Specifically, we select the objects in the catalog which have the following flags[1]:

[1]The official SDSS DR16 web site (https://www.sdss.org/dr16/) provides a detailed description of the flags in the spectroscopic catalogs.

- *SPECPRIMARY*: equal to 1. This flag indicates if the selected object is a primary target of the survey. This selection ensures that in the final catalog there are not multiple entries of the same object.

- *CLASS*: "Galaxy". This flag indicates the type of the selected object, it is needed because inside the SDSS public catalogs there are data for galaxies, stars and quasars. This selection ensures that we only take data from objects recognized as galaxies.

- *ZWARNING*: equal to 0, 4 or 16; with this selection we make ensures that we take objects with a reliable spectroscopic redshift estimation. In fact, this flag indicates if there are problems with the fitting procedure used to recover the spectroscopic redshift. When this flag is set equal to 0 or 16 means that there are not any problems in the sprectrum fit, while if it is set equal to 4 means that there are many outliers in the spectrum, but the spectroscopic redshift measurement is reliable.

- *ZERR*: less than 6×10^{-4}. This flag indicates the error, resulting from the fit of the spectrum, of the estimated spectroscopic redshift. We only select galaxies with low redshift errors.

- *Z*: between 0.05 and 0.75 included.

We find almost $760,000$ galaxies within the Legacy Survey that are useful for our analysis.

BOSS is a part of the six-year SDSS-III program, that obtained the spectroscopic redshifts of 1.5 million LRGs out to a redshift of almost 0.7. We also include data from the eBOSS, which obtained the spectroscopic redshifts of LRGs, Emitting Luminous Red Galaxies (eLRGs) and quasars (QSO), up to $z = 3.5$. We select galaxies form these surveys using similar flags[2] to the Legacy survey case. We consider the objects which have the flag *SPECPRIMARY* equal to 1 and we select those which have *CLASS_NOQSO* equal to "Galaxy". We consider the galaxies with the most reliable redshift estimation by selecting those which have the flag *ZWARNING_NOQSO* equal to 0, 4 or 16, and the flag *ZERR_NOQSO* less than 6×10^{-4}. Finally, we select the galaxies with redshift 0.05 and 0.75 included by using the flag *Z_NOQSO*. We find about 1.9 million galaxies useful for our analysis within the BOSS and the eBOSS.

Figure 5.1 shows the angular positions of the selected galaxies, in Right Ascension (R.A.) and Declination (Dec.) coordinates, within the Legacy Survey (left panel) and within BOSS and eBOSS (right panel). Figure (5.2) shows the redshift distribution of the galaxies inside the exploited sample. The mean galaxy redshift within the Legacy survey is $z \simeq 0.16$, while BOSS and eBOSS galaxies have a mean redshift of $z \simeq 0.48$.

[2]The flags that end with *_NOQSO* are specific for the BOSS and eBOSS galaxies. The description of the flags and their meaning are the same as in the Legacy Survey.

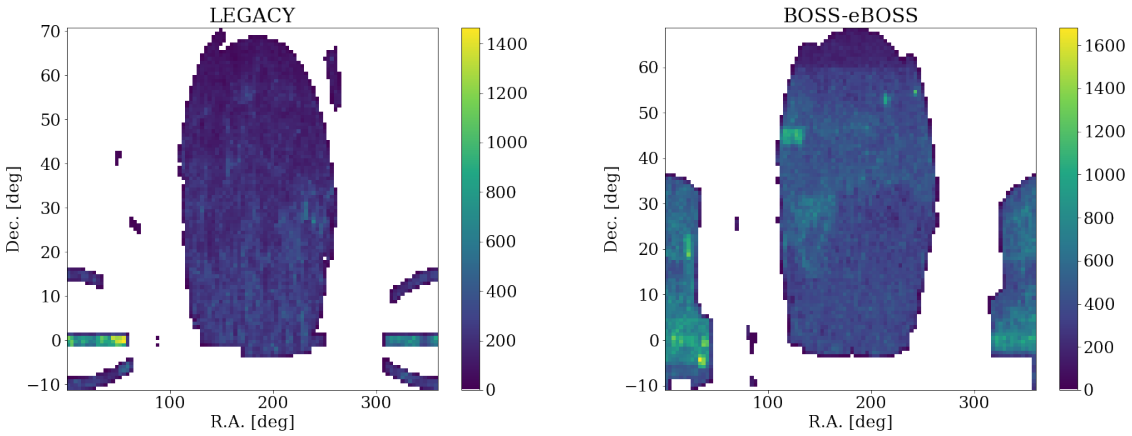

(a) (b)

Figure 5.1: Angular positions of the selected galaxies. The color bar shows the number of galaxies in each bin of sky area. Each bin has an area of almost 2.9 deg^2. The left panel shows the selected galaxies within the Legacy Survey, while the right panel shows the selected galaxies within BOSS and eBOSS.

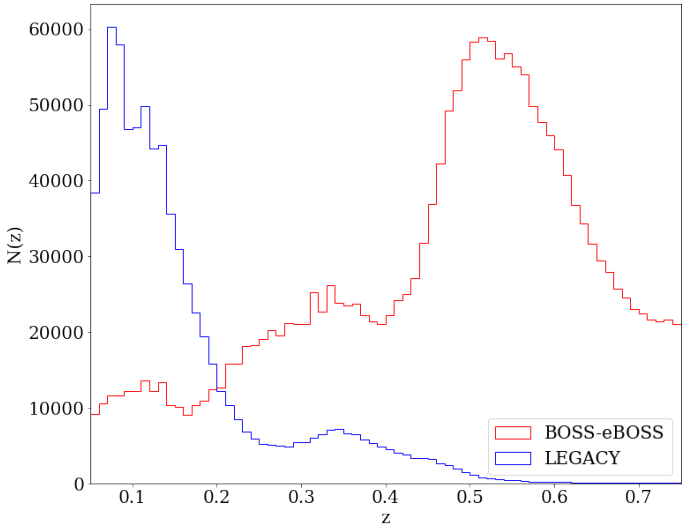

Figure 5.2: Redshift distribution of the selected galaxies. The blue line represents the galaxy redshift distribution within the Legacy Survey, while the red line shows the distribution within BOSS and eBOSS.

5.3 Searching for Cluster Member Galaxies

To recover the signal of the gravitational redshift effect, it is necessary to calculate the distribution of the galaxy line-of-sight velocity offsets, Δ, as a function of the cluster radius, which is described in Eq.(4.3). To compute Δ we construct two new catalogs of cluster member galaxies by cross-correlating the cluster catalogs, described in Sec.5.1, with the public galaxy data, described in Sec.5.2.

To find the cluster member galaxies we compute the projected transverse distance, $r_\perp$, and the Δ of all the galaxies with respect to each cluster center. We define the cluster center as the mean values of angular positions and redshifts of the BCG closest galaxies, which have a transverse distance less than r_{500} from the BCG.

The WHL15 and DESI cluster catalogs, described in Sec.5.1, provide the BCG angular positions of the identified clusters. However, most of the BCG do not have a spectroscopic measurement of their redshift. Thus, to increase the number of the available spectroscopic BCGs, we cross-match the cluster samples with the galaxy catalog, in order to identify the cluster BCGs inside the galaxy sample we exploit. We take into account the fact that, according to SDSS specifications, two galaxies are considered the same object if they are closer than 3 arcsecs, in the Legacy Survey case, and 2 arcsecs, in BOSS and eBOSS survey case. Thus, we consider the cluster member galaxies only inside clusters which have the BCG identified in the galaxy catalog, described in Sec.5.2. The advantage of doing so is that we increase the statistics of the cluster samples, and we make sure that we only analyze clusters which have a reliable spectroscopic redshift measurement of their centers. We cross-match the WHL15 catalogs and the SDSS data, and we obtain $85,588$ clusters with a spectroscopic BCG identification; $47,779$ of these have the BCG identified in BOSS and eBOSS, while the other $37,809$ clusters have the BCG identified in the Legacy Survey. On the other hand, by cross-matching the DESI catalog and the galaxy catalogs, we obtain $114,527$ clusters with a spectroscopic BCG identification; $80,827$ of these have the BCG identified in BOSS and eBOSS, while the other $33,700$ clusters have the BCG identified in the Legacy Survey.

Once we have identified the cluster BCGs, we search for the closest galaxies to define a new cluster center. To obtain the new centers we compute the projected transverse distances and the line-of-sight velocities of all the SDSS galaxies with respect to the BCGs. We keep the galaxies which lie within a separation of $r_\perp < r_{500}$ and $|\Delta| < 2,500$ km s^{-1} from the BCGs. It should be noted that in this work we use the transverse distance in units of r_{500}, so we can take advantage of the self-similarity of the clusters. The WHL15 and the DESI cluster catalogs have an average r_{500} of about 0.67 Mpc. To calculate the transverse distance between a galaxy and the BCG we assume the cosmological model described in Sec.2.4. For each cluster in our catalog, we compute the average value of the redshifts and angular positions of the selected galaxies, including the BCG, and we define these averages as the new cluster centers. It should be noted that this center definition has never been used in the past literature to perform the measurement of the gravitational redshift in galaxy clusters. In fact, the past literature works, such as Wojtak et al. [2011] and Jimeno et al. [2014], assume that the cluster center coincides

with the BCG position. However, the average of the member galaxy positions provides a more reliable location of the center than the BCG, because the BCG could be misidentified due to the surface brightness modulation effect. In fact, the peculiar velocities can change the ranking of the two cluster brightest galaxies.

Once we have defined the cluster center, we reselect the cluster member galaxies. We consider a galaxy to be a cluster member if it lies within a separation of $r_\perp < 4\ r_{500}$ and $|\Delta| < 4,000$ km s^{-1} from the cluster center. Hence, we create a cluster member catalog given the galaxy position average described above as the center, and we retrieve the galaxy line-of-sight velocity distribution Δ_{mean}[3]. This searching procedure is repeated both for the cluster member galaxies in the WHL15 cluster catalog, as well as for those in the DESI cluster catalog. It should be noted that the galaxies which have $|\Delta|$ between $3,000$ km s^{-1} and $4,000$ km s^{-1} are considered as either foreground or background galaxies, which are not gravitational bound to any cluster. We include these galaxies in the catalogs because they are used to correct the velocity distributions of the galaxies which effectively lie within the cluster gravitational potential well, as described in Sec.6.1.1.

Before proceeding with the measure of the gravitational redshift, we make some further selections on the catalogs. Firstly, we discard the clusters which have a redshift above 0.5, in both cluster member catalogs. We make this selection in order to avoid the redshift range where the possibility of a cluster false identification is higher than about the 5% in both the exploited cluster catalogs, as described in Wen et al. [2015] and Zou et al. [2021]. Moreover, by applying the redshift selection, we work in a low redshift region, where the impact of the assumed cosmological model is not significant, as claimed in Wojtak et al. [2011]. We discuss the impact of this selection on the measurements in Appendix A. Then, we consider only the clusters which have at least 4 associated galaxies and the clusters where the average center is computed using data of at least 3 galaxies, including the BCG. We make the latter selection in order to be conservative and to analyze the clusters which have their centers estimate with a sufficient number of galaxies. Also these selections are discussed in Appendix A.

When the cluster mass increases, the gravitational redshift effect becomes stronger and the probability to have a cluster false identification decreases. Moreover, Δ measured in low-mass clusters is more affected by the galaxy peculiar velocities than the one which is measured in high-mass clusters. To minimize these possible sources of systematic uncertainties, we select the clusters which have a mass above than 1.5×10^{14} M$_\odot$. This selection is discussed in Appendix A.

Finally, we discard the configurations in which Legacy and BOSS-eBOSS spectra were mixed together. That is, the cluster member galaxies (comprising the BCG) of the Legacy cluster sample are selected only from the Legacy spectroscopic galaxy sample, while the ones of the BOSS-eBOSS cluster sample are selected only from the BOSS-eBOSS galaxy sample. We choose to do this because the mixed configurations suppress the gravitational redshift signal for small values of transverse distances, as demonstrated by Sadeh et al. [2015].

[3]We include the BCG in the galaxy sample when we calculate Δ_{mean}.

The characteristics of the final cluster member catalogs (i.e. the number of clusters and associated member galaxies, the average redshift and the average mass) are shown in Table 5.1. Figure 5.3 shows the redshift (left panel) and mass (right panel) distributions of the final WHL15 cluster member catalog, while Fig.5.4 shows the same for the final DESI cluster member catalog.

	WHL15	DESI
number of clusters	$3,014$	$2,040$
number of member galaxies	$49,243$	$41,023$
average z	0.25	0.23
average M_{500} [$M_{\odot}$]	2.75×10^{14}	2.69×10^{14}

Table 5.1: The table shows the number of clusters and associated member galaxies, the average redshift and the average mass, for both the constructed cluster member catalogs.

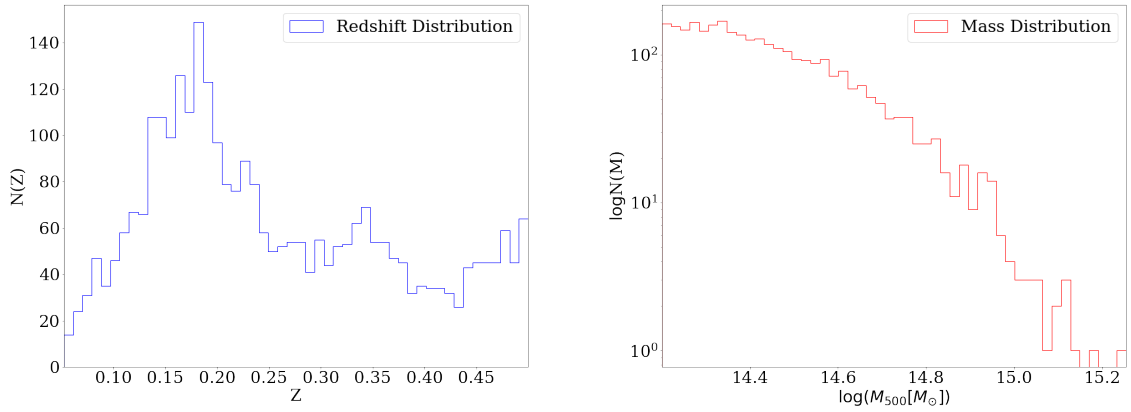

(a) (b)

Figure 5.3: Redshift distribution (left panel) and mass distribution (right panel) of the cluster member catalog constructed by using WHL15 cluster data.

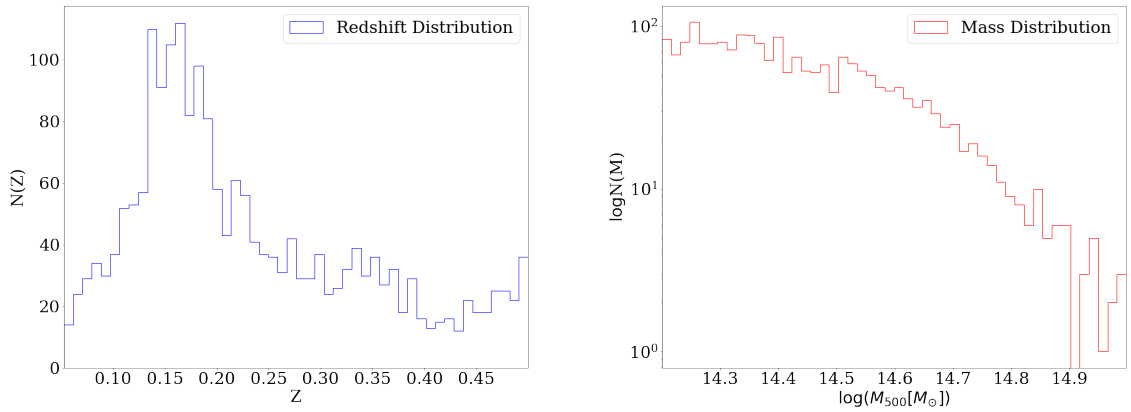

(a) (b)

Figure 5.4: Such as Fig.5.3 for the cluster member catalog constructed by using DESI cluster data.

To summarize, we constructed two new catalogs of cluster member galaxies, never exploited in the past literature, by using the public available data of galaxy (Sec.5.2) and cluster catalogs (Sec.5.1.1 and Sec.5.1.2). For each catalog we defined the cluster center as the average positions of the BCG closest galaxies, and we have used this center to compute the distributions Δ_{mean}. The described selection method ensures that all the galaxies we have identified as cluster members have a reliable estimate of their spectroscopic redshift. Differently from these past literature works of Wojtak et al. [2011] and Jimeno et al. [2014], we take advantage of the cluster self-similarity by computing the transverse distances in unit of r_{500}. Moreover, we perform a background correction technique on the phase-space diagram of the cluster members in order to remove the contamination of the foreground and background galaxies, this correction is described in Sec.6.1.1. Thanks to these improvements we are able to reduce the measurement errors by about the 15% respect to the past literature works described in Chapter 4, up to a distance of almost 3 Mpc from the cluster center.

In order to investigate the impact of assuming the average galaxy positions as the center of the cluster potential wells, we compare the results to the ones obtained by assuming instead the BCG as the cluster center, as done in past literature works [see Wojtak et al., 2011, Jimeno et al., 2014, Sadeh et al., 2015]. Thus, we construct the cluster member catalog by using the same selection criteria described in this Section. This searching procedure is repeated both for the cluster member galaxies in the WHL15 cluster catalog, as well as for those in the DESI cluster catalog. The analyses on the cluster member catalogs, which are constructed assuming the BCG as the cluster centers, are described in Appendix A.

Chapter 6

Results

In this Chapter we describe the method we use to recover the signal of the gravitational redshift effect in the data described in Chapter 5. We present how we calculate the theoretical model for the three considered gravity theories, following the prescriptions described in Chapter 4. Finally, we describe the obtained results.

6.1 Measurement Method

6.1.1 Correction of the Phase-Space Diagrams

To measure the gravitational redshift effect from the cluster member catalogs constructed in Sec.5.3, we stack all the data of the member galaxies (i.e. the transverse distances $r_\perp$, and line-of-sight velocities Δ) in a single phase-space diagram [Kim and Croft, 2004, Wojtak et al., 2011]. Figure 6.1 shows the stacked line-of-sight velocity offset distributions for the member galaxies in the WHL15 catalog, while Fig.6.2 shows the same for the member galaxies in the DESI catalog.

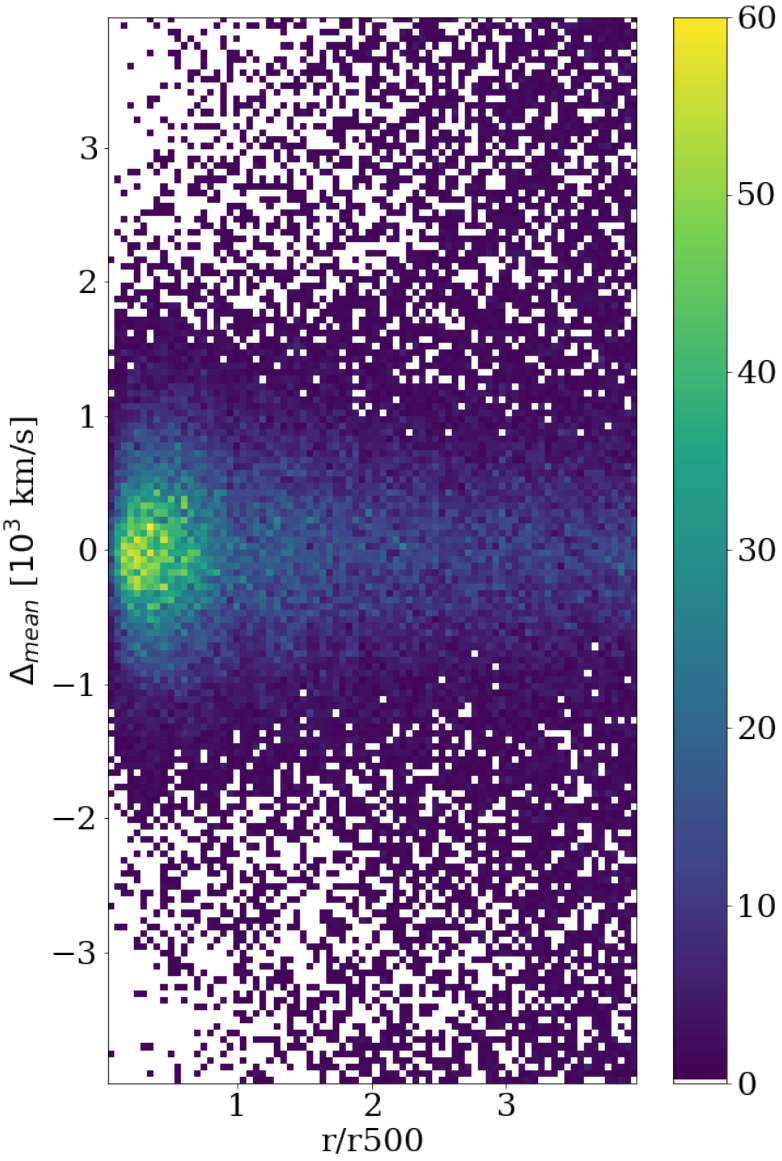

Figure 6.1: Phase-space diagram for the stacked member galaxy data of the clusters in the WHL15 catalog, assuming the average of the positions and redshifts of the cluster members as the centers. The color bar shows the number of member galaxies we have in each bin. The bins have a size of $0.05\ r_{500} \times 50$ km s^{-1}.

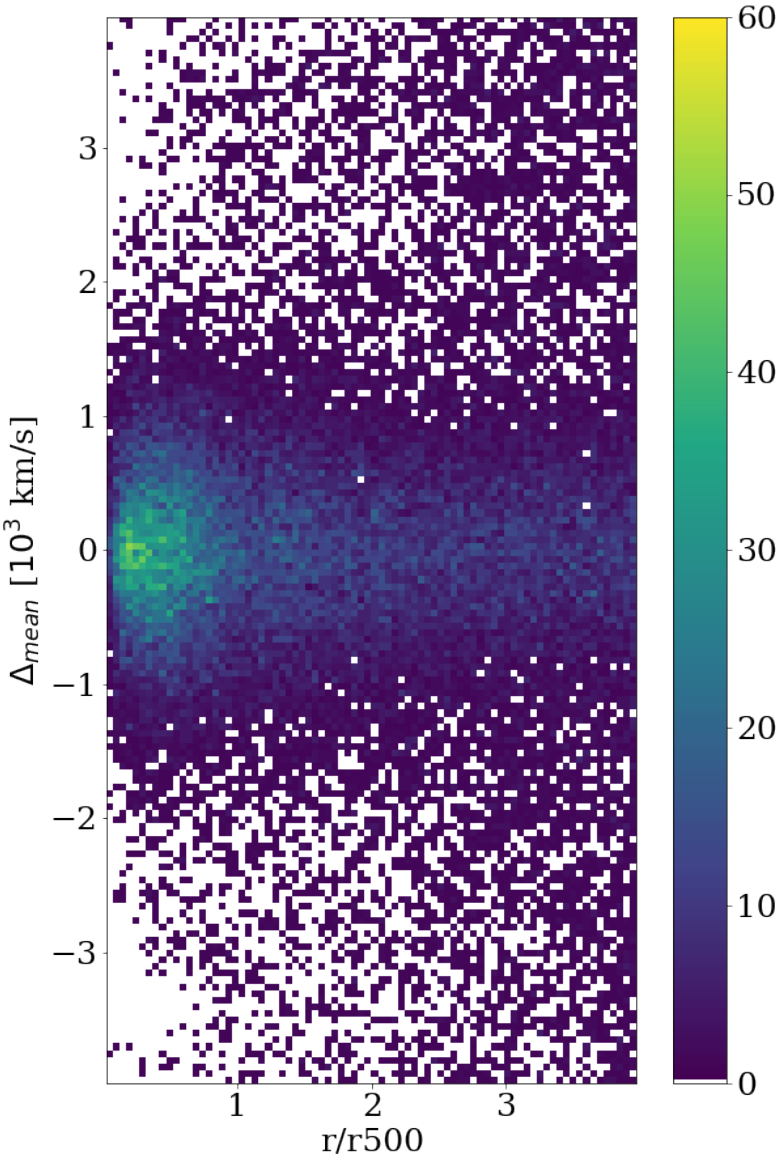

Figure 6.2: Phase-space diagram for the stacked member galaxy data of the clusters in the DESI catalog. The symbols are the same as Fig.6.1.

The phase-space diagrams, which are shown in Fig.6.1 and Fig.6.2, are affected by the contamination of the foreground and background galaxies, which are not gravitationally bound to any cluster, due to projection effects. To make a reliable measurement of the gravitational redshift we have to take into account only the galaxies that are within the cluster gravitational potential well, thus we have to deal with the foreground and background galaxy contamination. To remove the contamination of these galaxies, we follow the procedure described in Jimeno et al. [2014]. The galaxies, which do not belong to any cluster, are considered statistically, once the data of all cluster member galaxies have been stacked into a single phase-space diagram (see Wojtak et al. [2007] for a detailed review over foreground and background galaxies removal techniques). Firstly, we split the phase-space distribution in bins of size $0.05\ r_{500} \times 50$ km s^{-1}. We assume that the galaxies which lie in the stripes $3,000$ km s$^{-1} < |\Delta| < 4,000$ km s^{-1} belong either to the pure foreground or to the pure background. Then, we fit a quadratic polynomial function, which depends on both Δ and $r_\perp$, to the points in both stripes. We use the interpolated model to correct the phase-space region where $|\Delta|$ is less than $3,000$ km s^{-1}, namely the region where the galaxies are gravitationally bound. The function $f(r_\perp, \Delta)$, that we use to model the phase-space region where the background and foreground galaxies lie, can be expressed as follows:

$$f(r_\perp, \Delta) = ar_\perp^2 + b\Delta^2 + c\Delta r_\perp + d\Delta + er_\perp + f. \tag{6.1}$$

We use a function that depends on both $r_\perp$ and Δ because, due to the observational selection, we may observe more galaxies which are close to us with respect to the cluster center (i.e. negative Δ) than further away (i.e. positive Δ). Moreover, the possibility to find galaxies that do not belong to the cluster increases with the distance from the cluster center. Once we have modeled the phase-space region of the foreground and background galaxies, we correct the inner phase-space region using the interpolated model.

Figure 6.3 shows the background-corrected phase-space diagram for member galaxies of the clusters in the WHL15 catalog, while Fig.6.4 shows the background-corrected phase-space diagram for the catalog constructed using the DESI cluster catalog. After removing the background, the phase-space diagrams of Δ_{mean} clearly show the inner region where the gravitationally bound galaxies reside, for both the cluster member catalogs. Indeed, most of the galaxies in the foreground and background regions have been removed, proving that the background-correction method succeeded. However, not all the contamination has been removed because of the intrinsic uncertainties in the fitting. Thus, we will take into account these errors when we fit the galaxy velocity distributions.

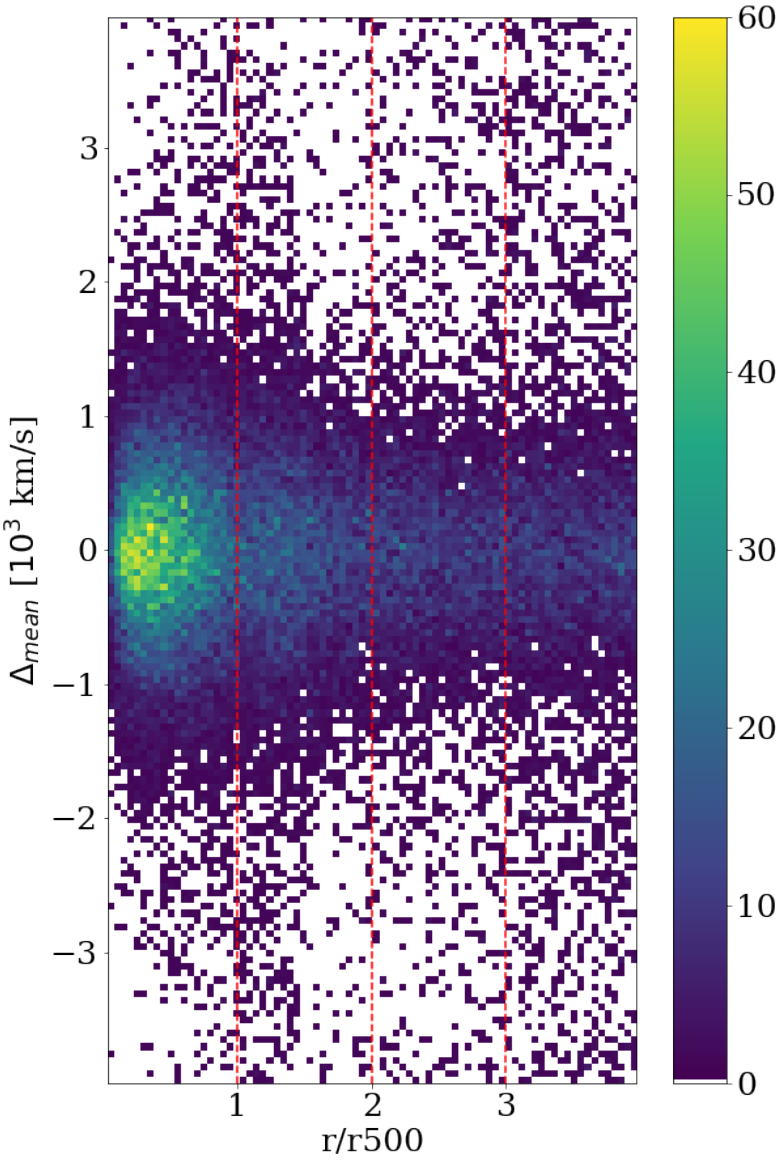

Figure 6.3: Background-corrected phase-space diagram for the stacked member galaxy data of the clusters in the WHL15 catalog. The red lines show the bins where we calculate the mean of the velocity distributions. The color bar shows the number of member galaxies we have in each bin. The bins have a size of $0.05\ r_{500} \times 50$ km s^{-1}.

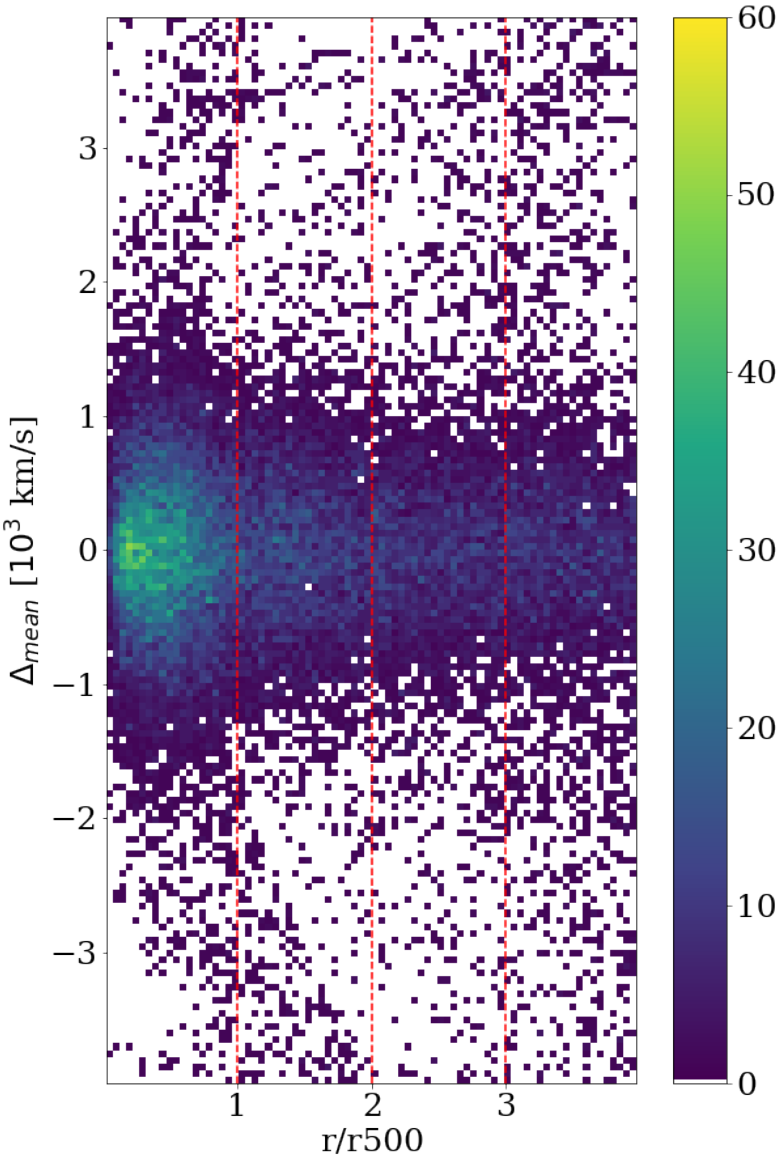

Figure 6.4: Background-corrected phase-space diagram for the stacked member galaxy data of the clusters in the DESI catalog. The symbols are the same as Fig.6.3.

6.1.2 Fitting the Data

In order to recover the gravitational redshift signal as a function of the cluster radius, we split the background-corrected phase-space diagrams into four equal bins of transverse distance. Each bin has a width of one r_{500}, as shown in Fig.6.3 and Fig.6.4. We fit the galaxy line-of-sight velocity distribution within each bin, in order to recover the mean of the distribution, $\hat{\Delta}$. The mean value of the distribution is proportional to the intensity of the gravitational redshift effect and we expect a negative value, as explained in Chapter 4. We perform a Monte Carlo Markov Chain (MCMC) statistical analysis to fit $\hat{\Delta}$ within each bin. We model the velocity distribution as a double Gaussian function, which can be expressed as follows[1]:

$$f(\Delta) = \frac{\varepsilon}{\sqrt{2\pi\sigma_1^2}} \exp\left[\frac{(\Delta-\hat{\Delta})^2}{2\sigma_1^2}\right] + \frac{1-\varepsilon}{\sqrt{2\pi\sigma_2^2}} \exp\left[\frac{(\Delta-\hat{\Delta})^2}{2\sigma_2^2}\right], \tag{6.2}$$

where the two Gaussian functions have the same mean, $\hat{\Delta}$. The relative normalization of the two functions, ε, and their widths, σ_1 and σ_2, are considered as free parameters of the MCMC analysis, and marginalized over. The Bayesan fit is implemented by using a Gaussian likelihood, with flat priors for all the free model parameters. In particular, we impose that $-0.1 \leq \hat{\Delta} \leq 0.1$ [10^3 km s^{-1}], $0 < \sigma_1 \leq 2$ [10^3 km s^{-1}], $\sigma_1 < \sigma_2 \leq 20$ [10^3 km s^{-1}] and $0 < \varepsilon \leq 1$. As distribution errors we consider the combination of two independent sources: i) the Poisson noise and ii) the error of the background-correction method. We use a quasi-Gaussian function (Eq.(6.2)) to take into account for the intrinsic non-Gaussian distributions of galaxy velocities in individual clusters and for the different cluster masses.

Figure 6.5 shows an example of the galaxy velocity distribution in the $2 < r_\perp/r_{500} < 3$ bin and the associated best-fitting model we computed with the MCMC. The gravitational redshift signal (i.e. the negative shift of the mean of the distribution) has a value of about -10 km s^{-1} in the range of cluster masses of the exploited cluster catalog. This signal is about two orders of magnitude smaller than the width of the distribution which represents the velocity dispersion of the stacked cluster member galaxies. We are able to recover the gravitational redshift signal because of the high statistics of the cluster member catalogs we constructed. Figure 6.5 also shows the distribution model computed by imposing $\hat{\Delta} = 0$ (i.e. no gravitational redshift signal). We notice that it is quite impossible to discriminate by eyes between the distributions with and without the gravitational redshift effect. For visual clarity, we zoom in on a region of the distribution. The zoomed region, shown in the small box on the upper left of Fig.6.5, shows that we actually recover the signal of the gravitational redshift, as the two curves are statistically distinguished. Thanks to the MCMC analysis, we can indeed recover the intensity of the gravitational redshift effect by fitting the cluster member velocity data, despite the small signal, thanks to the high statistics of the constructed cluster member catalogs.

[1]The new likelihood algorithms will be released in the forthcoming public version of the CBL [Marulli et al., 2016].

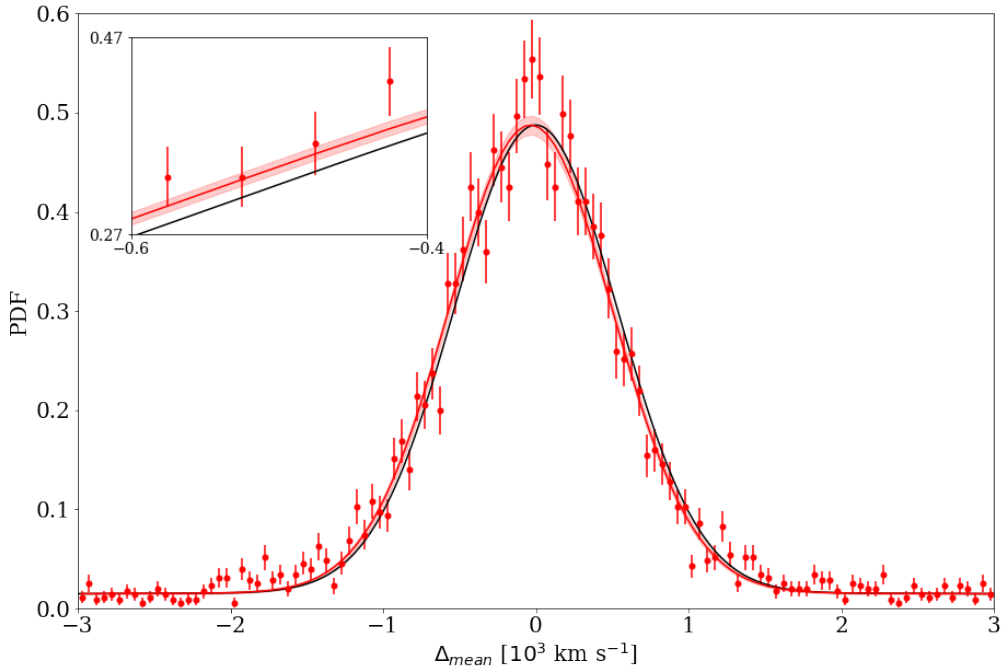

Figure 6.5: Example of the galaxy velocity distribution in the $2 < r_\perp/r_{500} < 3$ bin of projected transverse distance. The red points represent the data of the binned background-corrected phase-space diagram and the error bars represent the Poisson noise combined with the error of the background-correction method. The red solid lines show the best-fitting model and the red shaded area shows the best-fitting error. The black solid curve shows the fitting model (Eq.6.2) computed with $\hat{\Delta} = 0$. In the small box on the upper left we zoom in a region of the distribution to visually clarify that the two curves are statistically distinguished.

6.2 Computing the Theoretical Models

To compute the predictions of the gravitational redshift effect in any theory of gravity we need to use Eq.(4.45). Specifically, we need to calculate the gravitational and the TD effects, as well as $\delta(z)$, to account for the four largest contributions in $\hat{\Delta}$. We calculate the gravitational effect by solving Eq.(4.11), while the TD effect is computed using Eq.(4.37). To solve these integrals we use the cluster mass distributions shown in Fig.5.3 for the clusters in the WHL15 catalog and in Fig.5.4 for clusters in the DESI catalog. The value of $\delta(z)$ depends strongly on the galaxy sample, which is described in Sec.5.2. The $\delta(z)$ computation is described in the following Section.

6.2.1 Computing the Surface Brightness Modulation Effect

To compute the intensity of the SB effect (Eq.(4.42)) we follow the process described in Kaiser [2013]. We have to calculate the redshift dependent logarithmic derivative of the number distribution of galaxies, $\delta(z)$, defined as:

$$\delta(z) := \frac{\mathrm{d}\log n(< M_{lim}(z))}{\mathrm{d}\log M}, \tag{6.3}$$

where M_{lim} is the absolute magnitude limit of the galaxy survey. For the galaxy luminosity function we use the value from Montero-Dorta and Prada [2009], where the r-band luminosity function is modeled as a Schecter function, K-corrected to $z = 0.1$, which has a characteristic magnitude $M_* - 5\log_{10} h = -20.7$ and a faint end slope $\alpha = -1.26$. Ideally, we should use a specific luminosity function of the cluster member galaxies. However, Hansen et al. [2009] demonstrated that the overall luminosity function for the cluster member galaxies does not vary significantly from the luminosity function of the field galaxies. Then, we assume an overall luminosity function, as it was done in the past literature [see Kaiser, 2013, Jimeno et al., 2014, Mpetha et al., 2021].

To calculate $\delta(z)$ we use the SDSS fibre magnitude limit in r-band, which has a value of 22.29 [2], as the magnitude cut. Figure 6.6 shows the function $\delta(z)$ we calculate for the exploited galaxy catalog, which is an increasing function of the redshift, as expected.

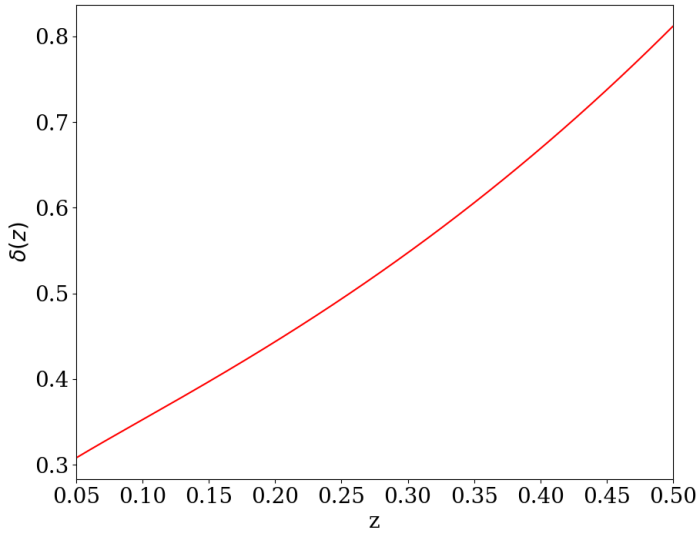

Figure 6.6: Logarithmic derivative of the galaxy number density as a function of redshift. The plot is limited to the redshift range considered in this work.

[2]This value is taken from the SDSS offical web site, see https://www.sdss.org/dr12/algorithms/magnitudes

To compute the intensity of the SB effect we need to calculate the average value of $\delta(z)$ over the cluster sample redshift range, $\langle\delta(z)\rangle$, by solving the following integral:

$$\langle\delta(z)\rangle = \frac{\int_{z_1}^{z_2} \delta(z)(\mathrm{d}N/\mathrm{d}z)\mathrm{d}z}{\int_{z_1}^{z_2}(\mathrm{d}N/\mathrm{d}z)\mathrm{d}z}, \tag{6.4}$$

where $z_1 = 0.05$ and $z_2 = 0.5$ are the lower and upper redshift limits in the exploited cluster member catalogs. To solve the integral in Eq.(6.4) we consider, as $\mathrm{d}N/\mathrm{d}z$, the galaxy redshift distribution which is shown in Fig.5.2. The result of the integral computation is:

$$\langle\delta(z)\rangle = 0.516, \tag{6.5}$$

which is the same for both the clusters in the WHL15 catalog and the clusters in the DESI catalog, because the SB effects depends only on the galaxy sample.

6.2.2 Computing the Concentration Parameter

To compute the prediction of the gravitational redshift effect, described in Chapter 4, we need the concentration parameter, c_{500}, for every analyzed cluster. The parameters we have to characterize the clusters are: the redshift, M_{500} and r_{500}. The latter two are the mass and the radius where the cluster density is 500 times the Universe critical density, ρ_c. In order to calculate c_{500} for each cluster in our sample, we develop this method:

1. For each cluster redshift in the exploited catalogs, we construct a sample of virtual clusters which are characterized by the mass M_{200}. The mass range of these virtual clusters is greater than the mass range of the exploited cluster catalogs. Then, we use the $M_{200} - c_{200}$ relation described in Duffy et al. [2008], to calculate c_{200} for every cluster in the virtual sample. For the computation we assume that the DM density profile inside the clusters follows the NFW profile.

2. Given M_{200} and c_{200}, we calculate M_{500} for every virtual cluster, by solving the following equation:

$$M_{500} = \frac{5}{2x^3} M_{200}, \tag{6.6}$$

   where $x := r_{200}/r_{500}$, and $c_{500} = c_{200}/x$. By doing so, we obtain the corresponding M_{500} for every virtual cluster. Then, we fit the relation $M_{200} - M_{500}$, which we model as a polynomial function, for the virtual clusters.

3. For every cluster in the exploited catalogs, we retrieve the corresponding M_{200}, given the measured M_{500}, by using the relation we have found for the virtual clusters. Then, we

use the Duffy relation to compute c_{200} for the real clusters. Finally, we calculate c_{500} by solving the following equation:

$$\frac{M_{200}}{M_{500}} g(c_{500}) - g(c_{200}) = 0, \tag{6.7}$$

where $g(c)$ is the function defined in Eq.(4.7).

By using the described procedure, we get the parameter c_{500} for every cluster in the WHL15 and DESI catalogs. Once we have computed c_{500}, we can calculate the theoretical predictions for the value of $\hat{\Delta}$ in any theory of gravity. The computed theoretical value of $\hat{\Delta}$ is described in the following Section.

6.2.3 Theoretical Predictions of the Gravitational Redshift Effect

Using Eq.(4.45) and following the method described in Chapter 4, we compute the model for $\hat{\Delta}$ as a function of cluster radius and mass in three different theories of gravity: GR, $f(R)$ and sDGP.

Figure 6.7 shows the predicted value of $\hat{\Delta}$ as a function of the cluster radius in unit of r_{500}, while Fig.6.8 shows the predicted gravitational redshift effect as a function of the cluster mass. The two figures show not only the combined effect given by Eq.(4.45), but also the gravitational, TD and SB effects individually. It should be noted that Fig.6.7 and Fig.6.8 are referred to the WHL15 catalog, but the predicted $\hat{\Delta}$ is almost the same in the DESI catalog, as well as the various effects.

Figure 6.7 shows that the value of $\hat{\Delta}$ becomes more negative as the cluster radius increases. This is expected because $\hat{\Delta}$ gives us information about the difference between the gravitational potential in the center and the potential at a given radius. Thus, since the gravitational potential well is deeper in the cluster center, the signal of the gravitational redshift effect is stronger at larger radii. However, this effect does not grow infinitely as the distance from the center increases, but it reaches a constant value when we analyze regions that are outside the cluster. Figure 6.7 also shows that the TD effect causes a positive shift of $\hat{\Delta}$, while the SB effect causes a negative shift, as described in Sec.4.4. The TD and SB effects are small compared to the gravitational effect.

Furthermore, Fig.6.7 shows that the $f(R)$ theory predicts a more negative value of $\hat{\Delta}$ than the GR, at any radius. This is caused by the enhancement of the gravitational force described in Sec.4.2. On the other hand, the sDGP model predicts a value of $\hat{\Delta}$ almost equal to that of the GR at small radii, while the sDGP gravitational redshift effect becomes less strong as the cluster radius increases, as described in Sec.4.3.

Figure 6.8 shows the GR, $f(R)$ and sDGP predictions of the gravitational redshift effect as a function of the cluster mass. We compute these predictions considering the integrated gravitational redshift signal up to a distance of $4\ r_{500}$ from the cluster center. We calculate the model as a function of the cluster mass because Kim and Croft [2004] pointed out that

for a complete detection of the gravitational redshift effect in galaxy clusters it is necessary to detect that the signal becomes more negative as the cluster mass increases. This is because the gravitational potential well becomes deeper as the cluster mass rises. Figure 6.8 shows that the TD effect causes a positive shift of $\hat{\Delta}$, while the SB effect causes a negative shift, and the two effects are small corrections of the gravitational effect. In this case, the sDGP model predicts a less intense effect than the GR at any mass, while the $f(R)$ theory predicts an effect that is always stronger. The measurements of the gravitational redshift effect as a function of the cluster mass are described in Appendix A.

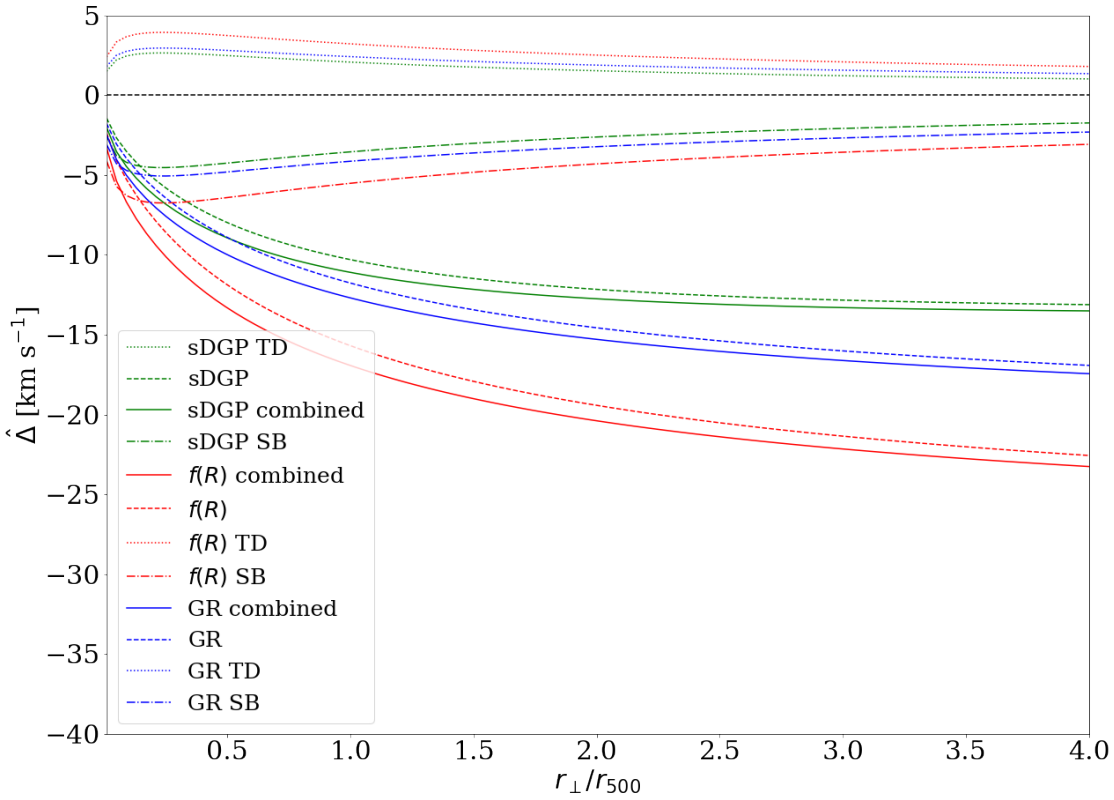

Figure 6.7: Predicted value of $\hat{\Delta}$ as a function of the cluster radius in unit of r_{500} for the WHL15 catalog. The blue lines refer to the predictions computed assuming GR, the green lines refers to the sDGP predictions and the red lines refers to $f(R)$ gravity theory. For each color, the dashed line shows the gravitational effect, the dotted line the TD effect, the dot-dashed line the SB effect, while the solid line is the combined effect.

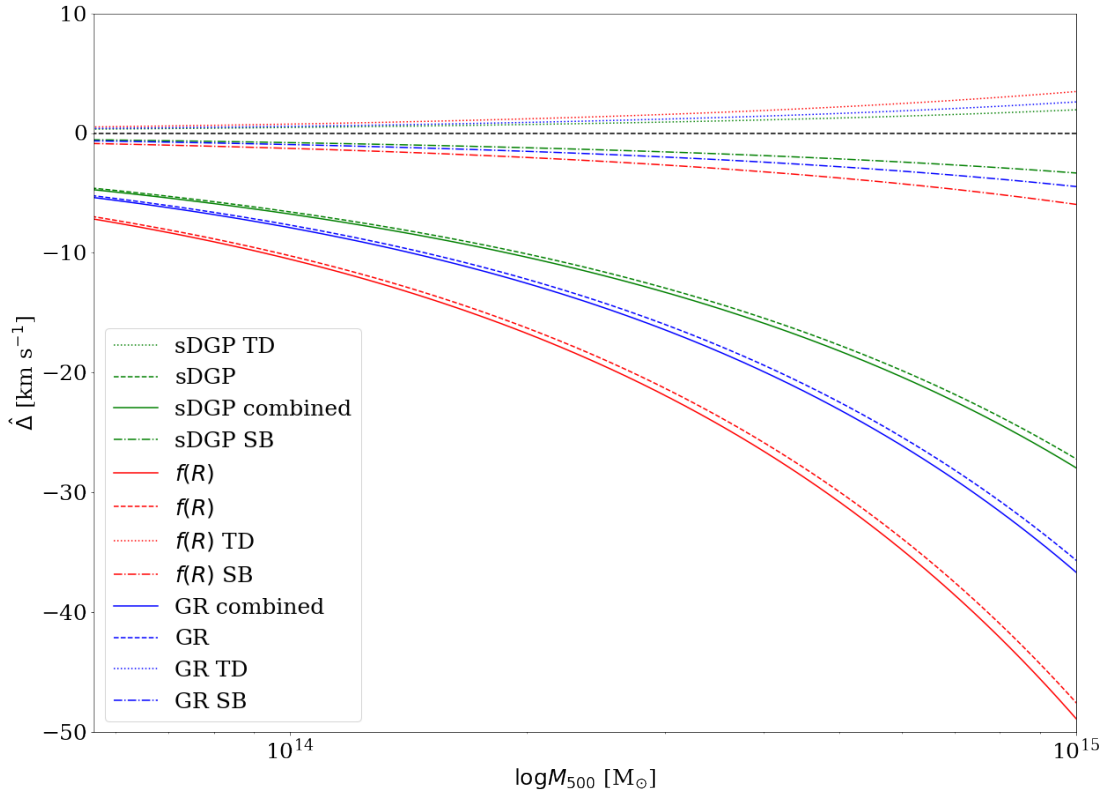

Figure 6.8: Predicted value of the integrated $\hat{\Delta}$ up to $4\ r_{500}$ as a function of the cluster mass for the WHL15 catalog. The symbols are the same as in Fig.6.7.

6.3 Gravitational Redshift Measurements

In this Section we describe the measurements of the velocity distributions of the cluster member galaxies of the WHL15 and DESI cluster catalogs. These results are obtained by selecting the clusters and the cluster member galaxies as described in Sec.5.3. For the sake of completeness, we investigate also how the results change when we modify the adopted selections. These analyses are described in Appendix A.

6.3.1 Gravitational Redshifts in WHL15 Cluster Catalog

In this Section we present the measurement results of the velocity distributions of the cluster member galaxies of the WHL15 cluster catalog.

We split the background-corrected phase-space diagrams, shown in Fig.6.3, into four equal bins of transverse distance. To recover the mean of the distribution, we fit the galaxy line-of-sight velocity distribution within each bin by using the method described in Sec.6.1.2. Figure 6.9 shows the velocity distributions in each bin of projected transverse distance assuming the average positions of the BCG closest galaxies as the cluster center. The figure shows the data of the binned background-corrected phase-space diagram and the associated error bars. As described in Sec.6.1.2, the errors are the result of two independent sources: i) the Poisson noise and ii) the error of the background-correction method. Figure 6.9 shows also the best-fit models within each bin (Eq.(6.2)). The reduced χ^2 is about 2 for all the best-fitting models we computed. We notice that the model systematically underestimates the data with low Δ_{mean} at any radius. This is a feature that was present also in the past literature works [Wojtak et al., 2011, Jimeno et al., 2014], and does not significantly affect the final $\hat{\Delta}_{mean}$ estimation.

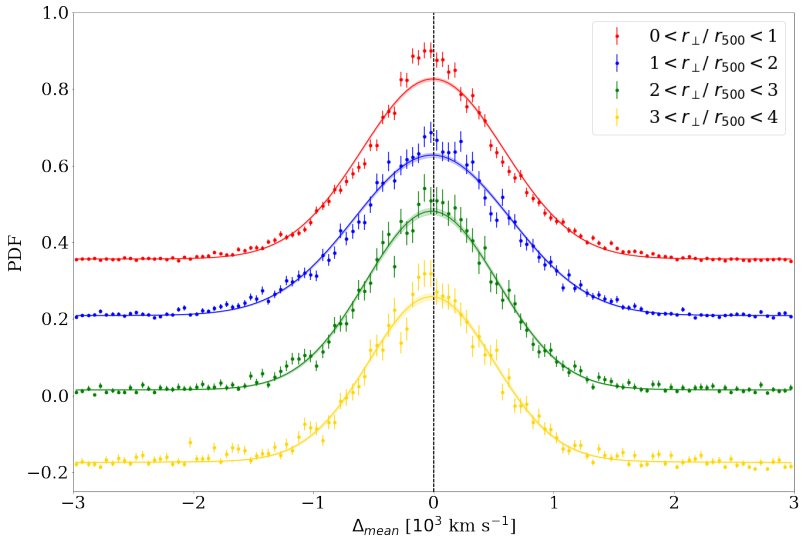

Figure 6.9: Velocity distributions of the WHL15 cluster member galaxies in the four bins of projected transverse distance, assuming the average positions of the BCG closest galaxies as the cluster center. These distributions are shifted vertically by an arbitrary amount (-0.2, 0, 0.2 and 0.35), for visual purposes. The colored points represent the data of the binned background-corrected phase-space diagram and the error bars represent the Poisson noise combined with the error of the background-correction method. The solid lines and the shaded colored areas show the best-fit models, and their errors, respectively.

As an example case, Fig.6.10 shows the corner plot of the MCMC parameter estimation for the velocity distribution, in this case in the bin $3 < r_{\perp}/r_{500} < 4$, assuming the average positions of the BCG closest galaxies as the cluster center. The corner plot shows that the parameter $\hat{\Delta}$ is independent of the other free parameters. We obtained similar results for all the distance bins analyzed.

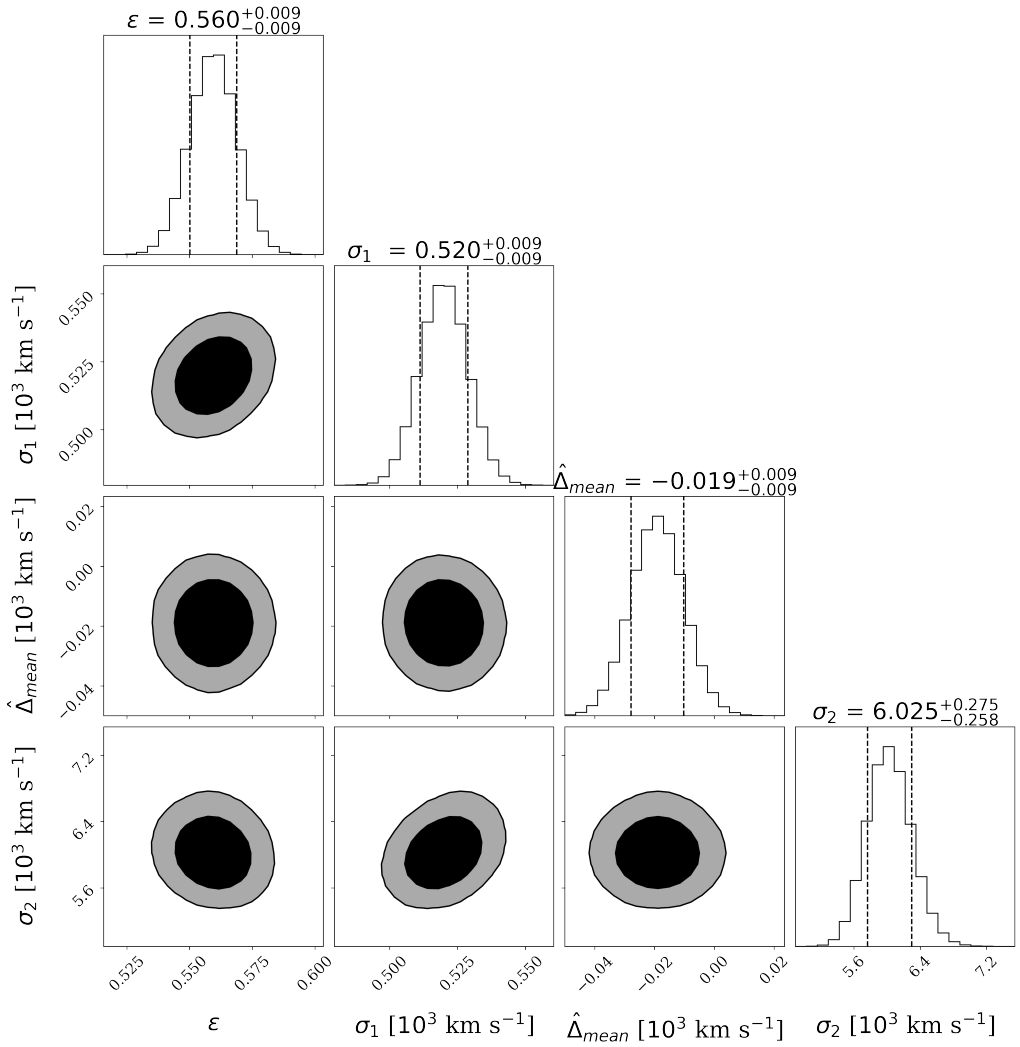

Figure 6.10: Corner plot showing the results of the MCMC parameter estimation for the velocity distribution of the WHL15 cluster member galaxies in the bin $3 < r_{\perp}/r_{500} < 4$, assuming the average positions of the BCG closest galaxies as the cluster center. The histograms on the diagonal show the marginalised posterior densities for each parameter (vertical dashed lines represent the 16_{th} and 84_{th} percentiles) and the best-fit parameters. The remaining plots show the 2D joint posterior densities of all parameter pairs, with the 68% and the 95% contours.

Figure 6.11 shows the comparison between the estimated $\hat{\Delta}$ within each bin and the GR, $f(R)$ and sDGP theoretical predictions, as a function of the cluster radius. The vertical error bars represent the range of $\hat{\Delta}_{mean}$ parameter containing 68% of the marginalized posterior probability. As it can be seen, we measure a significantly negative shift of the mean of the velocity distributions, as we expected from the theoretical analysis described in Chapter 4. As shown in Fig.6.11, our measurements are in agreement, within the errors, with the predictions of GR and sDGP, while in a marginal tension with $f(R)$ predictions, though the disagreement is not statistically significant. We measure also the integrated gravitational redshift signal up to four r_{500}, by considering all the cluster member galaxies in the background-corrected phase-space diagram shown in Fig.6.3. We get $\hat{\Delta}_{mean,int} = -11.4 \pm 3.3$ km s^{-1}, which is in agreement, within the errors, with the expected value of -10 km s^{-1} predicted in GR for clusters in the same range of masses as the WHL15 cluster member catalog.

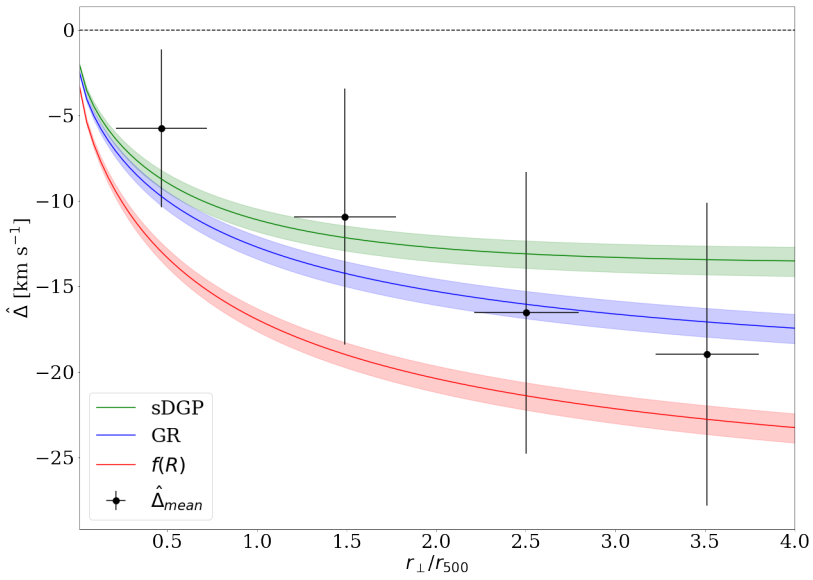

Figure 6.11: Comparison between the estimated $\hat{\Delta}_{mean}$ of the WHL15 cluster member galaxies within each bin of transverse distance and the theoretical predictions from GR (blue line), $f(R)$ (red line), sDGP (green line). The shaded colored areas show the model errors which are caused by the fitting uncertainties on the cluster mass distribution, the dispersion of the cluster redshifts and the dispersion of the concentration parameter values. The black points show the estimated $\hat{\Delta}_{mean}$. The vertical error bars represent the range of $\hat{\Delta}_{mean}$ parameter containing 68% of the marginalized posterior probability, while the horizontal error bars show the dispersion of the galaxy transverse distances in a given bin.

To impose new constraints on the gravity theory and to discriminate among the three different theories we analyzed, we proceed by fitting the measured $\hat{\Delta}_{mean}$, shown in Fig.6.11. We construct a model which takes into account the theoretical predictions of GR, $f(R)$ and sDGP. To do this, we modify the theoretical model given by Eq.(4.45), by changing the gravitational acceleration experienced by the photons inside the clusters. In practice, we multiply the gravitational constant G by a constant α (i.e. $G \rightarrow \alpha G$), which will be cosidered as the free parameter of the fit. By using this model we take into account not only the GR prediction, but also the modification of the gravitational force predicted by $f(R)$ and sDGP model. In fact, by construction α is equal to one in GR theory, while $\alpha = 1.33$ in the $f(R)$ theory and $\alpha \simeq 0.9$ in the sDGP model. We perform a MCMC analysis in order to fit the measured $\hat{\Delta}_{mean}$, using a Gaussian likelihood. It should be noted that this fitting procedure has never been implemented in past literature works.

Figure 6.12 shows the results of the MCMC analysis. We get $\alpha = 0.86 \pm 0.25$, with a reduced $\chi^2 = 0.23$. The value of the reduced χ^2 indicates a possible overestimation of the measurement errors. The best-fitting results confirm that our measurements are in agreement, within the error, with GR and sDGP predictions, while the $f(R)$ is marginally discarded at about 2σ. This is in slight disagreement with the past literature works of Wojtak et al. [2011] and Mpetha et al. [2021], whose results were consistent also with $f(R)$.

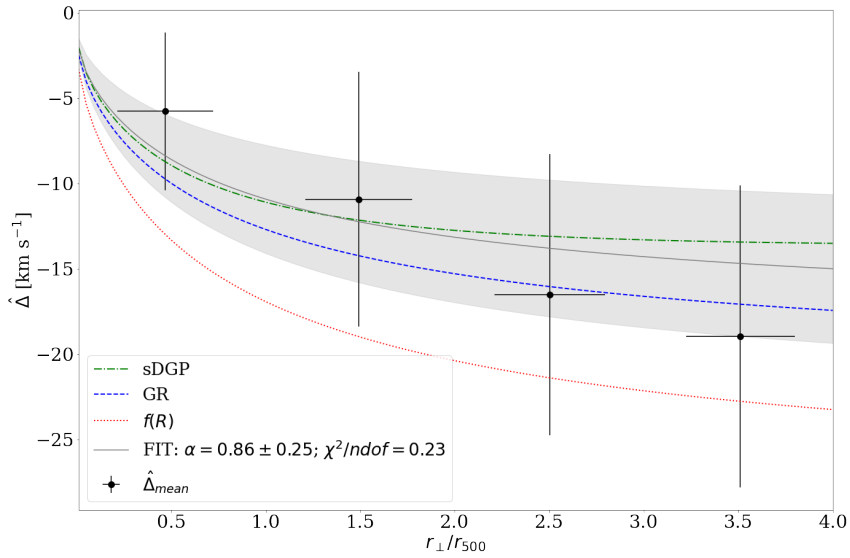

Figure 6.12: Best-fit model of $\hat{\Delta}(r_\perp/r_{500})$ from MCMC (grey solid line) for the WHL15 cluster member galaxies. The shaded grey area shows the 68% uncertainty on the posterior median. The theoretical predictions of GR (blue dashed line), $f(R)$ (red dotted line), sDGP (green dash-dotted line) are shown for comparison.

6.3.2 Gravitational Redshifts in DESI Cluster Catalog

In this Section we present the measurement results of the velocity distributions of the cluster member galaxies of the DESI cluster catalog.

Considering the background-corrected phase-space diagrams, shown in Fig.6.4, we perform again the procedure described in Sec.6.3.1, to recover the gravitational redshift measurements as a function of the cluster radius.

Figure 6.13 shows the velocity distributions in each bin of projected transverse distance and the associated best-fitting models. The reduced χ^2 is about 2 for all the best-fitting models we computed. As an example, Fig.6.14 shows the corner plot of the MCMC parameter estimation for the velocity distribution, in this case in the bin $2 < r_\perp/r_{500} < 3$. The descriptions of Fig.6.13 and Fig.6.14 are the same as Fig.6.9 and Fig.6.10, respectively.

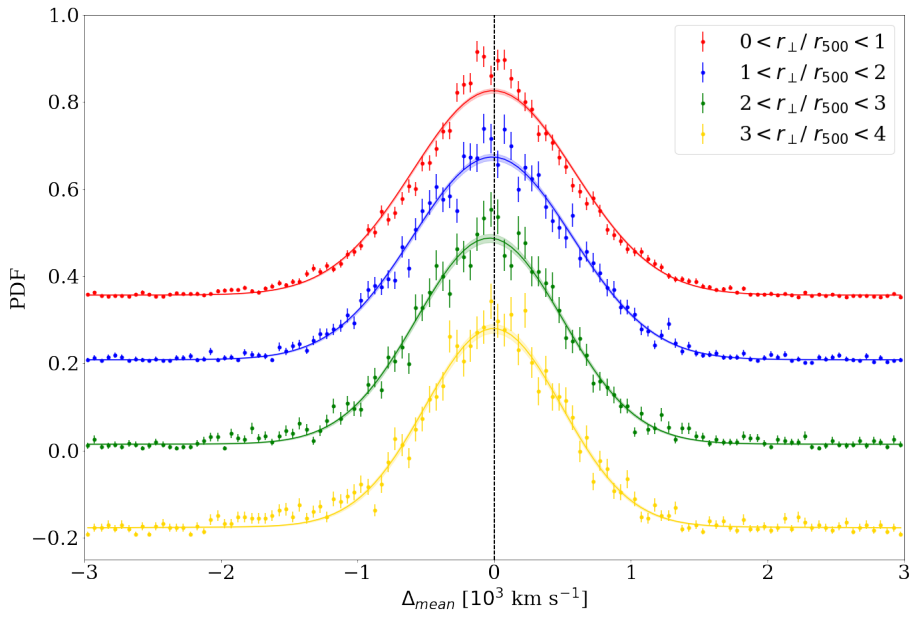

Figure 6.13: Velocity distributions of the DESI cluster member catalog in the four bins of projected transverse distances. The symbols are the same as in Fig.6.9.

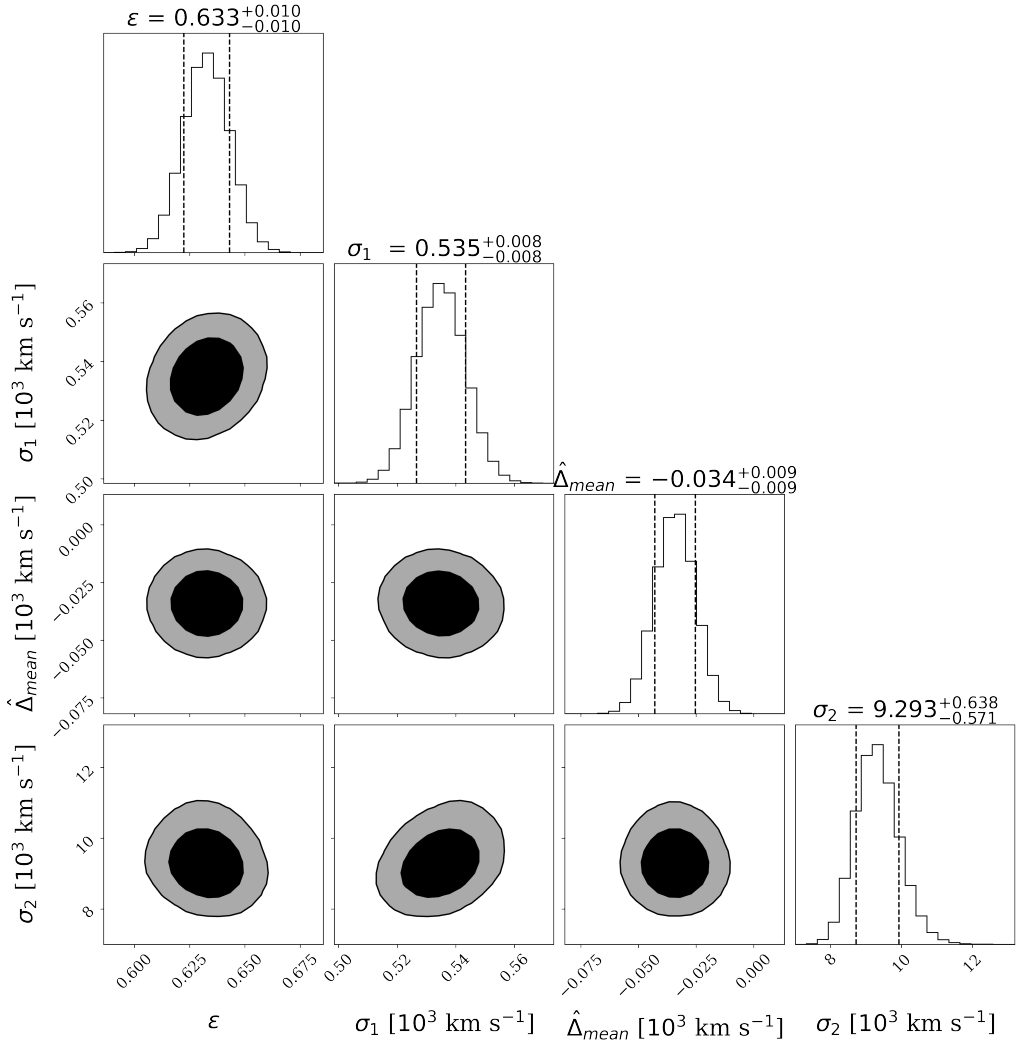

Figure 6.14: Corner plot showing the results of the MCMC parameter estimation for the velocity distribution in the bin $2 < r_\perp/r_{500} < 3$. The symbols are the same as in Fig.6.10.

Such as in Sec.6.3.1, we compare the estimated $\hat{\Delta}$ within each bin and the GR, $f(R)$ and sDGP theoretical predictions, the comparison is shown in Fig.6.15. In this case, the measurements are in agreement, within the errors, with the GR prediction for transverse distances less than $2r_{500} \simeq 1.3$ Mpc, while in the outermost bins the measured $\hat{\Delta}$ slightly depart from GR. We claim that this is probably caused by the effect of cluster false identifications, despite of the selections we made to mitigate this problem. Furthermore, when we constructed the DESI cluster member catalog, we mixed the spectroscopic data from the DESI cluster catalog and the SDSS galaxy survey. This fact can bias the final measurement due to the differences between the characteristics of the two surveys (e.g. difference in the spectroscopic

redshift template-fitting procedure), as claimed by Sadeh et al. [2015]. The effect of the mixed survey data is not well known and it was not taken into account in the theoretical model. Hence, going outside the cluster virialized region (i.e. $r_\perp \gtrsim 2$ Mpc), it is possible that this effect becomes more significant. Further investigations with numerical simulations are necessary in order to quantify the effect produced by mixed survey data.

In this case, the integrated gravitational redshift signal we get is $\hat{\Delta}_{mean,int} = -14.1 \pm 3.6$ km s^{-1}, which is in agreement, within the error, with the GR predictions for clusters in the same range of masses as the DESI cluster member catalog.

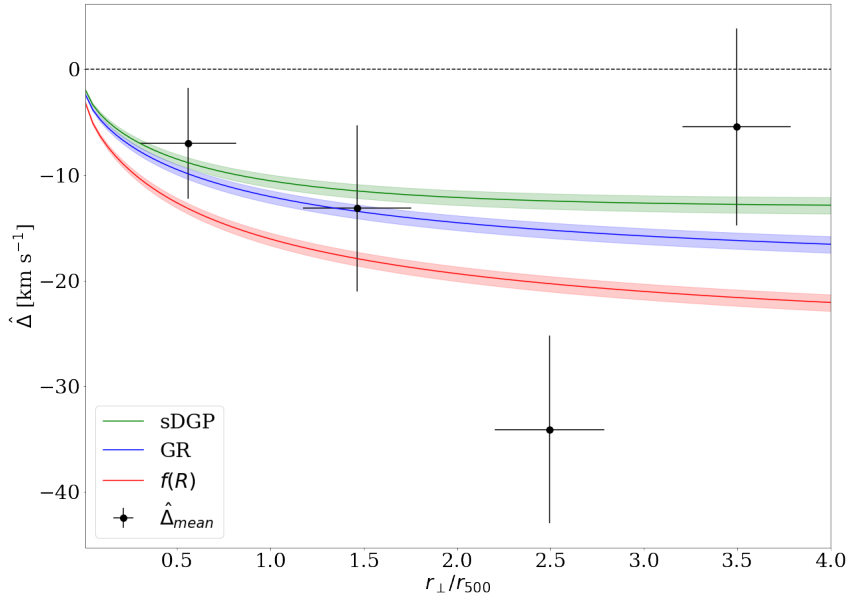

Figure 6.15: Comparison between the estimated $\hat{\Delta}_{mean}$ of the DESI cluster member catalog within each bin of projected transverse distance and the theoretical predictions from GR (blue line), $f(R)$ (red line), sDGP (green line). The symbols are the same as Fig.6.11.

We perform the MCMC analysis as described in Sec.6.3.1 for the DESI catalog; Fig.6.16 shows the results of this analysis. We get $\alpha = 1.04 \pm 0.28$, with a reduced $\chi^2 = 2.04$. The best-fit results are in agreement, within the error, with the three considered gravity theories. As explained previously, we do not know the effect caused by the mixed survey data, thus we perform again the MCMC analysis excluding the outermost bins. When we exclude the bin $3 < r_\perp/r_{500} < 4$, we get $\alpha = 1.27 \pm 0.32$, while, considering the transverse distances less than two r_{500} only, we get $\alpha = 0.83 \pm 0.38$. The three MCMC results are in agreement, within the error, between each other; thus the gravitational redshift measurement seems robust, despite

of the mixed survey effect. However, we are not able to discriminate among the three gravity theories, due to the measurement errors.

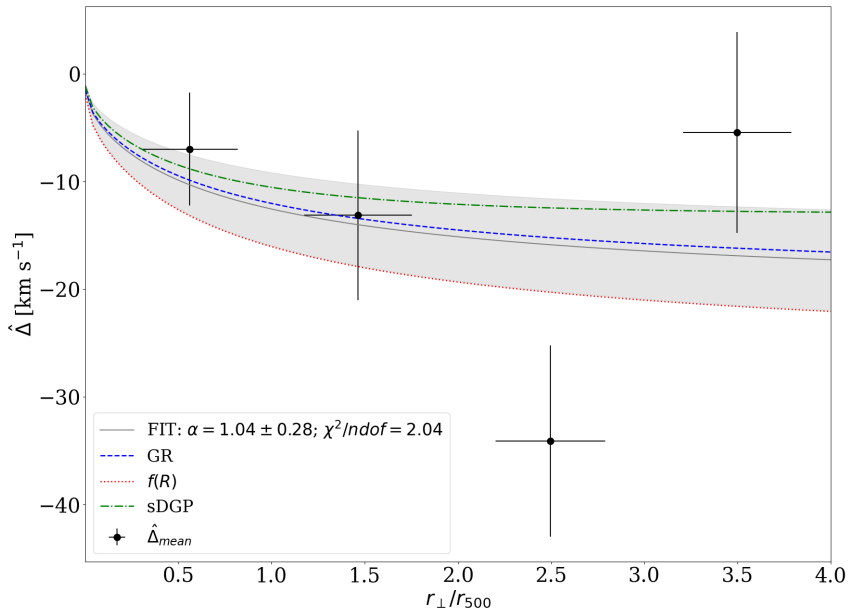

Figure 6.16: Best-fit model of $\hat{\Delta}(r_\perp/r_{500})$ from MCMC (grey solid line) for the DESI cluster member galaxies. The symbols are the same as in Fig.6.12.

Chapter 7

Conclusions and Future Perspectives

In this Thesis work we tested the Einstein theory of General Relativity by measuring the gravitational redshift effect in galaxy clusters, within the ΛCDM cosmological framework. To perform the gravitational redshift measurements, we created two new cluster member galaxies, as described in Chapter 5. In Appendix A, we described the investigations we conducted to study the impact on the final measurements of the selections we used to construct the cluster member catalogs, described in Sec.5.3. Following the method described in Kim and Croft [2004], we stacked the data of the cluster member galaxies in a single phase-space diagram and we corrected it for the background and foreground galaxy contaminations, as explained in Sec.6.1.1. We splitted the phase-space diagrams in four bins of transverse distances, recovering the galaxy velocity distributions within them. We implemented a MCMC analysis, described in Sec.6.1.2, to recover the shift of the mean of the velocity distributions, which is proportional to the gravitational redshift effect, as described in Chapter 4. We recovered an integrated gravitational redshift signal $\hat{\Delta}_{mean,int} = -11.4 \pm 3.3$ km s^{-1} for the WHL15 cluster catalog, and $\hat{\Delta}_{mean,int} = -14.1 \pm 3.6$ km s^{-1} for the DESI cluster catalog. These values are in agreement with the expected value of -10 km s^{-1}, predicted in GR for clusters in the same range of masses as the WHL15 and the DESI clusters.

We computed the theoretical gravitational redshift effect in three different gravity theories: GR, $f(R)$ and sDGP, described in Chapter 4. The gravitational redshift models are shown in Fig.6.7 as a function of the cluster radius and in Fig.6.8 as a function of the cluster mass. We compared our measurements with the predicted gravitational redshift effect as a function of the cluster radius. These comparison are shown in Fig.6.11 for the WHL15 cluster catalog, and Fig.6.15 for the DESI cluster catalog. We implemented a new statistical analysis in order to discriminate among the different gravity theories, as described in Sec.6.3.1. From this analysis we get: $\alpha = 0.86 \pm 0.25$ from the WHL15 catalog, and $\alpha = 1.04 \pm 0.28$ from the DESI catalog. The MCMC results in the two cluster member catalogs are in agreement, within the errors. Nevertheless, the estimated α value in the WHL15 cluster catalog is marginally inconsistent with the $f(R)$ theory, while that estimated in the DESI catalog is in agreement with the three analyzed gravity theories.

In this Thesis work, we demonstrated that the peculiar velocity distribution of the cluster member galaxies provides a powerful tool to directly investigate the gravitational potentials within galaxy clusters and to impose new constrains on the gravity theory on the largest scales of the Universe. Further investigations are necessary to corroborate the measurement method, by exploiting cosmological simulations, especially at high redshifts. Forecasting analyses are needed to compute the required number of clusters and associated member galaxies necessary to discriminate among different gravity theories with a high statistical significance (i.e. $\sim 5\sigma$ significance). Moreover, further investigations are necessary to improve the modelling for both galaxy velocity distributions and gravitational redshift theoretical predictions. The model improvements are necessary to take into account the BCG proper motions, and to relax the assumption of the cluster spherical symmetry and the NFW density profile. Furthermore, it is essential to investigate the effects caused by mixing the data from different spectroscopic surveys, in order to increase the available statistics by jointly combining data from different catalogs.

Appendix A

Testing the Systematic Uncertainties in the WHL15 and DESI Cluster Member Catalogs

In this Appendix we describe the tests we conduct to investigate the effects of the various selections on the cluster member galaxies, described in Sec.5.3, on the gravitational redshift measurements in the WHL15 and DESI cluster member catalogs. Moreover, we present the results we obtained when we assume the BCG as the cluster center, as done in the past literature works by Wojtak et al. [2011], Jimeno et al. [2014] and Sadeh et al. [2015].

A.1 Testing the Selections

When we searched for the WHL15 and DESI cluster member galaxies, we made a certain number of selections, as described in Sec.5.3. In this Section we discuss the impact of these choices on the gravitational redshift measurement.

A.1.1 Selection on the Number of the Cluster Member Galaxies

In the analysis presented in this Thesis, we decided to consider only the clusters which have at least 4 associated member galaxies. We do this following Wojtak et al. [2011] and Jimeno et al. [2014], who made a similar selection. This choice is useful to mitigate the problem of cluster false identification. We test this selection by measuring the gravitational redshift in the phase-space diagrams constructed by changing the minimum number of cluster associated member galaxies. We notice that if the minimum number increases above 6, the statistics becomes too low, and the measurement cannot be performed due to the too small number of clusters, and thus too high Poisson noise in the velocity distributions. On the other hand, if the minimum number of cluster member galaxies is less than 3, the cluster false identification significantly

affects the measurement causing a positive shift of the mean of the velocity distribution. On the other hand, in the range between 3 and 6, the selection does not significantly changes the final results, which are in agreement with those described in Sec.6.3.1 and in Sec.6.3.2 for the WHL15 and DESI cluster member catalogs, respectively.

A.1.2 Selection on the Average Galaxy Positions

A second choice we made in our analysis was to select only the cluster whose centers can be computed with at least 3 member galaxies. We made this choice to select only the cluster whose average redshifts have an error which is reduce by at least 50% with respect to the BCG spectroscopic redshift error. In fact, when we computed the velocity distributions, the center redshift error propagates to all the galaxy redshifts associated to that center. This is a major problem especially for the clusters with a large number of member galaxies. We made several tests by arbitrarily increasing the redshift error of the cluster center, up to 5×10^{-3}. We notice that, as the error increases, the velocity distributions have an increasing larger positive shift of the mean. Further analyses are necessary to investigate this effect. Moreover, we notice that if the number of member galaxies used to estimate the centers increases above 5, the statistics becomes too low, which does not allow us to obtain any measure. On the other hand, if this number is less than 3, the results are not statistically distinguishable from the ones obtained considering the BCG as the cluster center (these measurements are described in Sec.A.2). For clusters where the average center positions are computed with $3 - 5$ galaxies, the final results do not vary significantly from those described in Sec.6.3.1 and in Sec.6.3.2 for the WHL15 and DESI cluster member catalogs, respectively.

A.1.3 Redshift Selection

In our analysis, we selected only the clusters which have a redshift less than 0.5, in order to mitigate the problem of the cluster false identification and to have a not significant impact of the assumed cosmological model on the measurements. In order to test this selection, we measure the gravitational redshift changing the cluster redshift cut-off. When we consider the low-redshift cluster with $z < 0.2$, the lack of statistics prevent us to obtain any measurement. We also test the analysis up to $z = 0.6$. In this case the final measurements do not vary significantly from that described in Sec.6.3.1 and in Sec.6.3.2. Further studies are necessary to investigate the method at higher redshifts, by exploiting cosmological simulations, to quantify how gravitational redshift theoretical predictions are affected by the redshift dependence of cosmological parameters.

A.1.4 Mass Selection

A further selection we applied in our analysis was to consider only the clusters which have masses above 1.5×10^{14} $M_\odot$, in order to mitigate the problem of the cluster false identification, described in Sec.5.3. To investigate the impact of including also lower mass clusters, we measure also the gravitational redshift as a function of the cluster mass. We split the WHL15 cluster member catalog in four sub-catalogs in different cluster mass ranges, while the DESI cluster member catalog is divided in three sub-catalogs. We do not take into account clusters with masses lower than 3×10^{13} $M_\odot$, because for those the richness-mass relation is not calibrated, as described in Sec.5.1.1 and Sec.5.1.2 for the WHL15 and DESI cluster catalogs, respectively. For each sub-catalog we construct the background-corrected phase-space diagram and measure the integrated gravitational redshift signal up to $4\ r_{500}$.

Figure A.1 shows the comparison between the estimated $\hat{\Delta}$ within each sub-catalog and the theoretical predictions from GR, $f(R)$ and sDGP of the gravitational redshift as a function of the cluster mass for the WHL15 cluster member catalog, while Fig.A.2 shows the same for the DESI cluster member catalog. The figures show that the measurements at $M_{500} \gtrsim 2 \times 10^{14}$ $M_\odot$ for both the cluster member catalogs, are in agreement, within the errors, with the GR and sDGP theoretical predictions. Moreover, in this mass range the measured effect becomes more negative as the cluster mass increases, as expected. On the other hand, in the WHL15 clusters member catalog the $\hat{\Delta}_{mean}$ value for clusters with average mass of about 1.5×10^{14} $M_\odot$ is positive and it is not in agreement with any prediction, while the $\hat{\Delta}_{mean}$ measurement in lowest mass range is instead in agreement with the theoretical predictions from the three analyzed gravity theories. On the other hand, in the DESI cluster member catalog, considering clusters with an average mass of about 10^{14} $M_\odot$ we recover a positive value of $\hat{\Delta}_{mean}$, which is not in agreement with any model. These positive values of $\hat{\Delta}_{mean}$ in both the cluster member catalogs, are probably caused by the higher percentage of false identified clusters than in the high-mass sample.

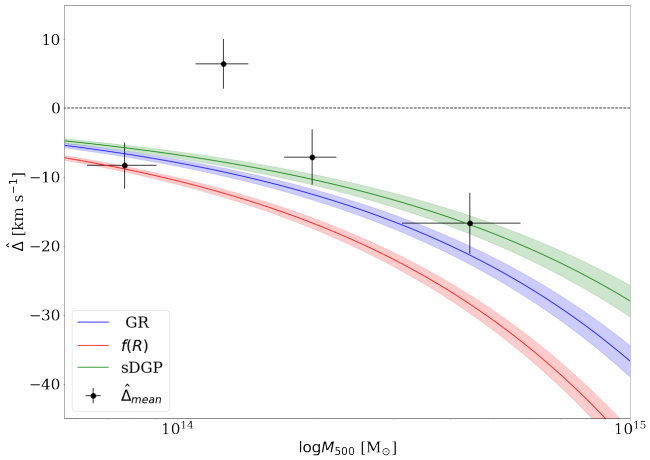

Figure A.1: Comparison between the estimated $\hat{\Delta}_{mean}$ of the WHL15 cluster member galaxies and the theoretical predictions from GR (blue line), $f(R)$ (red line), sDGP (green line). The shaded colored areas show the model errors, while the black points show the estimated $\hat{\Delta}_{mean}$. The vertical error bars represent the range of $\hat{\Delta}$ parameter containing 68% of the marginalized posterior probability, while the horizontal error bars show the dispersion of the cluster masses in a given bin.

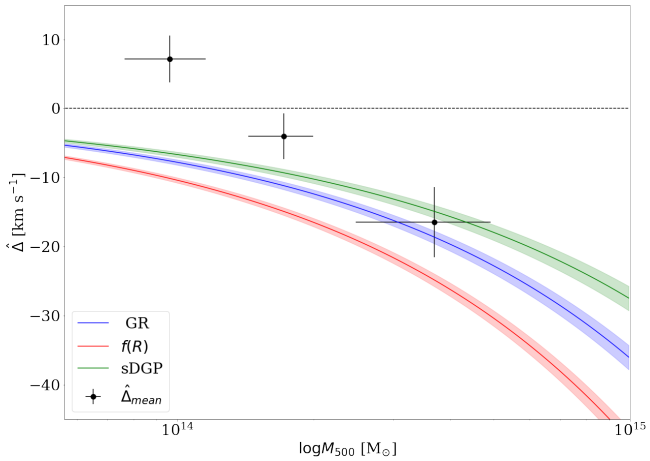

Figure A.2: Comparison between the estimated $\hat{\Delta}_{mean}$ of the DESI cluster member catalog and the theoretical predictions from GR (blue line), $f(R)$ (red line), sDGP (green line). The symbols are the same as in Fig.A.1.

To investigate the impact of the mass selection on the measurement, we stack all the clusters with mass above 3×10^{13} $M_{\odot}$ in a single background-corrected phase-space diagram and measure the gravitational redshift effect as a function of the cluster radius. We split the phase-space diagrams in four bins of width equal to r_{500}, as done in Sec.6.3.1 and in Sec.6.3.2 for the mass selected WHL15 and DESI cluster member catalogs, respectively. Figure A.3 shows the comparison between the estimated $\hat{\Delta}_{mean}$ within each bin and the theoretical predictions from GR, $f(R)$ and sDGP in the WHL15 catalog, while Fig.A.4 shows the same for the DESI cluster member catalog.

Figure A.3 shows that the measurements are slightly in disagreement with the theoretical predictions in all the four bins, differently from the mass-selected cluster member catalog consider in the analysis of this Thesis work (see Fig.6.11). Moreover, the measured $\hat{\Delta}$ is almost comparable with zero. Hence, the false identified low-mass clusters cause a positive shift of the mean of the velocity distribution.

Figure A.4 shows that the measurements are in agreement with the theoretical predictions only for transverse distances $1 < r_{\perp}/r_{500} < 3$. As we claimed previously, the low-mass clusters cause a positive shift of $\hat{\Delta}_{mean}$. Moreover, the departure from the theoretical models is caused by the effect of the mixed survey data, described in Sec.6.3.2.

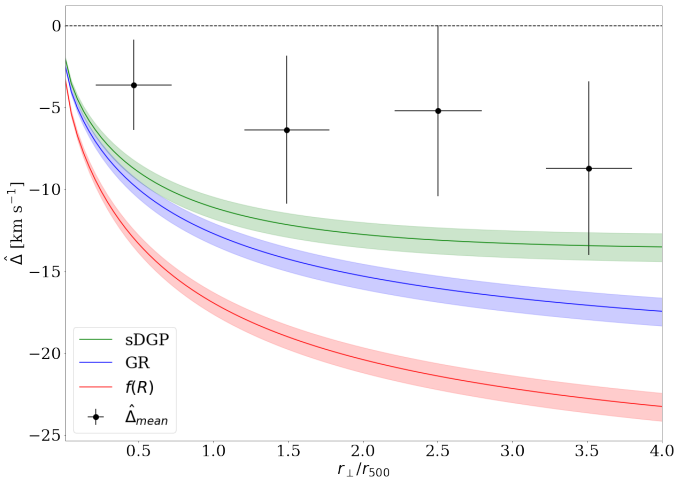

Figure A.3: Comparison between the estimated $\hat{\Delta}_{mean}$ of the WHL15 cluster member galaxies within each distance bin and the theoretical predictions from GR (blue line), $f(R)$ (red line), sDGP (green line). The symbols are the same as in Fig.A.1.

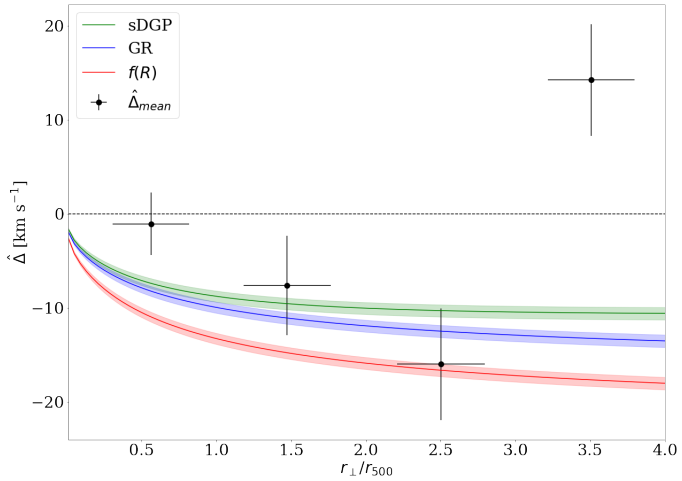

Figure A.4: Comparison between the estimated $\hat{\Delta}_{mean}$ of the DESI cluster member catalog within each distance bin and the theoretical predictions from GR (blue line), $f(R)$ (red line), sDGP (green line). The symbols are the same as in Fig.A.1.

We also fit the measured $\hat{\Delta}_{mean}$ by using the procedure described in Sec.6.3.1, to constrain the α parameter. Figure A.5 shows the result of the MCMC α estimation for the WHL15 clustercatalog, while Fig.A.6 shows the same for the DESI cluster catalog.

For the WHL15 cluster catalog, we recover a value of α equal to 0.51 ± 0.19 with a reduced χ^2 of 0.07. This value is marginally in disagreement with the estimation obtained for the mass selected WHL15 cluster member catalog, shown in Fig.6.12. On the other hand, for the DESI cluster member catalog, we recover a value of α equal to $0.26^{+0.19}_{-0.16}$ with a reduced χ^2 of 4.78. Such as the WHL15 case, the estimated α is in disagreement with the estimation obtained for the mass selected DESI cluster member catalog, shown in Fig.6.16. Moreover, the error on the α parameter is asymmetric because we impose as a prior that α has to be greater than zero (if $\alpha = 0$ we do not have a gravitational force, and if $\alpha < 0$ we have an anti-gravity force).

Further investigations are necessary to better understand these effects by exploiting cosmological simulations.

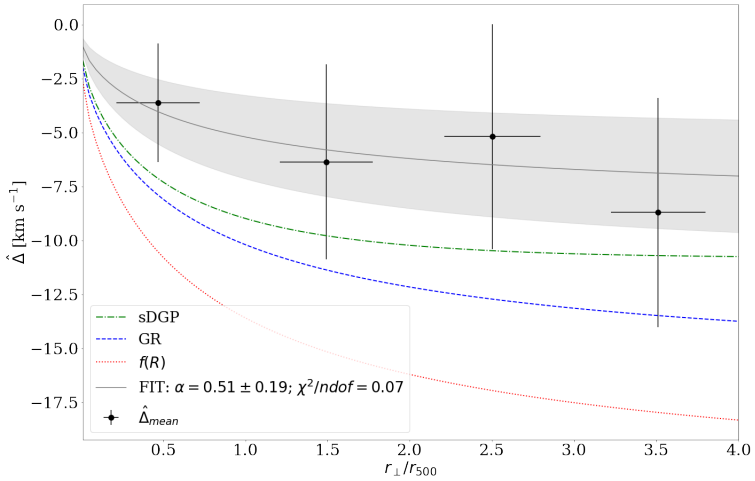

Figure A.5: Best-fit model of $\hat{\Delta}(r_\perp/r_{500})$ from MCMC (grey solid line) for the WHL15 cluster catalog. The shaded grey area shows the 68% uncertainty on the posterior median. The theoretical predictions of GR (blue dashed line), $f(R)$ (red dotted line), sDGP (green dash-dotted line) are shown for comparison.

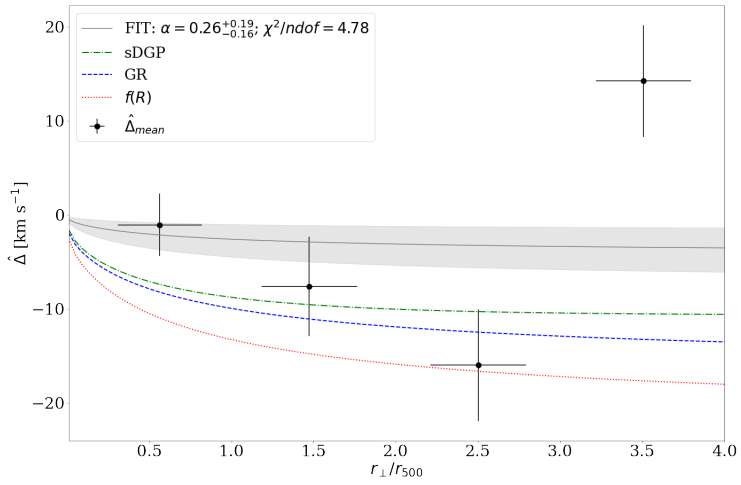

Figure A.6: Best-fit model of $\hat{\Delta}(r_\perp/r_{500})$ from MCMC (grey solid line) for the DESI cluster catalog. The symbols are the same as in Fig.A.5.

A.2 Assuming the BCG as the Cluster Center

To investigate if the average galaxy positions provide a better approximation of the center of the cluster potential wells than the BCG positions, we repeat the analysis by assuming the BCG as the cluster center, as done in past literature works. We construct the cluster member catalogs by using the same selection criteria described in Sec.5.3. When we estimate the cluster center from the BCG, all the cluster member galaxies are selected all over again. The new set of member galaxies in the outer cluster region is different in this case, since galaxies near the edges of our selection can be either included or excluded, depending on the center choice, according to the selection criteria described in Sec.5.3.

We obtain a cluster member catalog with $3,020$ clusters and $46,819$ cluster member galaxies for the WHL15 clusters, while for the DESI clusters we obtain a cluster member catalog with $2,041$ clusters and $39,509$ cluster member galaxies.

We construct the background-corrected phase-space diagrams as described in Sec.6.1.1, in order to compare the results with those described in Sec.6.3.1 and in Sec.6.3.2. Then, we fit the galaxy velocity distributions, Δ_{BCG}, to retrieve the gravitational redshift signal as a function of the cluster radius. Figure A.7 shows the comparison between the estimated $\hat{\Delta}_{BCG}$ of the WHL15 cluster member galaxies within each distance bin and the theoretical predictions from GR, $f(R)$, sDGP, while Fig.A.8 shows the same for the DESI cluster member catalog.

Figure A.7 shows that the measurements in the outermost bins are in agreement with the theoretical models, while those in the inner bins are not and present a positive value of the mean of the galaxy velocity distribution. This problem in the inner bins is mainly caused by two effects. Firstly, the effect of the BCG peculiar velocities, which is similar to the TD effect, but less intense, causes a positive shift of $\hat{\Delta}$, as demonstrated by Kaiser [2013]. This effect was not included in the theoretical model, described in Chapter 4, because it is expected to be a second-order effect. Moreover, we do not have any information about the BCG peculiar velocities. Further investigations are necessary to understand the real impact of the BCG peculiar motions. Secondly, there is the possibility of the BCG misidentification, due to the surface brightness modulation effect. In the case the real BCG is not identified, due to velocity effects, so we may erroneously consider as the center a galaxy which in reality is an hot-population object, and which may not lie near the center of the cluster gravitational potential well. Thus, the BCG false identification might cause a positive shift of the mean of the velocity distribution.

Figure A.8 shows that the measurement in the innermost bin is in agreement with the theoretical models, while those in the central and outermost bins are not, differently from the measured $\hat{\Delta}_{BCG}$ in the WHL15 catalog, shown in Fig.A.7. The measurement in the outermost bin present a large negative value of $\hat{\Delta}_{BCG}$, which is in agreement, within the error, with the $f(R)$ model. We claim that the measurements, shown in Fig.A.8, are not mainly affected by the BCG peculiar motions, described previously, which principally affect the innermost bins. In fact, the DESI cluster member catalog is mainly contaminated by the unknown effect of mixing the cluster data from the DESI survey and the galaxy spectroscopic data form the SDSS. Further investigations are needed to better understand the impact of this effect.

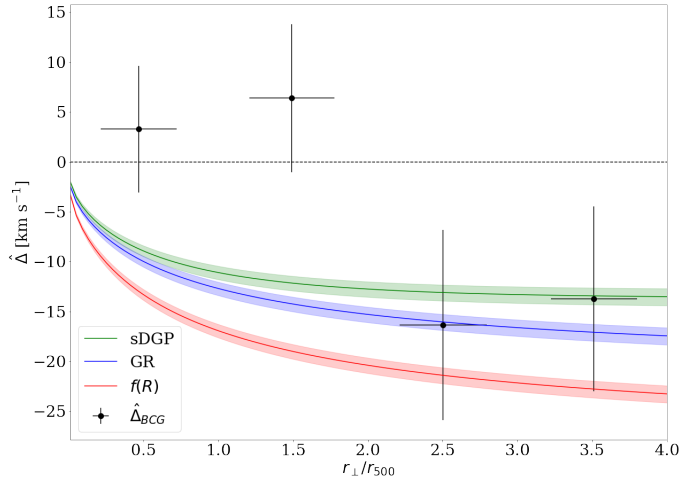

Figure A.7: Comparison between the estimated $\hat{\Delta}_{BCG}$ of the WHL15 cluster member galaxies within each distance bin and the theoretical predictions from GR (blue line), $f(R)$ (red line), sDGP (green line). The symbols are the same as in Fig.A.1.

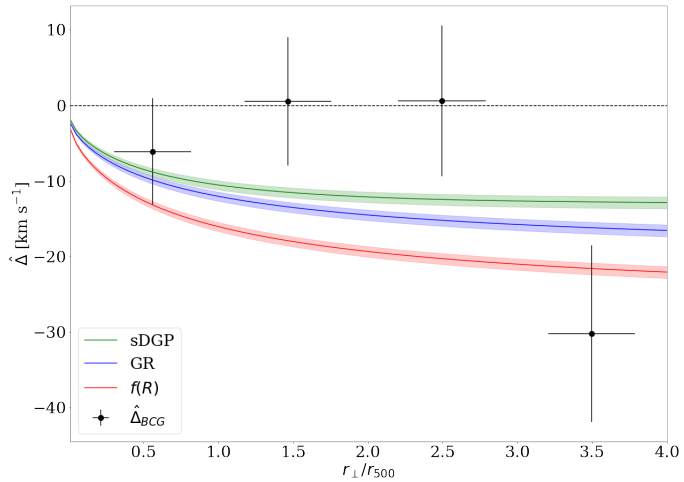

Figure A.8: Comparison between the estimated $\hat{\Delta}_{BCG}$ of the DESI cluster member galaxies within each distance bin and the theoretical predictions from GR (blue line), $f(R)$ (red line), sDGP (green line). The symbols are the same as in Fig.A.1.

We estimate the parameter α by fitting the measured $\hat{\Delta}_{BCG}$, shown in Fig.A.7 and Fig.A.8. We use the same fitting procedure described in Sec.6.3.1. Figures A.9 and A.10 show the computed best-fit models for the WHL15 and DESI cluster member catalogs, respectively.

For the WHL15 cluster member catalog, we get $\alpha = 0.32^{+0.25}_{-0.20}$ with a reduced χ^2 equal to 1.78. In this case, the best-fit model is marginally inconsistent with any gravity theory we analyzed and it is almost comparable with zero. On the other hand, for the DESI cluster member catalog, we obtain $\alpha = 0.55^{+0.32}_{-0.29}$ with a reduced χ^2 equal to 1.67. In this case, the best-fit model is almost in agreement with the sDGP model. For both the cluster member catalogs, the error on the α parameter is asymmetric, due to the prior we impose in the MCMC analysis, as described in Sec.A.1.4

Hence, we tend to conclude that we do not have a reliable α estimation due to the BCG misidentification and peculiar velocities, which are not taken into account in the model. Further investigations are necessary to improve the modeling when we assume the BCG as the cluster center.

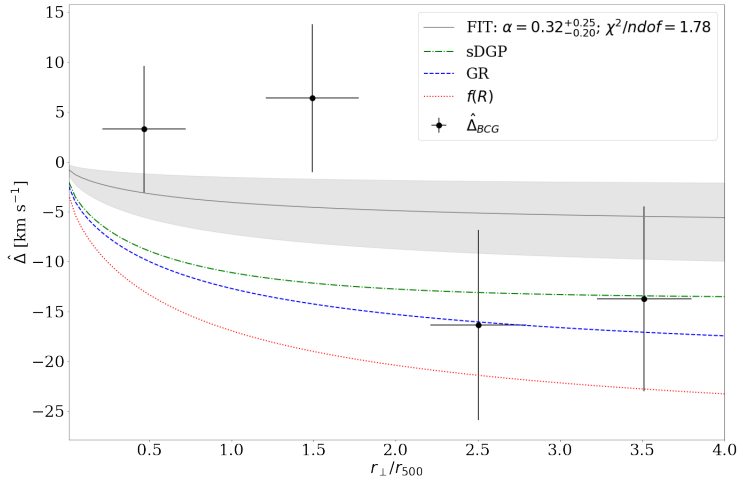

Figure A.9: Best fit model of $\hat{\Delta}(r_\perp/r_{500})$ from MCMC (grey solid line) for the WHL15 cluster member galaxies, which are identified assuming the BCG as the cluster center. The symbols are the same as in Fig.A.5.

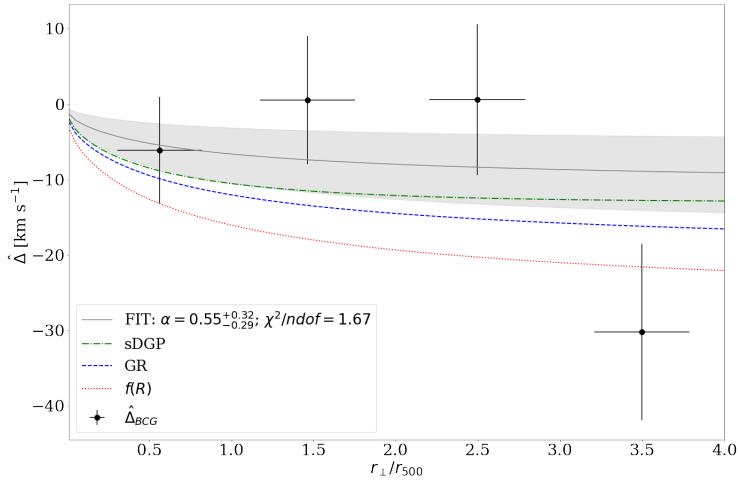

Figure A.10: Best fit model of $\hat{\Delta}(r_\perp/r_{500})$ from MCMC (grey solid line) for the DESI cluster member galaxies, which are identified assuming the BCG as the cluster center. The symbols are the same as in Fig.A.5.

Bibliography

K. N. Abazajian, J. K. Adelman-McCarthy, M. A. Agüeros, S. S. Allam, C. A. Prieto, D. An, K. S. J. Anderson, S. F. Anderson, J. Annis, N. A. Bahcall, and et al. The seventh data release of the sloan digital sky survey. *The Astrophysical Journal Supplement Series*, 182 (2):543–558, 2009.

N. Aghanim et al. Planck 2018 Results, Paper I-X. *Astronomy and Astrophysics*, 641:A6, 2020.

R. Ahumada et al. The 16th Data Release of the Sloan Digital Sky Surveys: First Release from the APOGEE-2 Southern Survey and Full Release of EBOSS Spectra. *The Astrophysical Journal Supplement Series*, 249(1), 2020.

I. K. Baldry. Reinventing the slide rule for redshifts: the case for logarithmic wavelength shift. 2018.

J. D. Bekenstein. Relativistic gravitation theory for the modified newtonian dynamics paradigm. *Phys. Rev. D*, 70:083509, 2004.

F. Bellagamba et al. Amico: optimized detection of galaxy clusters in photometric surveys. *Monthly Notices of the Royal Astronomical Society*, 473(4):5221–5236, 2017.

J. Binney et al. Galactic Dynamics. 1987.

Y.-C. Cai et al. Gravitational redshift and asymmetric redshift-space distortions for stacked clusters. *Monthly Notices of the Royal Astronomical Society*, 468(2):1981–1993, 2017.

A. Cappi. Gravitational redshift in galaxy clusters . *Astronomy and Astrophysics*, 301:6–10, 1995.

J. Casado. Steady flow cosmological model. *Astrophysics and Space Science*, 344:513–520, 2013.

A. Cavaliere and R. Fusco-Fermiano. X-rays from hot plasma in clusters of galaxies. *Astronomy and Astrophysics*, 49(1):137–144, 1976.

N. Clerc, C. C. Kirkpatrick, A. Finoguenov, R. Capasso, J. Comparat, S. Damsted, K. Furnell, A. E. Kukkola, J. Ider Chitham, A. Merloni, M. Salvato, A. Gueguen, T. Dwelly, C. Collins, A. Saro, G. Erfanianfar, D. P. Schneider, J. Brownstein, G. A. Mamon, N. Padilla, E. Jullo, and D. Bizyaev. SPIDERS: overview of the X-ray galaxy cluster follow-up and the final spectroscopic data release. *Monthly Notices of the Royal Astronomical Society*, 497(3): 3976–3992, 2020.

P. Coles and F. Lucchin. Cosmology: the origin and evolution of cosmic structure. 2008.

R. A. C. Croft. Gravitational redshifts from large-scale structure. *Monthly Notices of the Royal Astronomical Society*, 434(4):3008–3017, 08 2013.

W. Cui, C. Power, V. Biffi, S. Borgani, G. Murante, D. Fabjan, A. Knebe, G. F. Lewis, and G. B. Poole. How does our choice of observable influence our estimation of the centre of a galaxy cluster? Insights from cosmological simulations. *Monthly Notices of the Royal Astronomical Society*, 456(3):2566–2575, 2015.

K. Dawson et al. The baryon oscillation spectroscopic survey of sdss-iii. *The Astronomical Journal*, 145(1):10, Dec 2012.

K. Dawson et al. THE SDSS-IV EXTENDED BARYON OSCILLATION SPECTROSCOPIC SURVEY: OVERVIEW AND EARLY DATA. *The Astronomical Journal*, 151(2):44, 2016.

A. De Felice and S. Tsujikawa. f(r) theories. *Living Reviews in Relativity*, 13(1), 2010.

C. Deffayet. Cosmology on a brane in minkowski bulk. *Physics Letters B*, 502(1):199–208, 2001.

E. Di Valentino et al. In the realm of the hubble tension—a review of solutions. *Classical and Quantum Gravity*, 38(15), 2021.

A. Duffy et al. Dark matter halo concentrations in the Wilkinson Microwave Anisotropy Probe year 5 cosmology. *Monthly Notices of the Royal Astronomical Society:Letters*, 390:L64–L68, 2008.

G. Dvali, G. Gabadadze, and M. Porrati. 4d gravity on a brane in 5d minkowski space. *Physics Letters B*, 485(1):208–214, 2000.

A. Einstein. Zur allgemeinen relativitätstheorie. *Sitzungsberichte*, pages 778–801, 1915.

Eisenstein. Spectroscopic target selection for the sloan digital sky survey: The luminous red galaxy sample. *The Astronomical Journal*, 122(5):2267–2280, 2001.

J. Erler et al. Planck's view on the spectrum of the Sunyaev-Zeldovich effect. *Monthly Notices of the Royal Astronomical Society*, 476:3008–3017, 2018.

A. Fabian. Cooling flows in clusters of galaxies. *Annual Review of Astronomy and Astrophysics*, 32:277–318, 1994.

W. Fang, S. Wang, W. Hu, Z. Haiman, L. Hui, and M. May. Challenges to the dgp model from horizon-scale growth and geometry. *Phys. Rev. D*, 78:103509, 2008.

A. Friedmann. Über die krümmung des raumes. *Zeitschrift für Physik*, pages 377–386, 1922.

B. Fuchs. The amount of dark matter in spiral galaxies. *Astro- and Particle Physics*, page 25, 2001.

J. Gao, H. Zou, X. Zhou, and X. Kong. A catalog of galaxy clusters identified from SCUSS, SDSS, and UNWISE. *Publications of the Astronomical Society of the Pacific*, 132(1008): 024101, 2020.

S. Godini et al. Scaling Relations for Galaxy Clusters: Properties and Evolution . *Space Science Reviews*, 177:247–282, 2013.

L. Granda. Unified inflation and late-time accelerated expansion with exponential and r2 corrections in modified gravity. *Symmetry*, 12:794, 2020.

S. M. Hansen, E. S. Sheldon, R. H. Wechsler, and B. P. Koester. THE GALAXY CONTENT OF SDSS CLUSTERS AND GROUPS. *The Astrophysical Journal*, 699(2):1333–1353, jun 2009.

J. Hao et al. A GMBCG Galaxy Cluster Catalog of 55,424 Rich Clusters from SDSS DR7 . *The Astrophysical Journal Supplement Series*, 191(2):254–274, 2010.

J. H. Jeans. The Stability of a Spherical Nebula. *Philosophical Transactions of the Royal Society of London Series A*, 199:1–53, 1902.

P. Jimeno et al. Comparing gravitational redshifts of SDSS galaxy clusters with the magnification redshift enhancement of background BOSS galaxies. *Monthly Notices of the Royal Astronomical Society*, 10 2014.

A. Joyce et al. Dark energy versus modified gravity. *Annual Review of Nuclear and Particle Science*, 66(1):95–122, 2016.

N. Kaiser. Measuring gravitational redshifts in galaxy clusters. *Monthly Notices of the Royal Astronomical Society*, 435(2):1278–1286, 08 2013.

J. Khoury and A. Weltman. Chameleon cosmology. *Phys. Rev. D*, 69:044026, 2004.

Y.-R. Kim and R. A. C. Croft. Gravitational redshift in simulated galaxy clusters . *The Astrophysical Journal*, 607, 2004.

A. V. Kravtsov et al. Formation of galaxy clusters. *Annual Review of Astronomy and Astrophysics*, 50(1):353–409, 2012.

G. Lesci et al. Amico galaxy clusters in kids-dr3: cosmological constraints from counts and stacked weak-lensing. 2020.

R. Li et al. Constraints on the identity of the dark matter from strong gravitational lenses. *Monthly Notices of the Royal Astronomical Society*, 460(1):363–372, 2016.

A. Loeb. 2006. URL https://ned.ipac.caltech.edu/level5/Sept06/Loeb/Loeb4.html.

F. Marulli et al. Cosmology with clustering anisotropies: disentangling dynamic and geometric distortions in galaxy redshift surveys. *Monthly Notices of the Royal Astronomical Society*, 426(3):2566–2580, 2012.

F. Marulli et al. CosmoBolognaLib: C++libraries for cosmological calculations. *Astrophysics Source Code Library*, 2016.

F. Marulli et al. Redshift-space distortions of galaxies, clusters, and agn. *Astronomy and Astrophysics*, 599:A106, 2017.

F. Marulli et al. The xxl survey. *Astronomy and Astrophysics*, 620:A1, 2018.

F. Marulli et al. C^3 Cluster Clustering Cosmology I. New Constraints on the Cosmic Growth Rate at $z \sim 0.3$ from Redshift-space Clustering Anisotropies. *the Astrophysical Journal*, 920(1), 2021.

P. Meszaros. The behaviour of point masses in an expanding cosmological substratum. *Astronomy and Astrophysics*, 37(2):225–228, 1974.

A. D. Montero-Dorta and F. Prada. The SDSS DR6 luminosity functions of galaxies. *Monthly Notices of the Royal Astronomical Society*, 399(3):1106–1118, Nov. 2009.

L. Moscardini and K. Dolag. Cosmology with numerical simulations. In *Dark Matter and Dark Energy*, pages 217–237. Springer, 2011.

C. T. Mpetha et al. Gravitational redshifting of galaxies in the spiders cluster catalogue. *Monthly Notices of the Royal Astronomical Society*, 503(1):669–678, 2021. ISSN 1365-2966.

S. Nadathur, S. Hotchkiss, and R. Crittenden. Tracing the gravitational potential using cosmic voids. *Monthly Notices of the Royal Astronomical Society*, 467(4):4067–4079, 2017.

J. F. Navarro, C. S. Frenk, and S. D. M. White. Simulations of X-ray clusters. *Monthly Notices of the Royal Astronomical Society*, 275(3):720–740, 08 1995.

A. Nicolis and R. Rattazzi. Classical and quantum consistency of the DGP model. *Journal of High Energy Physics*, 2004(06):059–059, 2004.

J. R. Peterson et al. X-ray imaging-spectroscopy of abell 1835. *Astronomy and Astrophysics*, 365(1):L104–L109, 2001.

W. H. Press and P. Schechter. Formation of Galaxies and Clusters of Galaxies by Self-Similar Gravitational Condensation. *Astrophysical Journal*, 187:425–438, 1974.

A. Riess et al. Large magellanic cloud cepheid standards provide a 1% foundation for the determination of the hubble constant and stronger evidence for physics beyond ΛCDM. 876 (1):85, 2019.

A. G. Riess et al. Observational evidence from supernovae for an accelerating universe and a cosmological constant. *The Astronomical Journal*, 116(3):1009–1038, 1998.

E. Rykoff et al. redMaPPer. I. Algorithm and SDSS DR8 Catalog . *The Astrophysical Journal*, 785:104, 2014.

I. Sadeh, L. L. Feng, and O. Lahav. Gravitational redshift of galaxies in clusters from the sloan digital sky survey and the baryon oscillation spectroscopic survey. *Physical Review Letters*, 114(7), 2015.

L. Salvati et al. Constraints from thermal sunyaev-zel'dovich cluster counts and power spectrum combined with cmb. *Astronomy and Astrophysics*, 614:A13, 2018.

F. Schmidt. Dynamical masses in modified gravity. *Phys. Rev. D*, 81:103002, 2010.

T. P. Sotiriou and V. Faraoni. $f(r)$ theories of gravity. *Rev. Mod. Phys.*, 82:451–497, 2010.

A. Starobinsky. A new type of isotropic cosmological models without singularity. *Physics Letters B*, 91(1):99–102, 1980.

M. Strauss et al. Spectroscopic target selection in the sloan digital sky survey: The main galaxy sample. *The Astronomical Journal*, 124(3):1810–1824, 2002.

R. Sunyaev and Y. B. Zel'dovich. The Observations of Relic Radiation as a Test of the Nature of X-Ray Radiation from the Clusters of Galaxies. *Comments on Astrophysics and Space Physics*, 4:173, 1972.

J. C. Vernaleo and C. S. Reynolds. Agn feedback and cooling flows: Problems with simple hydrodynamic models. *The Astrophysical Journal*, 645(1):83–94, jul 2006.

A. Veropalumbo et al. An improved measurement of baryon acoustic oscillations from the correlation function of galaxy clusters at z $\sim$ 0.3. *Monthly Notices of the Royal Astronomical Society*, 442(4):3275–3283, 2014.

A. Veropalumbo et al. Measuring the distance–redshift relation with the baryon acoustic oscillations of galaxy clusters. *Monthly Notices of the Royal Astronomical Society*, 458(2): 1909–1920, 2016.

Z. Wen et al. A CATALOG OF 132,684 CLUSTERS OF GALAXIES IDENTIFIED FROM SLOAN DIGITAL SKY SURVEY III. *The Astrophysical Journal Supplement Series*, 199 (2):34, 2012.

Z. Wen et al. Calibration of the optical mass proxy for clusters of galaxies and an update of the WHL12 cluster catalog. *The Astrophysical Journal*, 807:178, 2015.

R. Wojtak, E. Łokas, G. A. Mamon, S. Gottlöber, F. Prada, and M. Moles. Interloper treatment in dynamical modelling of galaxy clusters. *Astronomy & Astrophysics*, 466(2):437–449, 2007.

R. Wojtak et al. Gravitational redshift of galaxies in clusters as predicted by general relativity. *Nature*, 477:567–569, 2011.

J. K. Yadav, J. S. Bagla, and N. Khandai. Fractal dimension as a measure of the scale of homogeneity. *Monthly Notices of the Royal Astronomical Society*, 2010.

D. York et al. The sloan digital sky survey: Technical summary. *The Astronomical Journal*, 120(3):1579–1587, 2000.

Zhao. Testing gravity theories via transverse doppler and gravitational redshifts in galaxy clusters. *Phys. Rev. D*, 88, 2013.

I. Zhuravleva et al. Turbulent heating in galaxy clusters brightest in x-rays. *Nature*, 515(7525): 85–87, 2014.

H. Zou, J. Gao, X. Zhou, and X. Kong. Photometric redshifts and stellar masses for galaxies from the DESI legacy imaging surveys. *The Astrophysical Journal Supplement Series*, 242 (1):8, 2019.

H. Zou, J. Gao, X. Xu, X. Zhou, J. Ma, Z. Zhou, T. Zhang, J. Nie, J. Wang, and S. Xue. Galaxy clusters from the desi legacy imaging surveys. i. cluster detection. *The Astrophysical Journal Supplement Series*, 253(2):56, 2021.

F. Zwicky. Die Rotverschiebung von extragalaktischen Nebeln. *Helvetica Physica Acta*, 6: 110–127, 1933.

E. L. Łokas and G. A. Mamon. Properties of spherical galaxies and clusters with an NFW density profile. *Monthly Notices of the Royal Astronomical Society*, 321(1):155–166, 02 2001.